

AD 706138

# COLUMBIA UNIVERSITY

IN THE CITY OF NEW YORK

## ELECTRONICS RESEARCH LABORATORIES

632 WEST 125th STREET

NEW YORK, NEW YORK 10027

DIAGNOSTIC STUDY OF THE FLUID TRANSPERSION ARC

FINAL REPORT F-1/312

AFOSR 70-0195TR

APRIL 1, 1964 TO MARCH 31, 1969

By

C. SHEER, S. KORMAN, C.G. STOJANOFF AND P.S. TSCHANG

Prepared for

MECHANICS DIVISION  
AIR FORCE OFFICE OF SCIENTIFIC RESEARCH  
1400 WILSON BOULEVARD  
ARLINGTON, VA., 22209

CONTRACT AF 49(638)-1395  
PROJECT TASK 9782-02



## FOREWORD

This final report was prepared by staff members of the Plasma Engineering Laboratory of the Electronics Research Laboratories, Columbia University, New York, N. Y., under Contract AF 49(638)-1395, for the Mechanics Division, Air Force Office of Scientific Research, Office of Aerospace Research, USAF. The work was performed under Project Task 9783-02 under the technical cognizance of Mr. Paul A. Thurston SREM, of the Mechanics Division, AFOSR.

That portion of the work done under this contract dealing with the development of a radiation source for solar simulation was jointly supported by the Office of Advanced Research and Technology, National Aeronautics and Space Administration, under the cognizance of Mr. Conrad Mook.

Acknowledgements are made to Mr. William Henriksen for his invaluable mechanical designs and to Messrs. Vito Fiore, Mark Gelband and Nestor Santiago for their assistance in carrying out the experiments. The authors are also grateful for the cooperation and assistance of the technical staff of the Electronics Research Laboratories, under the direction of Professor L. H. O'Neill.

### ABSTRACT

This report covers the investigation of the fluid transpiration arc in combination with the fluid convection cathode. Various arc configurations and operating techniques are described. Preliminary theoretical treatments of the interaction phenomena due to gas injection through a porous anode and through a tightly shrouded cathode nozzle with the arc discharge are carried out. Good agreement has been shown in some respects although several anomalies have been found attributed to deficiencies in the modelling. Several diagnostic techniques were developed during this investigation featuring transient plasma probes. These include a Hall magnetic probe, a thermocouple probe, a fiber optics probe and a Pitot tube probe. The cause of arc ignition damage to electrodes was investigated and corrected. The radiation characteristics of a combination arc source featuring a collinear geometry for the fluid transpiration anode and fluid convection cathode, were also investigated. Improved performance in conversion efficiency and luminous efficacy was demonstrated along with a favorable brightness profile.

AUTHORIZATION

The work described in this report was performed at the Electronics Research Laboratories of the School of Engineering and Applied Science of Columbia University. The report was prepared by C. Sheer, S. Korman, C. G. Stojanoff and P. S. Tschang.

This project was sponsored by the Mechanics Division, Office of Aerospace Research, U. S. Office of Scientific Research, and a portion of the work jointly sponsored by the Office of Advanced Research and Technology, National Aeronautics and Space Administration, under Air Force Contract AF 49(638)-1395.

Submitted by:

Charles Sheer  
Principal Investigator

Approved by:

Professor L. H. O'Neill  
Director

## TABLE OF CONTENTS

	<u>Page No.</u>
Abstract	iii
I. Introduction	1
II. Summary of Previously Reported Findings	5
A. The Fluid Transpiration Arc	5
B. The Fluid Convection Cathode	33
C. Techniques	52
D. Radiation Source	89
III. Recent Progress	101
A. Arc Ignition Phenomena	101
B. Radiation Source	129
IV. Bibliography	138

### List of Illustrations

<u>Fig. No.</u>	<u>Caption</u>	<u>Page No.</u>
1	Sketch of FTA	6
2	Axial distribution in positive column of FTA	10
3	Computed radial distributions of heat potential in a 1 atm argon arc column	14
4	Electrical conductivity of 1 atm argon vs. temperature	25
5	Calculated and measured current densities near the anode	29
6	Aparatus used to study effect of forced convection into the column at the cathode constriction	35
7	Radial distribution of magnetic flux density	38
8	Axial potential distribution	40
9	Radial temperature distribution	42
10	Temperature profile of FCC	44
11	Electrical conductivity vs. temperature	46
12	Thermal conductivity vs. temperature	49
13	Dynamic viscosity vs. temperature	51
14	Oscillogram of Hall probe trace	56
15	Radial magnetic field distribution	57
16	Radial current density distribution	58
17	Calibration curves for thermocouple probe in argon	62
18	Oscillograms of thermocouple probe outputs	64

19	Temperature profile of plasmajet measured by thermocouple probe	65
20	First model of transient fiber optics probe	68
21	Schematic diagram of two later models of the transient fiber optics probe	69
22	Oscillogram of radial intensity distribution of FTA positive column	71
23	Comparison of transient and steady state pressure measurements	74
24	Oscillograms of pressure probe traces in cathode column	75
25	Triple cathode arc in swept back geometry	78
26	Arc jet generated by triple-cathode arc assembly	79
27	Single cathode FCC-FTA combination	80
28	Single cathode FCC-FTA combination in operation	81
29	Sketch of conical version of FTA	83
30	Conical FTA in operation	84
31	Cross-sectional distribution of cold flow near anode face (poor specimen)	86
32	Cross-sectional distribution of cold flow near anode face (good specimen)	87
33	Sketch of collinear opposing flow FCC-FTA combination	91
34	Photo of collinear FCC-FTA arc lamp	92
35	Photo of lamp control console	93
36	Schematic diagram of radiation source gas flow system	94
37	Schematic diagram of radiation source water cooling circuits	95
38	Schematic diagram of radiometry arrangement	97

39	Conversion efficiency test results	100
40	Effect of multiple spark ignition	104
41	Current and voltage transients for NC-60 anode and Miller power supply	109
42	Current and voltage transients for 37G anode and Miller power supply	110
43	Current and voltage transients for NC-60 anode and constant current power supply	114
44	Current and voltage transients for 37G anode and constant current power supply	115
45	Flow transients for NC-60 anode	117
46	Frame sequence showing build-up of anode coverage area during ignition	120
47	Area coverage transient for Miller power supply	122
48	Area coverage transient for constant current power supply	123
49	Current density transient for NC-60 anode and Miller power supply	126
50	Arc current variation during programmed ignition sequence	130
51	Tungsten anode surface after ten ignitions with programmed control sequence	131
52	Spectral irradiance of FTA-FCC and vortex- stabilized arc radiation sources	133
53	Micro-brightness profile of FTA-FCC radiation source	137

## I. Introduction

This document is the final report on the work done under Air Force Contract AF 49(638)-1395 for the Mechanics Division of AFOSR. The project extended from April 1, 1964 to March 31, 1969. The general subject matter of the investigation dealt with the study of a DC electric arc subject to forced convection. Its long range objective was to increase fundamental knowledge in arc heater technology. The importance of arc heaters for such practical applications as wind tunnels, materials evaluation facilities, and a variety of other military and industrial uses, has become well recognized in recent years.

This project differs from most other investigations in the area of arc heater technology chiefly in the manner in which the working fluid is injected into the arc. The usual technique employed in these devices is to force the fluid as closely to the arc column as possible while stabilizing the arc against the effects of convection by some form of physical constraint, e.g. thermal, magnetic, fluid vortex, etc. In the present case the fluid is injected through or very close to the electrode-gas boundaries of the discharge which when properly carried out was found to permit relatively high fluid throughput rates without requiring further stabilization of the arc column. It was demonstrated that the injection of fluid via the arc terminations at the anode and/or cathode provides a "free-burning", readily accessible, convective arc system well suited to the study of interaction phenomena be-

tween a gas stream and an arc discharge.

The specific objectives of the project were as follows:

- (1) Develop techniques for practical arc operation with forced convection at anode and cathode.
- (2) Apply appropriate diagnostic techniques to determine experimentally the influence of gas convection on the plasma properties and general arc behavior.
- (3) Devise, if possible, physical models that would explain the observed interaction phenomena with particular emphasis on the anode and cathode regions.
- (4) Investigate the radiation characteristics of the arc subject to convection at both anode and cathode under conditions that optimize conversion of electrical to radiant energy.

Most of the progress made toward the achievement of these objectives has been described in detail in a series of interim progress and technical reports. These are listed in the bibliography as references 1 through 6. The general areas of coverage and the time periods during which the work in each report was carried out is given in the following table.

\* This portion of the work was jointly supported by NASA/OART.

TABLE 1

SUBJECT AND TIME COVERAGE OF INTERIM REPORTS

<u>Report</u>	<u>Subject Coverage</u>	<u>Time Coverage</u>
Ref. 1	Arc instrumentation, diagnostic instrumentation, preliminary findings on anode and cathode convection	4/1/64-9/30/64
Ref. 2	Detailed diagnostic study of anode convection. Preliminary theoretical treatment of column in vicinity of anode.	9/30/64-9/30/66
Ref. 3	Detailed diagnostic study of cathode convection. Probe and spectroscopic data used to derive transport properties with the aid of energy balance equation.	4/1/65-4/1/67
Ref. 4	Development of collinear flow geometry with opposing anode and cathode flow for radiation source investigation. Development of radiometric instrumentation.	1/1/67-6/30/67
Ref. 5	Preliminary testing of radiation source. Development of porous tungsten anodes and preliminary investigation of arc ignition phenomena.	7/1/67-12/31/67
Ref. 6	Measurement of radiation source efficiency and spectral irradiance. Investigation of stability phenomena.	1/1/68-9/30/68

Since the accomplishments in the areas listed in Table 1 have been adequately described in the referenced reports, only brief summaries of the more significant findings will be included here. These are presented in Section II. In Section III the details of the previously unreported results of the

last six months of this project (October 1, 1968 to March 31, 1969) are presented.

## II. Summary of Previously Reported Findings

The accomplishments described in refs. 1 through 6 have been divided for convenience into four subject groups, and summarized in the following:

### A. The Fluid Transpiration Arc (Refs. 1 & 2)

This represents one of the two basic techniques whereby a working fluid may be passed through an arc discharge without further constraints on the arc column. The fluid transpiration arc (more appropriately the fluid transpiration anode), abbreviated "FTA", embodies a porous conductive body which serves as the current receiving positive terminus of the arc column, and through which the gas may be transpired so that it emerges directly into anode sheath region of the arc and thence through the column proper to form an effluent plasma jet. Fig. (1) shows a schematic diagram of this arrangement. Earlier work (7,8) showed that, with proper pore size and permeability, a device of this kind could be operated continuously in argon gas with negligible anode wear and high efficiency (ratio of effluent enthalpy to power input). The high efficiency is attributable to regenerative cooling of the anode and elimination of the need for energy-absorbing constrictor channels. Measurements of arc heating efficiency from 75% to over 90% were demonstrated.

#### (1) Two-Temperature Model

Early results on this project (ref. 1) indicated that the portion of the column adjacent to the anode surface

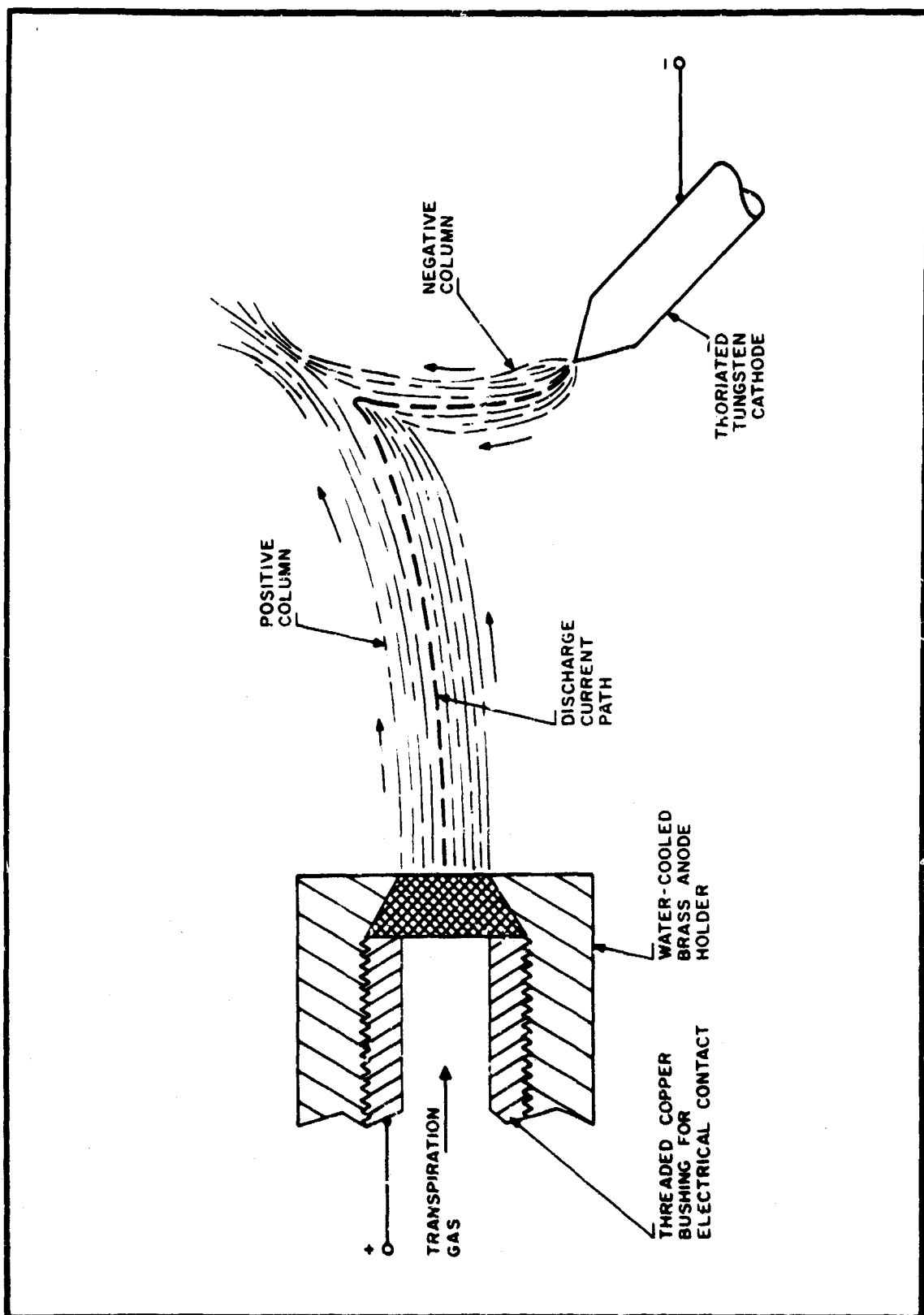


FIG. 1 SKETCH OF FTA

was in a highly non-equilibrium state. The low plasma temperatures near the anode, due to the copious influx of cold gas, was visually evident by the much lower luminosity in this region (anode "dark space"). Later measurements (see Fig. 2) showed that the gas temperature in this region was far below that required for appreciable thermal ionization. Yet measurements of potential distribution (see Fig. 48, ref. 1) indicated unusually high electrical conductivity in this region. In an attempt to provide some insight into this phenomena, various particle relaxation times were calculated using the theory of equilibration based on hard-sphere interactions. Some of the results (Table 3, ref. 2) are reproduced here for reference in Table 2.

TABLE 2  
SUMMARY OF PARTICLE INTERACTION RELAXATION TIMES

<u>INTERACTION</u>	<u>RELAXATION TIME (Sec)</u>
electron-electron	$10^{-11}$
ion-ion	$6 \times 10^{-10}$
ion-atom	$7 \times 10^{-10}$
atom-atom	$2.5 \times 10^{-9}$
electron-ion	$10^{-7}$
electron-atom	$3.2 \times 10^{-6}$

Since the transit time of the free electrons through the positive column is about  $2 \times 10^{-6}$  sec. it is clear from the

very short electron self-relaxation time that the energy received by the electrons from the field is very rapidly equilibrated and we may properly speak of an electron temperature,  $T_e$ . Similarly, since the heavy particle transit times are about  $500 \times 10^{-6}$  sec., we observe that the heavy particle relaxation times are sufficiently short that both an ion temperature,  $T_i$ , and a neutral gas temperature,  $T_g$ , are defined. Referring to the cross-relaxation times, we observe that the ion-atom relaxation time is also short compared to the ion residence time (probably because of the high charge transfer cross-section) so that ions and neutral atoms are essentially equilibrated among themselves in the positive column. In other words

$$T_i \approx T_g.$$

However the important cross relaxation times are those for the electron-atom and electron-ion encounters, since the free electrons carry nearly 100% of the arc current and it is chiefly by electron-heavy particle collisions that energy is transferred from the electric field to the gas. From Table 2 it is clear that these relaxation times are very long compared to the free electron residence time in the column. We conclude that the electrons comprising the drift current to the anode are very weakly coupled to the cold gas emerging from the anode and therefore the zone adjacent to the anode should be characterized by two distinct temperatures, namely a high electron temperature

and a low gas temperature.

In order to verify this conclusion, the axial temperature distribution was measured near the anode. A typical result (see Fig. 55 and 56, ref. 2) is reproduced here for reference in Fig. 2. The electron temperature was measured by determining the absolute intensity of the argon continuum at 5000 $\text{\AA}$ , while the gas temperature was determined by means of a calibrated thermocouple probe used as a heat flux gauge (cf. subsection C, below). The curves in Fig. 2 confirm the pertinence of the two-temperature model, at least for the first 9 mm of the column. \*

## (2) Theoretical Considerations

The attempt to provide a theoretical background for the FTA positive column in accordance with the two temperature model consists of two main parts. The first of these is a rough approximation carried out for the purpose of justifying the use of a one-dimensional model in the sample volume of interest. In this case the energy equation is solved by using a series of piece-wise linear relations between the electrical conductivity and the heat potential, in the manner of Stine and Watson <sup>(9)</sup>, to simplify the treatment.

The simplified form of the energy equation used in the first development is:

\* This accounts for about 40% of the arc gap and 80% of the positive column.

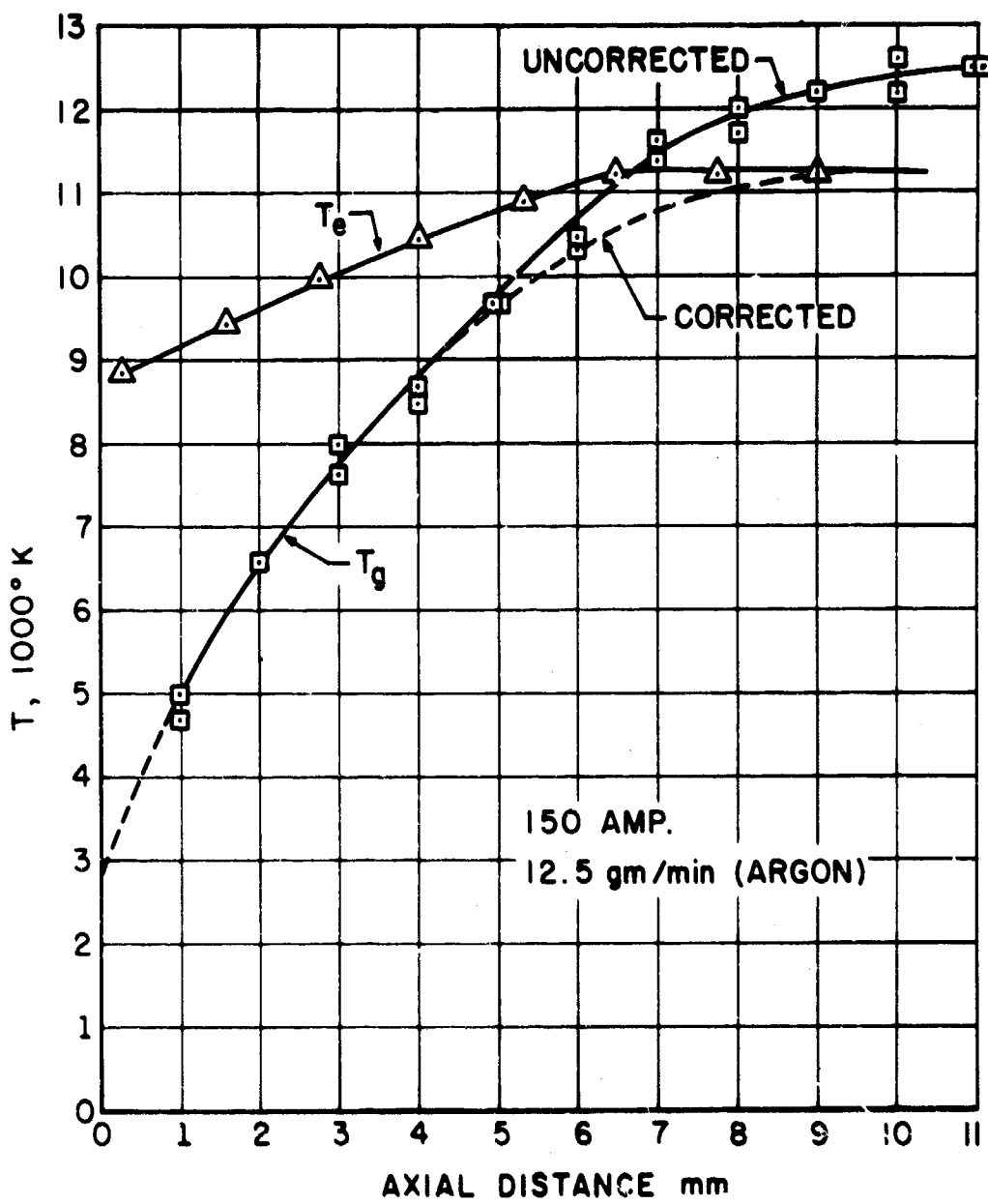


FIG. 2 AXIAL TEMPERATURE DISTRIBUTIONS IN POSITIVE COLUMN OF FLUID TRANSPираATION ARC

$$Q_E = Q_Z + Q_R + Q_{rad}$$

where  $Q_E$  = power generated in the column

$Q_Z$  = power dissipated axially

$Q_R$  = power dissipated radially

$Q_{rad}$  = power dissipated radiatively

For a rough approximation in a 1 atm. argon arc we neglect  $Q_{rad}$ . Energy balance is then expressed in cylindrical coordinates by

$$Q_E = -\frac{\partial}{\partial z} (\lambda \frac{dT}{dz}) + \dot{m} C_p \frac{\partial T}{\partial z} - \frac{1}{\pi} \frac{\partial}{\partial r} (\lambda r \frac{dT}{dr}) \quad (1)$$

where  $T$  = temperature

$z, r$  = axial, radial coordinate

$\lambda$  = thermal conductivity

$C_p$  = specific heat at constant pressure

$\dot{m}$  = mass flow density

The three terms on the right of eq. (1) represent axial conduction, axial convection, and radial conduction respectively. In order to assess the relative importance of axial vs. radial variation in the volume of interest the solution of eq. (1) was undertaken. First, new variables are introduced as follows:

(a) The heat potential:

$$\phi \equiv \int_{T_c}^T \lambda(T) dT \quad (T_c = a \text{ constant})$$

F-1/312

(b) The enthalpy:

$$h \equiv \int_{T_c}^T C_p dT$$

Substituting these in eq. (1) we obtain

$$\frac{\partial^2 \phi}{\partial r^2} + \frac{1}{r} \frac{\partial \phi}{\partial r} + \frac{\partial^2 \phi}{\partial z^2} + Q_E - \sigma \frac{\partial h}{\partial z} = 0 \quad (2)$$

We make the approximations:

$$\sigma \approx A_\sigma \phi + B_\sigma$$

$$h \approx A_h \phi$$

where  $\sigma$  = electrical conductivity

and

$A_\sigma, B_\sigma, A_h$  = constants.

Using these relations and assuming that the Joule heating  $Q_E =$

$Q_0$  = constant in the column, we obtain from eq. (2)

$$\frac{\partial^2 \phi}{\partial r^2} + \frac{1}{r} \frac{\partial \phi}{\partial r} + Q_0 - A_h \sigma \frac{\partial \phi}{\partial z} = 0 \quad (3)$$

where we have neglected the axial conduction term ( $\partial^2 \phi / \partial z^2$ )  
subject to a posteriori verification.

Substituting in eq. (3) the relations

$$\phi(r, z) = u(r) e^{-\alpha^2 z}$$

and  $\rho = r/r_c$  ( $r_c$  = column radius)

we obtain

$$\frac{d^2 u}{d \rho^2} + \frac{1}{\rho} \frac{du}{d\rho} + \beta^2 u + Q_0 r_c^2 = 0 \quad (4)$$

$[\beta^2 = \alpha^2 A_h \sigma r_c^2]$

which is seen to be the zero order Bessel equation.

The solution to eq. (4) is given by

$$\phi = \frac{r_c^2 Q_0}{4} \left[ (1 - \rho^2) - 8 \sum_{m=1}^{\infty} \frac{J_0(\beta_m \rho) e^{-\alpha_m^2 z}}{\beta_m^3 J_1(\beta_m)} \right] \quad (5)$$

Some values of  $(4\phi/r_c^2 Q_0)$  as a function of  $\rho$  have been computed from eq. (5) and plotted in Fig. 3 with different parametric values of  $\alpha_m^2 z$ . The curves give a semi-quantitative picture of the extent of the region in which a quasi-one dimensional variation can be presumed to prevail. We observe that for  $\alpha_m^2 z = 0.1$  the distribution is essentially radially invariant to approximately  $\rho = 0.8$ . As  $z$  increases the effects of the radial gradient at the boundary propagate towards the center. Thus, for  $\alpha_m^2 z = 0.4$ , the flat portion extends only from the axis to  $\rho = 0.4$ . Using the values:

$$A_h = 250 \text{ cm-sec/gm} \text{ (from published argon temperature-enthalpy data)}$$

$$\dot{m} = 0.2 \text{ gm/sec-cm}^2 \text{ (lowest mass flow density used in experiments)}$$

$$r_c = 0.5 \text{ cm. (average experimental value)}$$

we find for  $\rho = 0.4$

$$z = \frac{0.4 A_h \dot{m} r_c^2}{2.4} = 0.9 \text{ cm.}$$

We conclude that for 0.9 cm downstream of the anode, and for the central portion of the column, at least 0.4 cm in diameter, the

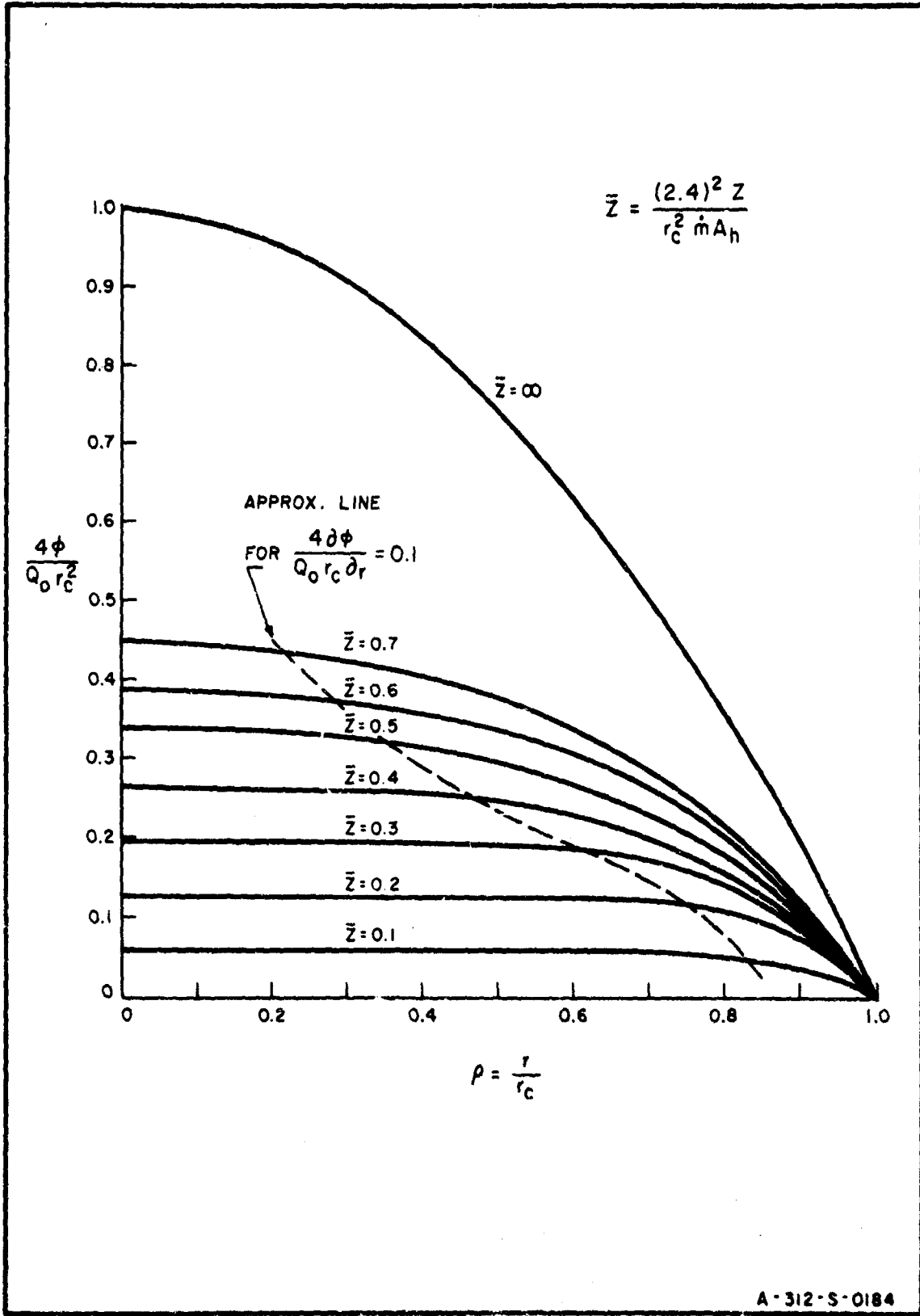


FIG. 3 COMPUTED RADIAL DISTRIBUTIONS OF HEAT POTENTIAL FOR 1 ATM. ARGON ARC WITH INTERNAL HEAT SOURCE  $Q_0$

assumption of quasi-one dimensionality with  $\partial/\partial r = 0$  is valid.\* Obviously for higher  $m$  the region will extend further. In any case the region is sufficiently large for convenient probe and other diagnostic techniques so that the experimental data may be restricted to the one-dimensional region. Incidentally from eq. (5) the neglect of the axial heat conduction term

( $\frac{d^2\phi}{dz^2} = 0$ ) is easily justified.

The second part of the theoretical treatment concerns the calculation of the electrical conductivity and electron-heavy particle energy transfer rates in the sample volume, using the two-temperature model and the simplification of quasi-one dimensionality. Having established that the individual particle distribution functions are very close to Maxwellian (low E/p or "weak field" assumption) the macroscopic equations for the transfer of momentum and kinetic energy in a three-component fluid can be written as (10)

Momentum Equation:

$$m_e m_e \frac{D\vec{U}_e}{Dt} = m_e e \vec{E} + \nabla P_e - \sum_s m_e m_s \nu_{es} (\vec{U}_e - \vec{U}_s) \quad (6)$$

Energy Equation:

$$m_e m_e \frac{DT_e}{Dt} = \frac{2}{3} T_e \frac{D(m_e m_e)}{Dt} - \sum_s m_e m_s \nu_s \left[ \frac{2m_e}{m_e + m_s} (T_e - T_s) - \frac{2}{3k} \left( \frac{m_s m_e}{m_s + m_e} \right) |\vec{U}_e - \vec{U}_s|^2 \right] \quad (7)$$

\* Note that this differs from the quasi-one dimensionality of the fully-developed column of the wall-stabilized arc, wherein  $\partial/\partial z = 0$  but gradients are appreciable in the radial direction.

where:

$\nu_{es}$  = collision frequency of electrons with heavy particles

$$= \frac{4\pi(m_s m_e)^{1/2}}{3m_e(2\pi k)^{3/2} k} \cdot \frac{\int_0^{\infty} T_{es} g^5 e^{-Kg^2} dg}{(m_s + m_e)(m_s T_e + m_e T_s)^{5/2}} \cdot n_s$$

$g$  = relative velocity between electrons and heavy particles

$m$  = particle mass

$T$  = temperature

$k$  = Boltzmann's constant

$$K = \frac{m_e m_s}{2k(T_e m_s + T_s m_e)}$$

$T_m$  = collision frequency for momentum transfer between electrons and heavy particles

$$= \int (1 - \cos \Theta) T_{es}(g, \Theta) d\Omega$$

$\Theta$  = scattering angle

$d\Omega$  = increment of solid angle

$U$  = drift velocity

subscript "e" refers to free electrons

subscript "s" refers to either ions or neutral atoms (heavy particles)

and  $\frac{D}{Dt}$  = the convective derivative.

Equations (6) and (7), which are written for electrons, are in general complemented by two analogous sets of equations for the ions and atoms.

Making use of the one-dimensionality discussed above (radial and azimuthal invariance), restricting the analysis to steady state only, and using the weak field approximation, major simplifications of eqs. (6) and (7) are permissible.

Thus we may put

$$\frac{\partial}{\partial r} = \frac{\partial}{\partial \theta} = 0 \quad \text{and} \quad \nabla = \frac{d}{dz}$$

Also in steady state  $\frac{\partial}{\partial t} = 0$  and the convective derivative

becomes

$$\frac{D}{Dt} = U_e \frac{d}{dz}$$

In addition, because of the low electric field to pressure ratio existing in the sample volume,  $U_i$  and  $U_a$  may be neglected compared to  $U_e$ , and because  $\frac{m_e}{m_s} \ll 1$ , only  $T_e$  remains, excepting the terms involving  $T_e - T_s$  in eq. (7). Finally the electron inertia term on the left hand side of eq. (6) is negligible since the very light "electron fluid" is resistance and not inertia limited.

Inserting these simplifications in (6) and (7), we obtain:

$$n_e e E = - \frac{d P_e}{dz} + \sum_s m_e n_e \nu_{es} U_e \quad (8)$$

$$m_e n_e U_e \frac{dT_e}{dz} = \frac{2 m_e T_e}{3} U_e \frac{d n_e}{dz} \sum_s m_e n_e \nu'_s \\ \left[ \frac{2 m_e}{m_s} (T_e - T_s) - \frac{2}{3k} m_e U_e^2 \right] \quad (9)$$

where  $E$  = electric field

$$p = \text{pressure}$$
$$v_{es} = \frac{1}{3} \sqrt{\frac{2}{\pi}} \left( \frac{m_e}{k T_e} \right)^{5/2} \cdot M_s \cdot \int_0^{\infty} g^5 e^{-Kg^2} dg$$

and

$$K = \frac{m_e}{2 k T_e}$$

Since eqs. (6) and (7) and hence (8) and (9), were derived originally from the Boltzmann equation, (see ref. 10), the possible influence of inelastic collision processes has thus far been neglected. This is justifiable for the momentum equation, (8), owing to the weak field approximation for which the very low value of drift momentum precludes any significant amount of inelastic events. The same conclusion is not immediately justifiable for the energy equation, (9), because of the possibility of ion-electron recombination. Purely radiative recombination in a relatively optically thin plasma (such as the sample volume of interest) represents a minor ( $< 5\%$ ) energy loss, as pointed out by Emmons. (11) However three body recombination processes are possible in which part of the ionization energy is carried off by increased kinetic energy of the third particle. The ionization energy  $eE_i$  ( $e$  = electron charge,  $E_i$  = ionization potential), which is released by recombination is 15.76 volts for argon. Since the average thermal kinetic energy per particle at  $7730^\circ K$  is only one volt it is clear that, even if a small fraction of the ionization energy is transferred to the electron gas by the

three body recombination process, the influence of this inelastic process could not be neglected.

The additional energy release due to recombination may be accounted for adding the term

$$-\left(\frac{3}{2}T_e + \frac{eE^*}{k}\right)\left(\frac{\partial n_e}{\partial t}\right)_{rec.}$$

to the left hand side of eq. (7);

where  $eE^*$  = portion of the ionization energy transferred to the electron gas by ion-electron recombination \*\*

$\left(\frac{\partial n_e}{\partial t}\right)_{rec.}$  = rate of electron concentration decrease due to recombination

We amend eq. (9) accordingly to obtain

$$\begin{aligned} m_e U_e \left[ \frac{3}{2} m_e \frac{dT_e}{dz} - T_e \frac{dn_e}{dz} \right] + \left( \frac{3}{2} T_e + \frac{eE^*}{k} \right) \left( \frac{\partial n_e}{\partial t} \right)_{rec.} \\ = \sum_s m_e m_s \nu_{es} \left[ \frac{3m_e}{2m_s} (T_e - T_s) - \frac{m_e U_e^2}{k} \right] \quad (10) \end{aligned}$$

Although eqs. (8) and (10) are much more tractable than (6) and (7), they do not represent a complete solution since there are only two equations containing six unknowns ( $m_e, T_e, E, U_e, T_s, m_s$ ). We invoke the perfect gas law and the

\*\* The value of  $E^*$  for argon has been given by Gushinow et al (12) as 1.5 ev., i.e. about 10% of the energy released by recombination.

charge conservation equation to obtain two more relations, viz:

$$n = n_a + n_i + n_e = n_a + 2n_e = \frac{p}{kT_a} \quad (11)$$

(which implies quasi neutrality and single ionization)

and

$$\nabla \cdot n_e \vec{U}_e = - \left( \frac{\partial n_e}{\partial t} \right)_{rec.}$$

which for the one-dimensional case we are considering is easily shown to be of the form:

$$\left( \frac{\partial n_e}{\partial t} \right)_{rec.} = \frac{n_e}{n} U_e \left( \frac{\partial n_e}{\partial z} \right) + n_e \left( \frac{\partial U_e}{\partial z} \right) + \frac{n_e U_e}{A} \left( \frac{\partial A}{\partial z} \right) \quad (12)$$

where  $A$  = cross-sectional area of the column

If, now we consider that  $T_s$  is given, i.e., experimentally determined, we need only one more equation to have a complete set of equations suitable for calculating plasma parameters in the sample volume. To provide this equation we make use of the following equation from statistical mechanics

$$N_e N_i / N_a = Z_e Z_i / Z_a$$

where  $N$  = total number of particles of a given species in a volume  $V$

$Z$  = partition function of the respective particles

Since each species has been shown to possess a defined temperature, we can substitute in the above the following well-known formulas:

$$Z_e = 2(2\pi m_e k T_e)^{3/2} V/h^3$$

$$Z_i = (2\pi m_i k T_i)^{3/2} V Z_{i(\text{elec})}/h^3$$

$$Z_a = (2\pi m_a k T_a)^{3/2} V Z_{a(\text{elec})}/h^3$$

where  $Z_{s(\text{elec})}$  represents the partition functions for electronic excitation of the ions and atoms respectively.

This leads to the relation

$$\frac{m_e m_i}{m_a} = 2(2\pi m_e k T_e/h^3) \left( m_i T_i / m_a T_a \right)^{3/2} \left( Z_{i(\text{elec})} / Z_{a(\text{elec})} \right) \quad (13)$$

Substituting in (13) the values of  $Z_{s(\text{elec})}$  for argon as given by Bond (13) we obtain finally

$$\frac{\alpha^2}{1-\alpha^2} = \left( \frac{3.27 \times 10^{-7} T_a}{P_{ai}} \right) \left( \frac{2(4+2e^{-2062/T_e})}{1+60e^{-162500/T_e}} \right) T_e^{3/2} e^{-183000/T_e} \quad (14)$$

where  $\alpha = m_e/(m_e + m_a)$  = the fractional ionization  
and  $P_{ai} = (m_a + m_i) k T_a$

In deriving eq. (14) loss of ion-electron pairs by lateral diffusion has been neglected. This can be justified by solving the diffusion equation under the appropriate conditions, which shows that the diffusion current is quite negligible compared to the drift current.

### (3) Comparison of theory and experiment

Equations (8), (10), (11), (12) and (14) represent a reasonably tractable theoretical framework from which the properties of the FTA positive column should be predictable with the aid of an empirically determined temperature distribution. Complete solution of these equations was not carried out, mainly because of the uncertainty in some of the parameter values and in several of the boundary conditions. Further investigation to resolve this uncertainty is required before a complete solution is warranted.

However, the two-temperature electrical conductivity, current density, and energy transfer from electrons to heavy particles, were calculated from the above set of equations and compared to experimental data, with the following results:

#### (a) Electrical conductivity

The electrical conductivity is given by

$$\sigma = \frac{J}{E} = \frac{e^2 n_e}{\sum_s m_e \nu_{es}} \quad (15)$$

Eq. (15) is obtained by manipulating eqs. (8) and (9). It indicates that one needs only the cross-sections for momentum transfer between electrons and each of the heavy particles ( $\sigma_M^{es}$ ) in order to substitute a relation for  $\nu_e$ , containing only  $T_e$  (see eq. (9)). For convenience we calculate the electrical resistivity by inverting eq. (15) to get

$$\eta = \frac{E}{J} = \frac{m_e}{e^2 M_e} (\nu_{ei} + \nu_{ea})$$

For we use the well known Spitzer and Härn formula (14) which evaluates  $\sigma_{ei}$  by assuming the Coulomb interaction cut-off to be equal to the Debye length, and which yields for the electron-ion resistivity

$$\nu_{ei} = 65.3 \frac{\ln \Lambda}{T_e^{3/2}} \text{ ohm-m.}$$

where the Coulomb logarithm is given by

$$\ln \Lambda = \ln \left[ \frac{12\pi(\epsilon_0 k T_e / e^2)^{3/2}}{M_e^{1/2}} \right]$$

For the electron-atom resistivity the situation is more complicated. In the evaluation of the collision frequency,  $\nu_{ea}$ , the usual assumption of the hard sphere model to obtain  $\sigma_m^{ea}$  for the integral

$$\int_0^\infty \sigma_m^{ea} g^5 e^{-Kg^2} dg$$

leads to too great an error due to the pronounced minimum in cross-section characteristic of the heavier noble gases. For argon this occurs at  $\sim 0.5$  ev which is in the middle of the temperature range of interest. The value of  $\sigma_m^{ea}$  has fortunately been measured experimentally in the range of 0.02 to 20 ev by

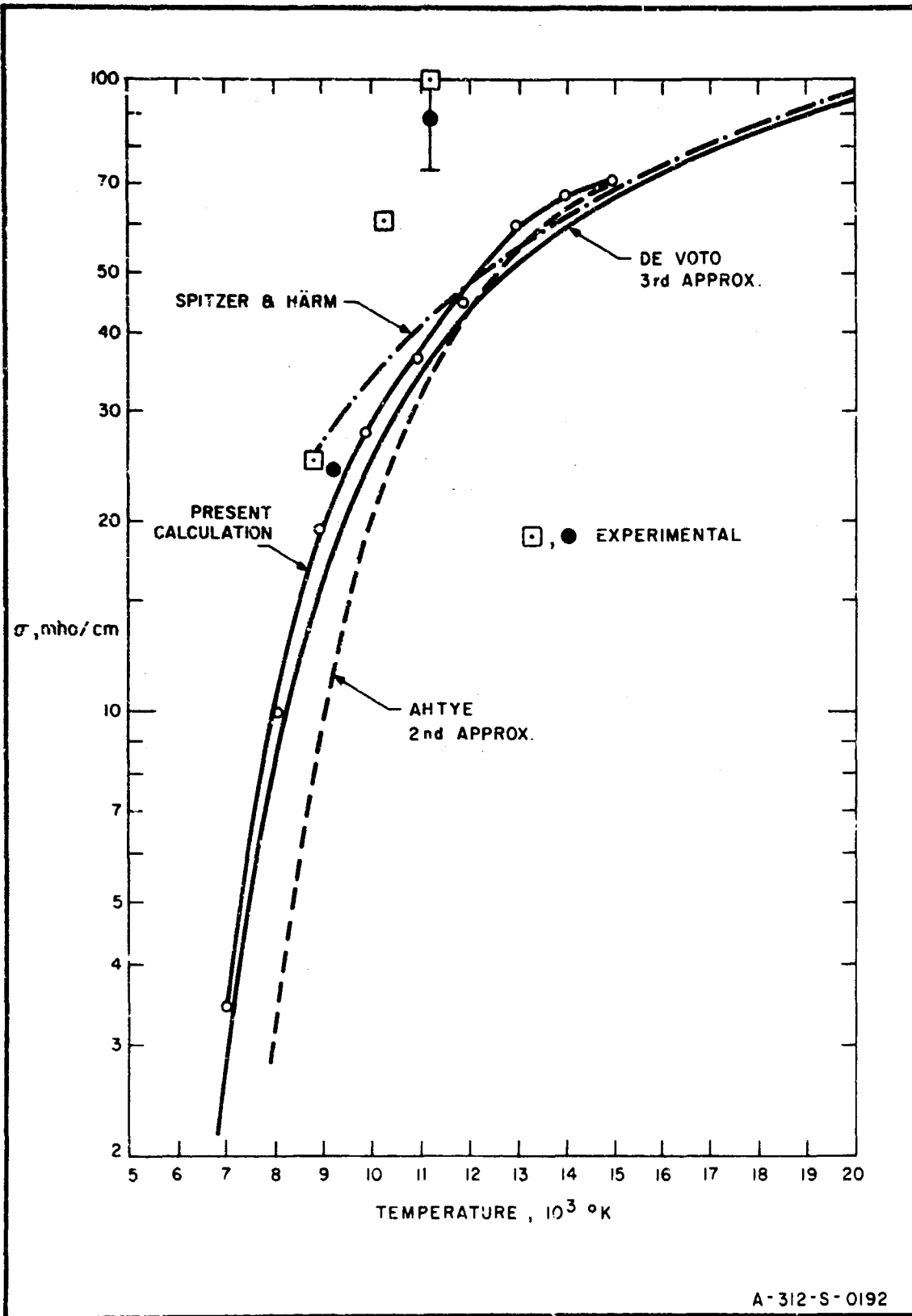
Engelhardt and Phelps<sup>(15)</sup> and was therefore available for a numerical computation. The result for the electron-atom resistivity is

$$\eta_{ea} = 1.04 \times 10^{-6} (M_a/n_e) (T_e/10,000)^{1.8} \text{ ohm-m.} \quad (18)$$

Taking the sum of eqs. (17) and (18) we obtain

$$\eta = \eta_{ei} + \eta_{ea} = 65.3 \frac{\ln \lambda}{T_e^{3/2}} + 1.04 \times 10^{-6} (M_a/n_e) (T_e/10^4)^{1.8} \text{ ohm-m.} \quad (19)$$

Equation (19), plotted as conductivity for ease of comparison to other results, is shown in Fig. 4, along with computations of Spitzer and Härn<sup>(14)</sup>, Ahtye<sup>(16)</sup> and de Voto<sup>(17)</sup>, and several experimental values of conductivity obtained by measuring the current density and field gradient in the FTA column. For the present calculation, the values of  $n_3/n_e$  were obtained from eq. (14). It is seen that at the lower temperatures the experimental values agree fairly well with the calculated values but at higher temperatures are greater than the closest theoretical curve by a factor of two or so. Two reasons are possibly responsible for this discrepancy. One is due to a prominent axial peak in the current density distribution (as measured by a transient Hall probe technique) which is more pronounced in the higher temperature region downstream of the anode (see Figs. 52 and 53, ref. 2). Assuming these



A-312-S-0192

FIG. 4 ELECTRICAL CONDUCTIVITY OF 1 ATM. VS. TEMPERATURE

are not real and smoothing out the measured curve brings the experimental values down to the lower end of the range indicated at the point near the top of Fig. 4. The second is the probable need for a correction to the Coulomb logarithm as indicated by Schweitzer and Mitchner<sup>(18)</sup>. When applied to the calculated points near 12,000°K, the discrepancy between theory and experiment is still further reduced (not shown in Fig. 4). The experimental uncertainty in  $J$  must be removed and the theoretical evaluation of the Coulomb cross-section further refined before a valid comparison can be made.

(b) Current density

Referring to eq. (10) (energy equation)

we recognize the four terms on the left as (1) the change in kinetic energy of the electrons due to axial temperature gradient, (2) the fluid mechanical volume work done by electrons due to an axial electron density gradient, and (3) plus (4) as the kinetic energy dumped into the electron gas due to three body electron-ion recombination. These are balanced by the two terms on the right which are evidently (1) the kinetic energy transfer due to temperature differences among the species and (2) the Joule heating term. Since the experimental curve for  $T_e$  vs.  $z$  (Fig. 2) and the curve for  $M_e$  vs.  $z$  derived from Fig. 2 and eq. (14) both show only gradual axial variations in  $T_e$  and  $M_e$ , we can in a first approximation assume a homogenous plasma ( $dT_e/dz = dn_e/dz = 0$ ) and neglect

the first two terms on the left of eq. (10). Also a calculation of the recombination energy \* shows that this source is also negligible compared to the Joule heating. This means that the Joule heating is balanced only by the temperature difference heat transfer, which means that the right hand side of eq. (10) is equal to zero.

Thus:

$$\sum_s m_e n_e v_e \left[ \frac{3m_e}{m_s} (T_e - T_s) - \frac{m_e U_e^2}{k} \right] = 0$$

or

$$\sum_s \frac{3k(T_e - T_s)}{m_s} = U_e^2 = J^2 / e^2 n_e^2$$

And since the heavy particles have essentially the same masses and temperatures,

$$J = n_e e \sqrt{3k(T_e - T_s)/m_s} \quad (20)$$

which is the compatibility relation due to Vlasov <sup>(19)</sup> and used by Kerrebrock <sup>(20)</sup> for his two-temperature model of the conductivity of seeded plasmas.

\* Using the value  $eE^* = 1.5$  ev (ref. 12) the total recombination power was estimated at 5 watts or about 0.1% of the Joule heating. See ref. (2) pp. 179-180.

In order to compare theory and experiment values of current density were computed by means of eq. (20) in the region where  $T_s$  is significantly lower than  $T_e$ , using the measured axial temperature distributions (Fig. 2) to obtain  $T_e - T_s$ , and calculating  $M_e$  with the aid of eq. (14). The results are compared to values of  $J$  measured directly by the Hall magnetic probe in the same region. Both curves are plotted in Fig. 5. It is seen that there is profound discrepancy between the calculated and measured current densities. Moreover the magnitude of the discrepancy is far greater than any conceivable experimental error either in  $J$  or in  $T_e$  and  $T_s$ . The only conclusion that appears possible is that eq. (20) is invalid. This does not mean that energy is not conserved. In fact energy balance is reasonably closely satisfied as may be shown by comparing the Joule heating with the convected gas energy. Thus if  $P_e$  = electrical power input (Joule heating) and  $P_g$  = the converted gas power then

$$P_e = EJ$$

and  $P_g = \dot{m} \frac{dH}{dT_g} \frac{dT_g}{dz}$

Using observed values of  $E$ ,  $J$ ,  $\dot{m}$  and  $T_g$  and published data for  $\partial H / \partial T$  for argon at 1 atm. both  $P_e$  and  $P_g$  were computed.

The results are listed in Table 3.

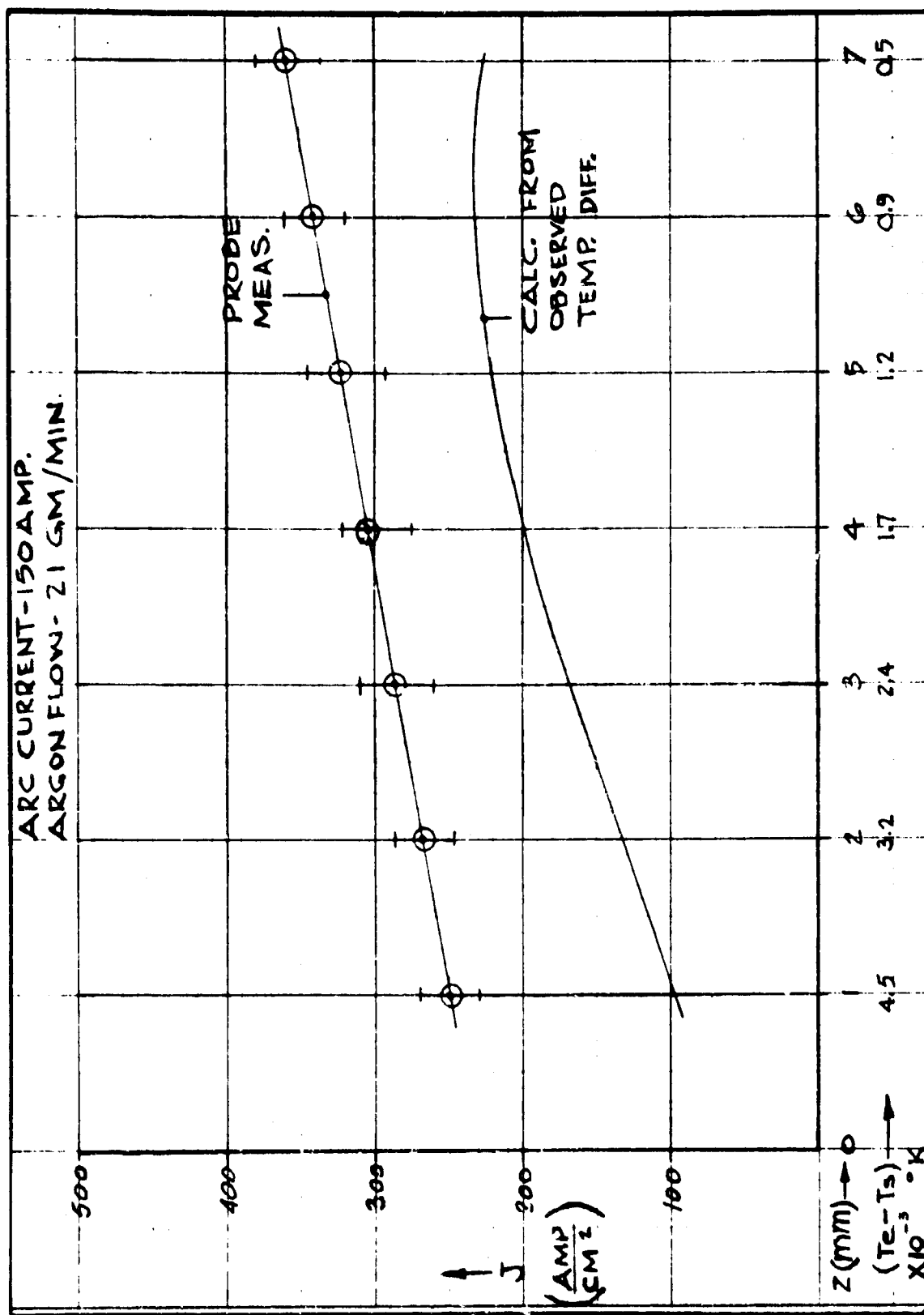


FIG. 5 CALCULATED AND MEASURED AXIAL CURRENT DENSITIES NEAR THE ANODE (1 ATM. ARGON)

Table 3

Comparison of Joule Heating and Convected Gas Energy

(150 amps; 21 gm/min. argon)

<u>Z (mm)</u>	<u>P<sub>g</sub> (KW/cm<sup>3</sup>)</u>	<u>P<sub>e</sub> (KE/cm<sup>3</sup>)</u>
1	2.04	2.63
2	2.0	2.39
3	1.96	2.2
4	1.87	1.89
5	2.1	1.86
6	2.39	1.98
7	3.12	2.24

Considering the neglect of radiation and other minor terms in the energy equation and the experimental error, the agreement is good enough to stipulate that on the whole energy is conserved in the FTA positive column.

(c) Energy transfer rates

From the right hand side of eq. (10) we obtain the expression for the energy transfer rates from electrons to heavy particles:

$$P_{es} = 2m_e \nu_{es} (m_e/m_s) (3/2) k (T_e - T_s)$$

which yields for the electron-ion heat transfer

$$P_{ei} = 2.03 \times 10^{-23} n_e^2 \ln \Lambda (T_e - T_i) / T_e^{3/2} \quad (21)$$

and for the electron-atom heat transfer

$$P_{ea} = 1.65 \times 10^{-41} M_e M_a (T_e / 10^4)^{1.8} (T_e - T_a) \quad (22)$$

Eqs. (21) and (22) were used to evaluate the heat transfer between electrons and heavy particles near the FTA anode with the results shown in Table 4.

Table 4  
Comparison of Energy Transfer Rates with Energy Input Rates  
(150 amps; 21 gm/min. argon)

<u>Z (mm)</u>	<u>P<sub>ea</sub></u> (KW/cm <sup>3</sup> )	<u>P<sub>ei</sub></u> (KW/cm <sup>3</sup> )	<u>P<sub>ea</sub> + P<sub>ei</sub></u> (KW/cm <sup>3</sup> )	<u>P<sub>e</sub></u> (KW/cm <sup>3</sup> )
1	0.83	1.31	2.14	2.63
2	0.72	2.0	2.72	2.39
3	0.71	3.12	3.83	2.2
4	0.71	4.6	5.31	1.89
5	0.66	6.13	6.79	1.86
6	0.65	8.25	8.90	1.98
7	0.47	7.4	7.87	2.24

From Table 4 it is seen that  $P_{ea}$  accounts for approximately a third of the power received by the electrons from the field ( $P_e$ ). The total energy transferred from the electrons to the heavy particles ( $P_{ea} + P_{ei}$ ) is consistent with  $P_e$  only for the first 2mm. of the column. Beyond that the large values of  $P_e$  indicated by theory are clearly erroneous. It is significant that the region of consistency between  $P_{ea} + P_{ei}$  and  $P_e$

is the low temperature part of the column (anode dark space) where the measured values of the electrical conductivity are consistent with the predictions of theory (see Fig. 4).

Further along the column, i.e. when  $T_g > \sim 7000^\circ K$ , both the conductivity and the energy transferred in electron-ion collisions, as calculated from theory, show significant discrepancies. In addition eq. (20) is inconsistent in all portions of the column.

A possible reason for the above results is the fact that they are based on erroneous assumptions in the calculation of collision frequencies. Eq. (20) for example was derived on the basis that the cross-section for momentum transfer is the same as for energy transfer. Under the conditions prevailing in the FTA arc column, it is possible that these are not the same. Existing theories for dense (1 atm) plasmas are all represented as applicable only to the order of the Debye screening theory<sup>(21)</sup>. This implies a fairly large number of electrons in a Debye sphere, e.g.  $n_D \geq 100$ . In our case  $n_D$  is not more than 10 and as low as 3. Under these conditions the entire concept of Debye screening would appear to lose significance. In particular the collision frequency for the electron-ion interaction would not be properly given by the Spitzer-Härm equation and the results for  $\eta_{ei}$  and  $P_{ei}$  would then be different from those calculated here. The present results seem to indicate that the electrons are energetically more insulated from the ions than is calculated from the more conventional Coulomb interaction.

In any case the two temperature model itself is not vitiated by this situation. The wide differences in  $T_e$  and  $T_s$  in the FTA column are amply demonstrated by the measurements. The relatively low volume rate of energy transfer from hot electrons to relatively cold atoms and ions is an essential requirement for the observed physical situation in which a large current is conducted through a column of gas whose heavy particle temperature is too low to account for the observed conductivity.

Future theoretical work on this phenomenon should feature the development of a plasma kinetic theory pertinent to the situation in which  $M_D$  is very low. This is admittedly a very difficult task since it involves a many-body problem; i.e. one with more than two interacting particles but too few for statistical treatment to be valid.

#### B. The Fluid Convection Cathode (Refs. 1 & 3)

This is the second technique whereby a fluid is injected into an arc column at an arc termination spot - in this case the cathode spot - without constraints on the column proper. In other words, the fluid convection cathode arc (abbreviated henceforth "FCC), like the FTA establishes a "free-burning" arc. Both techniques have the common advantage that the arc operates very stably despite the forced convection of considerable quantities of working fluid and without the necessity for water-cooled constrictor channels. This in

turn provides the benefits of high heating efficiency and virtually complete accessibility for probe and optical diagnostics.

A sketch of the apparatus used to study the FCC arc is given in Figure 6. The conical cathode tip is surrounded by a closely spaced conical nozzle so that the gas is projected as a thin relatively high speed layer into the arc column very close to the cathode spot. The influence on an arc column of gas flow controlled by an annular nozzle surrounding the cathode was also studied by Busz-Peukert and Finkelnburg (22). The main difference between their system and that of the present work lies in the use of a much more tightly shrouded cathode nozzle in our case, which provides a more localized and higher velocity flow field.

(1) Diagnostic Program

Preliminary qualitative observation of the FCC showed that this type of nozzle produced a very stable arc over a wide range of gas convection rates and operating parameters. A convenient range of parameters was therefore chosen for this work. Arc currents were usually set at 150 amp or 200 amp and the arc gap at 3 cms. The resulting arc voltages were usually in the range of 40 to 70 volts (depending primarily on injection velocity). For most of the measurements a total convection rate of  $\dot{m} = 0.2 \text{ gm/cm}^2\text{-sec}$  was used. A parameter which was found to have an important influence on the operation of the FCC is the mass flow density referred to

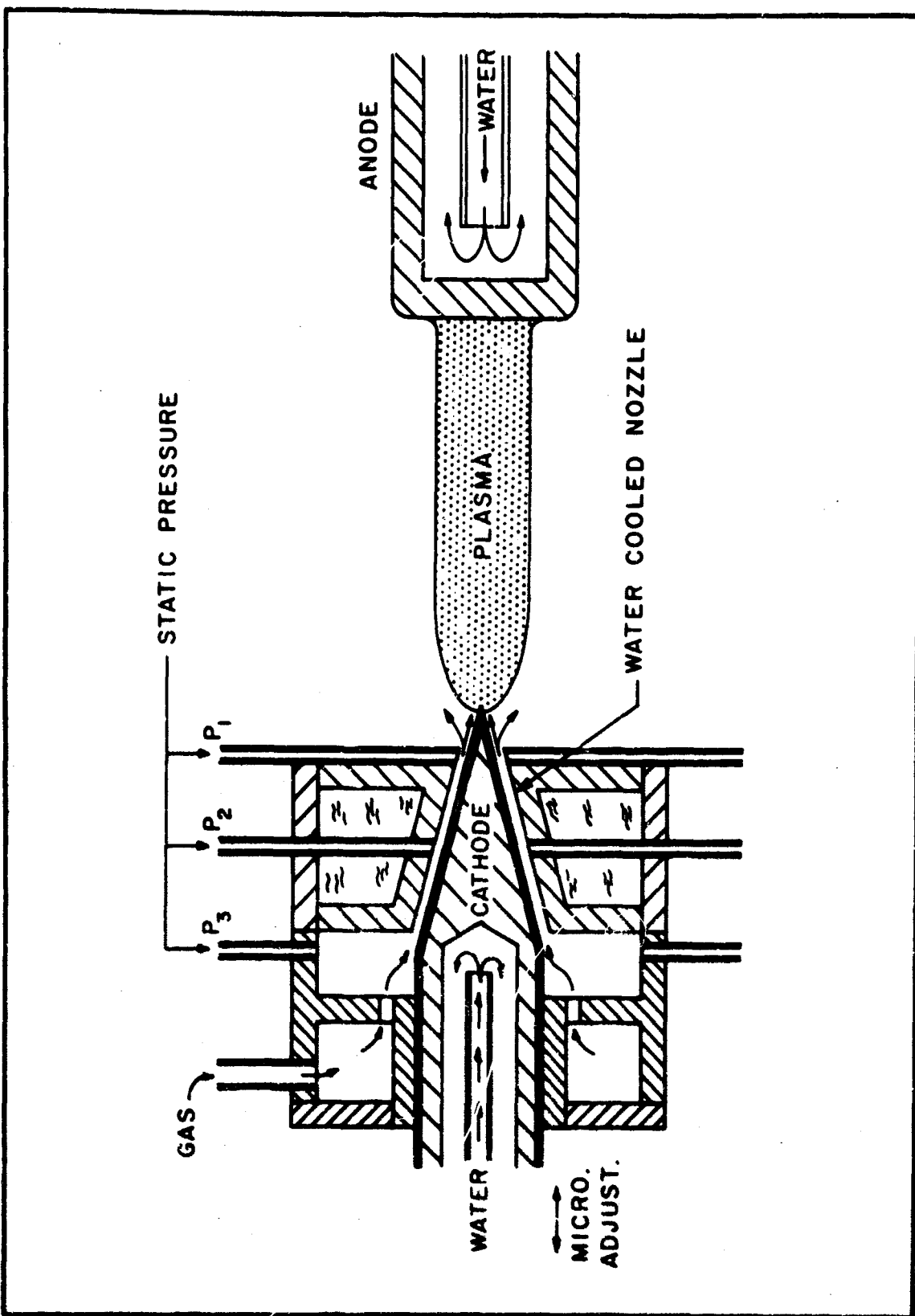


FIG. 6 APPARATUS USED TO STUDY EFFECT OF FORCED CONVECTION INTO COLUMN AT THE CATHODE CONSTRICION

the nozzle orifice, defined as

$$\xi \equiv \frac{\dot{m}}{A} = \rho w$$

where:

$A$  = area of annular nozzle orifice

$\rho$  = gas density at nozzle orifice

$w$  = gas velocity at nozzle orifice

It is evident that  $\xi$  is a measure of the momentum per unit volume of the convected gas stream at the moment of impingement on the column. Due to the convergent nature of the flow it is clear that the column experiences a constriction in the region just beyond the cathode tip because of the inwardly-directed radial component of the gas momentum. This constriction has a considerable influence on arc behavior, an example of which is described below. Hence since the amount of constriction depends on  $\xi$ , separate measurements were made parametric in  $\xi$ , the values used being 2.5, 5.0, and 20 gm/cm<sup>2</sup>-sec, respectively. The axial component of the gas momentum serves to stabilize the arc on the axis of symmetry. There is of course no azimuthal component for the type of nozzle used.

The measurements were made by various transient probe techniques and, in the case of temperature, by the conventional spectroscopic method. These are more fully discussed in refs. 1, 2, 3 and 25. The quantities measured were the potential distribution in the column which yields the field

strength  $E$ , the self-magnetic field for the evaluation of the current density,  $J$ , and the temperature distribution. The distribution of mass flow density at points in the column beyond the cathode were also measured, using a small transient Pitot tube, this measurement being required for the determination of dynamic viscosity. The complete distribution in the column was obtained by measuring radial distributions at various axial stations between anode and cathode, the measurements at each station being repeated for the several values of the injected mass flow density. Complete details of the diagnostics program are given in ref. 3. A few of the results are presented here for reference in the following.

(a) Current density

The current density was obtained from the radial distribution of the self-magnetic field which in turn was measured by a small Hall element sensor enclosed in a water-cooled envelope and swept rapidly through the column in the radial direction. This provides a direct evaluation of the magnetic induction,  $B(r)$ , due to the arc current. The data are obtained in the form of an oscillogram giving  $B(r)$  as a function of  $r$ . The raw data are considerably in error mainly due to the size of the Hall probe, compared to the column diameter. The magnitude of the resulting perturbation was calculated and a correction factor arrived at to compensate for this error. A typical case is shown in Figure 7.

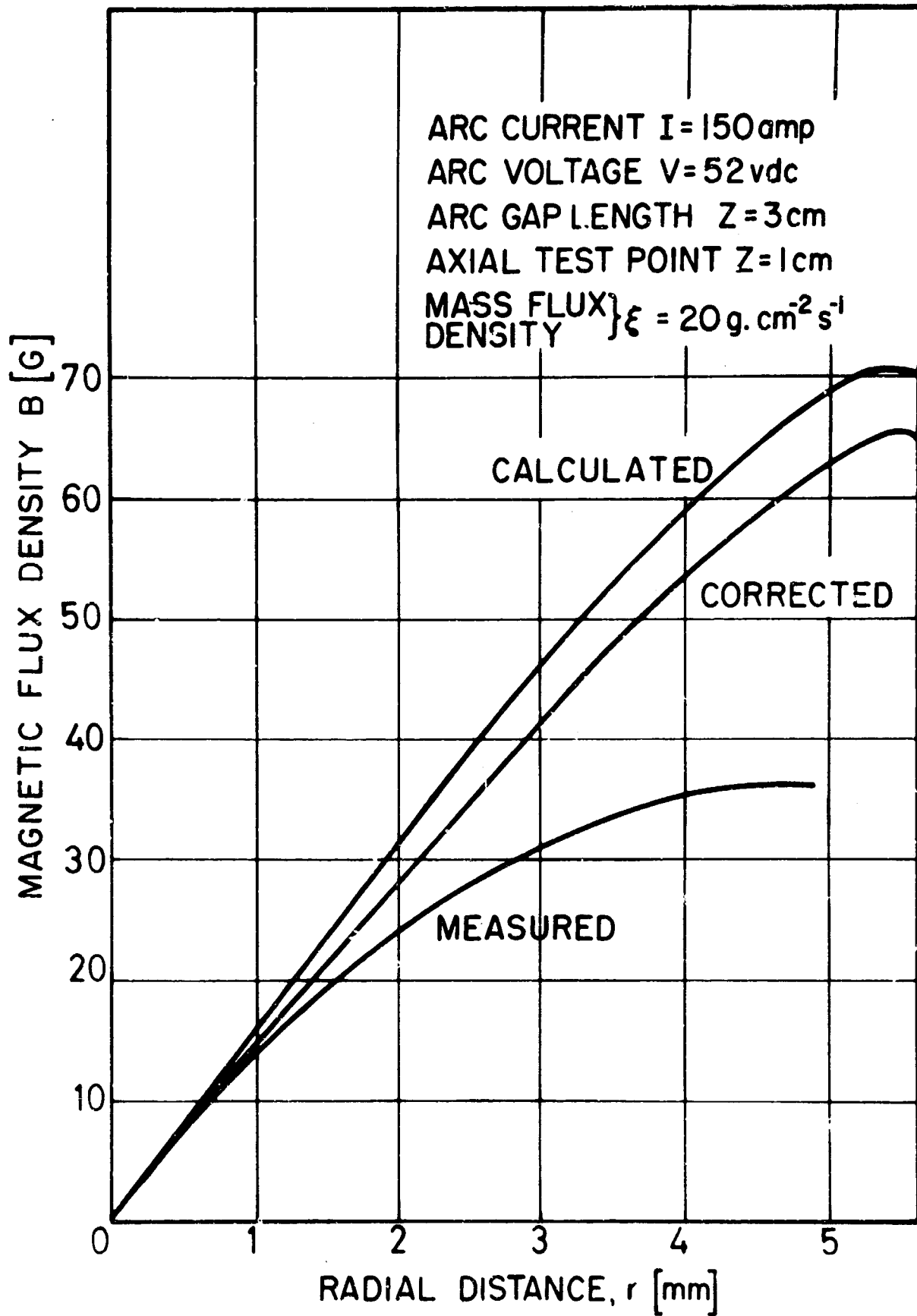


FIG. 7 RADIAL DISTRIBUTION OF MAGNETIC FLUX DENSITY IN A FREE BURNING ARGON ARC

From the corrected curve of  $B(r)$  vs.  $r$ , the current density was then computed from the well-known relation for an axially symmetric column:

$$J = \frac{1}{\mu} \left( \frac{\partial B}{\partial r} + \frac{B}{r} \right)$$

(b) Potential distribution

This measurement was carried out in the usual manner, using a small insulated tungsten wire probe swept rapidly across the column. This does not, of course, give accurate values of absolute plasma potential; however, it suffices for measuring the voltage gradient since the difference between the floating probe potential and the plasma potential, although not directly determinable in dense plasmas, does not vary significantly along the column. Hence potential differences between relatively closely spaced points along the column axis will accurately reflect the electric field. A typical result is shown in Figure 8.

(c) Temperature distribution

In contrast to the positive column of the FTA, the FCC column may be assumed to be in LTE. Hence the temperature can be obtained by the standard procedure (23) of measuring a chordal scan of intensity for the continuum radiation or for a line whose transition probability is known. The radial intensity distribution is then obtained by Abel inversion of the chordal scan, and the corresponding temperatures

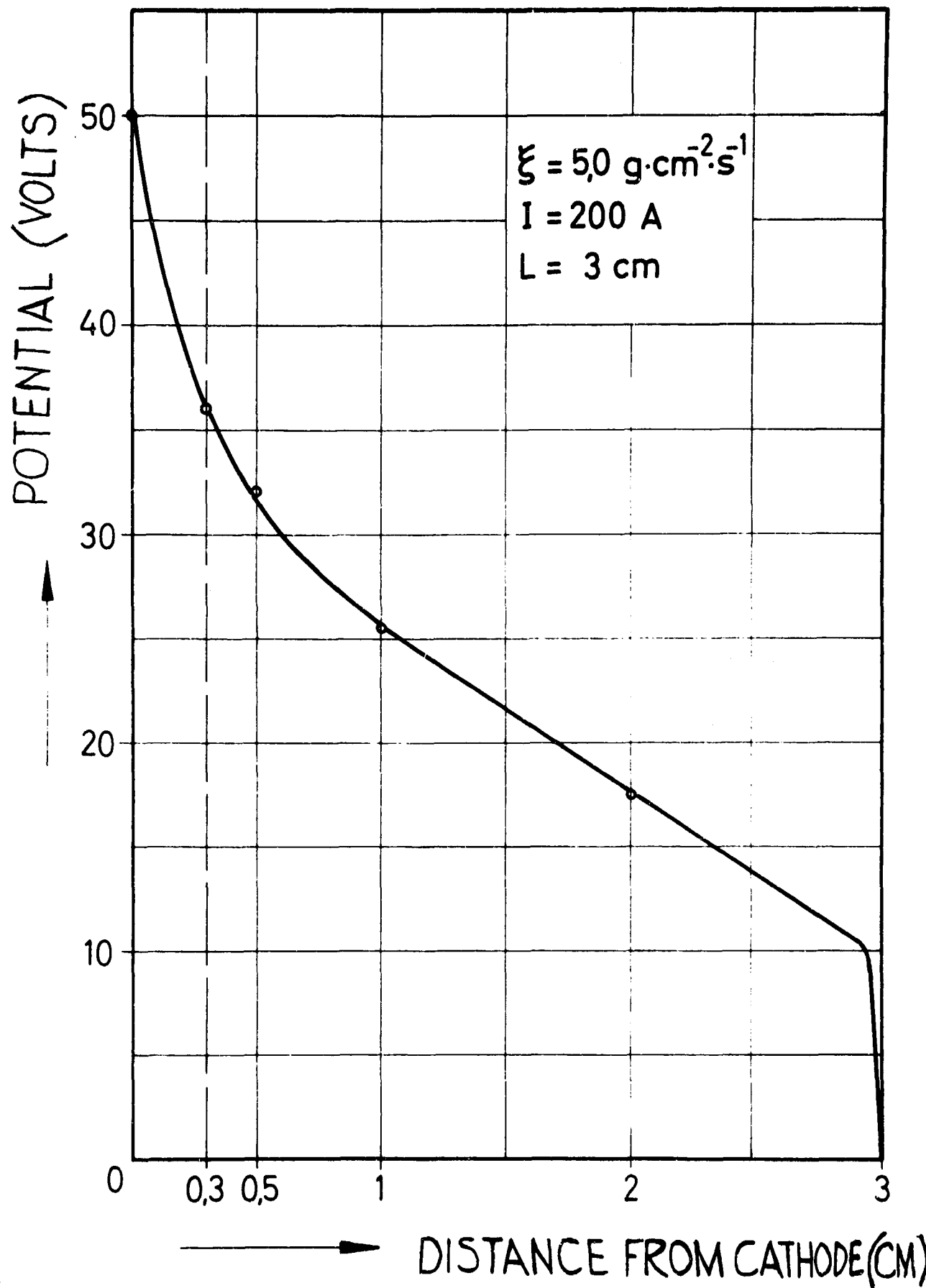


FIG. 8 AXIAL POTENTIAL DISTRIBUTION

from the known emission coefficients for either line or continuum radiation. Temperatures derived from both types of radiation agreed with each other within experimental error, thus justifying the assumption of LTE.

A typical radial temperature distribution at an axial station ( $z^*$ ) of 0.5 cm. from the cathode is shown in Figure 9. The pronounced effect of the mass flow density,  $\xi$ , on the temperature distribution is at once evident. In particular, the axial temperature rises sharply from 13,200°K at  $\xi = 2.5 \text{ gm/cm}^2\text{-sec}$  to 18,300°K at  $\xi = 5 \text{ gm/cm}^2\text{-sec}$ . Then as  $\xi$  is further increased the axial temperature drops again, reaching a value of 13,000°K at  $\xi = 20 \text{ gm/cm}^2\text{-sec}$ . It is significant that the potential gradient in the same axial region, and the total arc drop as well, follows the same variation with  $\xi$ , i.e. both quantities have a maximum at  $\xi = 5$ . (cf. Figure 8 with Figures 3.16 and 3.18 of ref. 3) It should be noted that the total convection rate ( $\dot{m}$ ) is the same for all 3 cases, so that the effect represents a maximum in the column enthalpy as well as temperature. The same effect has been observed at  $z^* = 1$  and 2 cm, so that it appears to pervade the entire column.

This interesting phenomenon is attributed to the constrictive effect of the radial component of injected gas momentum on the current density distribution near the column axis. The increase in current density near the axis increases the local rate of Joule heating thereby increasing the temperature and

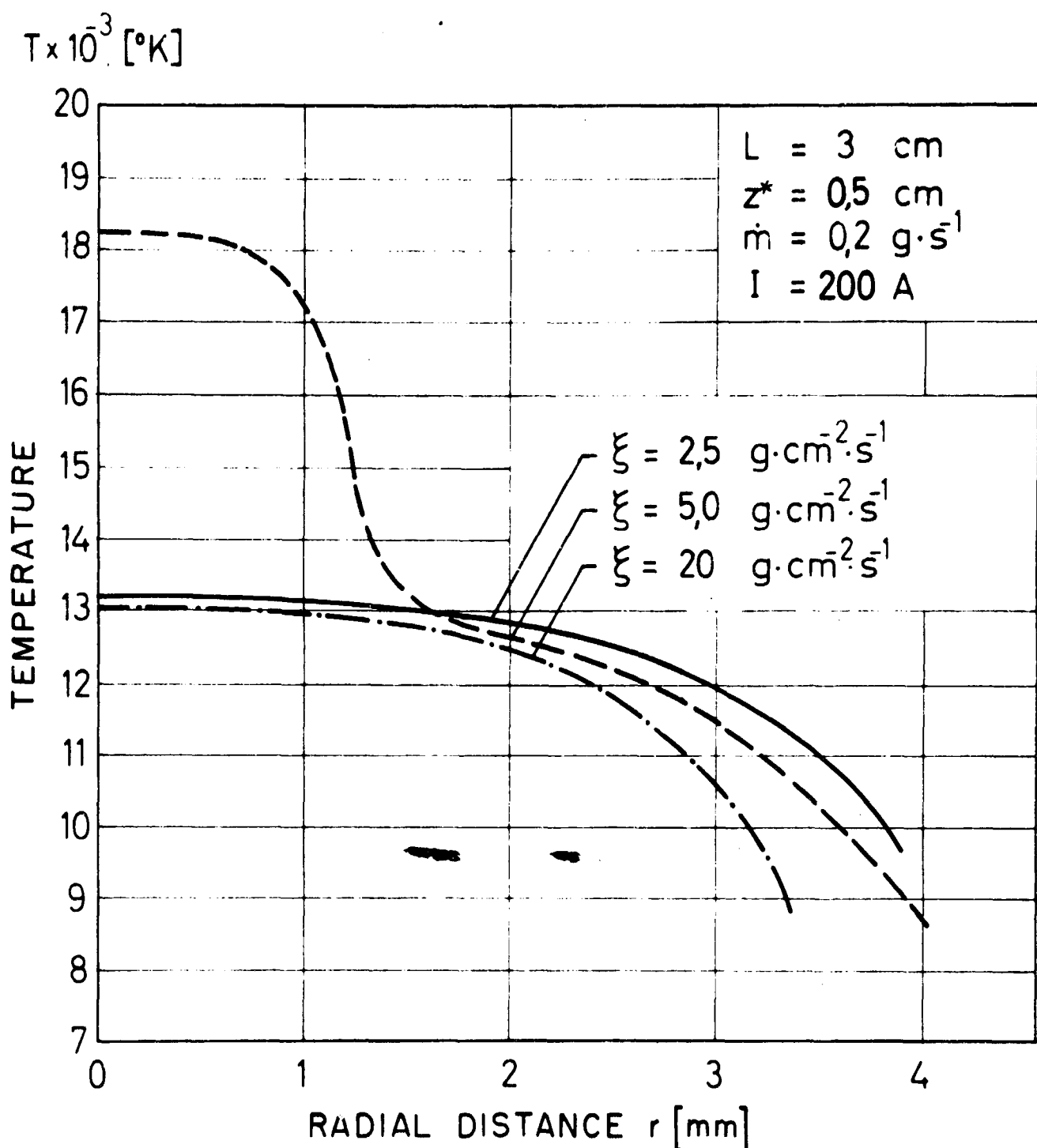


FIG. 9 RADIAL TEMPERATURE DISTRIBUTION AT  $z^* = 0.5 \text{ cm}$

enthalpy. As  $\xi$  is increased beyond 5, the flow undergoes a more or less gradual transition from essentially laminar flow to turbulent flow. The transition region appears to lie between  $\xi = 6$  and  $\xi = 9$ . (cf, Figure 3.19, ref. 3). As the nature of the flow changes an increasingly larger fraction of the flow momentum changes to angular momentum which of course reduces the linear radial component and therefore the degree of column constriction. The rise in temperature of an arc column due to (laminar) radial inflow was predicted theoretically by Druxes et al. (24)

In Figure 10, the complete temperature profile of the FCC column for  $\xi = 5$  is presented. The high column temperatures exhibited, while not quite as high as those obtainable by tight constriction with a water-cooled channel, is nevertheless of practical interest in view of the much higher efficiency of the device and the complete accessibility of the column.

#### (2) Determination of transport properties

The results of the diagnostics program were utilized to determine the electrical conductivity, the thermal conductivity and the dynamic viscosity of argon as a function of temperature. The analysis required to evaluate these parameters makes use of the "single fluid plasma model" to which the following conditions are assumed to hold over the major portion of the arc column .

- a. The shape of the column is right circular cylinder of length "L" and radius "R":\*

\* This excludes only the first few mm of the column beyond the cathode tip.

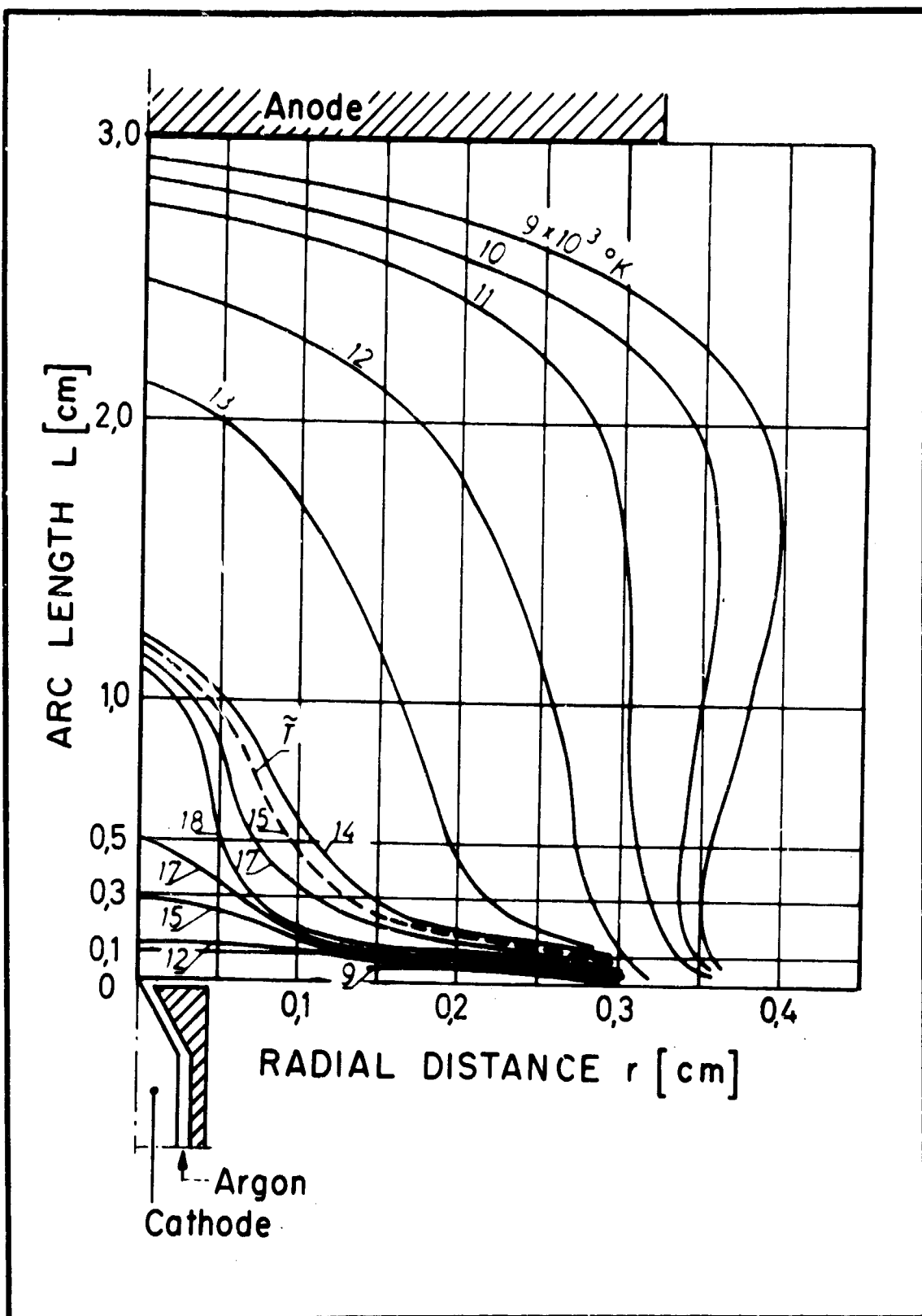


FIG. 10 TEMPERATURE PROFILE OF FCC

b. The gas flow is assumed one-dimensional laminar, and axisymmetric with the mass flux density  $\rho_w = \xi$  constant.

c. The arc is stationary.

d. The axial temperature gradient is small.

e. The existence of local thermodynamic equilibrium is assumed.

f. The self-magnetic field is negligible.

g. The electric potential is constant on planes perpendicular to the axis ( $E \cdot \nabla T = 0$ ).

h. Viscous dissipation and kinetic energy changes are assumed negligible compared to enthalpy changes due to ohmic heating.

i. The azimuthal and radial components of the velocity are zero.

j. The plasma is optically thin.

k. The pressure gradients in all directions are negligible.

(a) Electrical conductivity

With the above assumptions, the electrical conductivity may be computed directly from Ohm's law:

$$\sigma = \frac{J}{E}$$

The measurements of  $J$  and  $E$  were made by the probe methods described above for the indicated three values of  $\xi$ . The results for a large number of measurements, converted into temperature via the observed axial temperature distribution pertinent to each measurement, are presented in Figure 11.

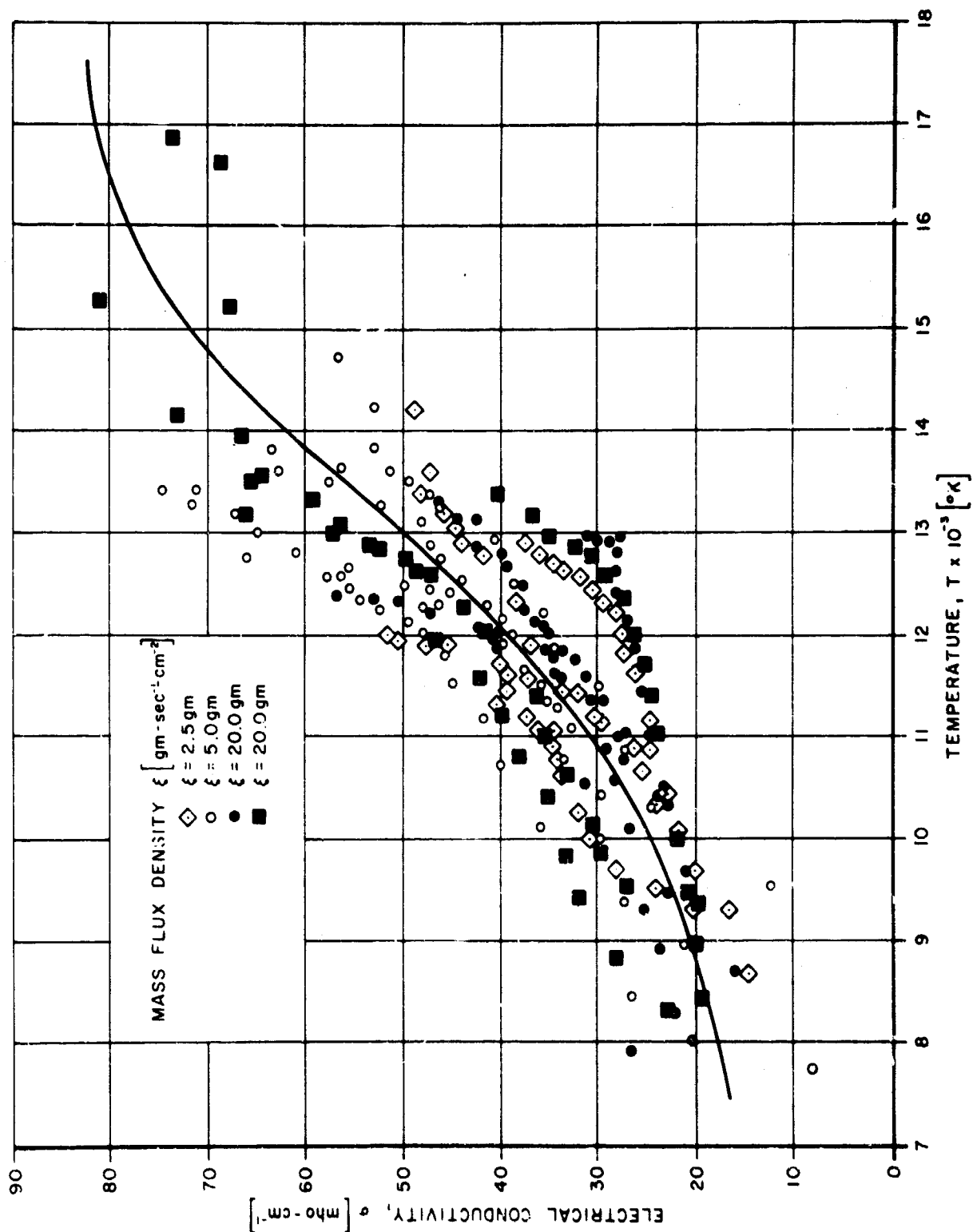


FIG. 11 EXPERIMENTAL DETERMINATION OF ELECTRICAL CONDUCTIVITY VS. TEMPERATURE (1 ATM. ARGON)

F-1/312

The average of all measurements is indicated by the solid line.

(b) Thermal conductivity

The basic relation for the determination of the thermal conductivity  $\lambda(T)$  is the Elenbaas-Heller equation, which is derived from the more general energy equation. For the assumed model, the energy equation can be separated from Maxwell's equations and the momentum equation. Applying the foregoing assumptions, the latter reduces to the familiar form of the Elenbaas-Heller equation

$$\sigma E^2 + \frac{1}{r} \frac{\partial}{\partial r} \left( r \lambda \frac{\partial T}{\partial r} \right) = S(r)$$

$S(r)$  being the radiation term. This relation equates the ohmic heating of the arc to the energy losses due to thermal conduction and radiation.

Integrating over the radius and solving for the thermal conductivity  $\lambda(r)$  yields the expression:

$$\lambda(r) = \frac{\int_r^R \sigma(r) E^2 r dr - \int_0^R S(r) dr}{r \frac{\partial T}{\partial r}}$$

It should be pointed out that in contrast to the lower temperature FTA column, the energy losses due to radiation in

the FCC are quite important and should be taken into account in the computation of the thermal conductivity. In the case of a free burning 200 ampere argon arc, ignoring the radiation loss would cause a 10 per cent error in the determination of thermal conductivity. The numerical calculations were carried out on an SDS Sigma 7 computer and the results are presented in Figure 12.

(c) Dynamic viscosity

In accordance with the assumed model for this study, and neglecting higher order terms, the momentum equation in cylindrical coordinates can be represented by the form:

$$\rho(r) w(r) \frac{\partial w}{\partial z} = \frac{1}{r} \left[ r \eta(r) \frac{\partial w}{\partial r} \right]$$

where  $\rho$  denotes the density,  $\eta$  the dynamic viscosity, and  $w$  is the axial flow velocity. Integrating over the radius and solving for the viscosity  $\eta$  at the radial coordinate  $r = r'$  gives the expression

$$\eta(r') = \frac{\int_0^{r'} \left[ \rho(r) r w(r) \frac{\partial w}{\partial z} \right] dr}{r' \frac{\partial w}{\partial r} \Big|_{r=r'}}$$

The density  $\rho(r)$  is obtained for the corresponding temperature distribution  $T(r)$  from the equation of state:

$$\rho(T) = m k T$$

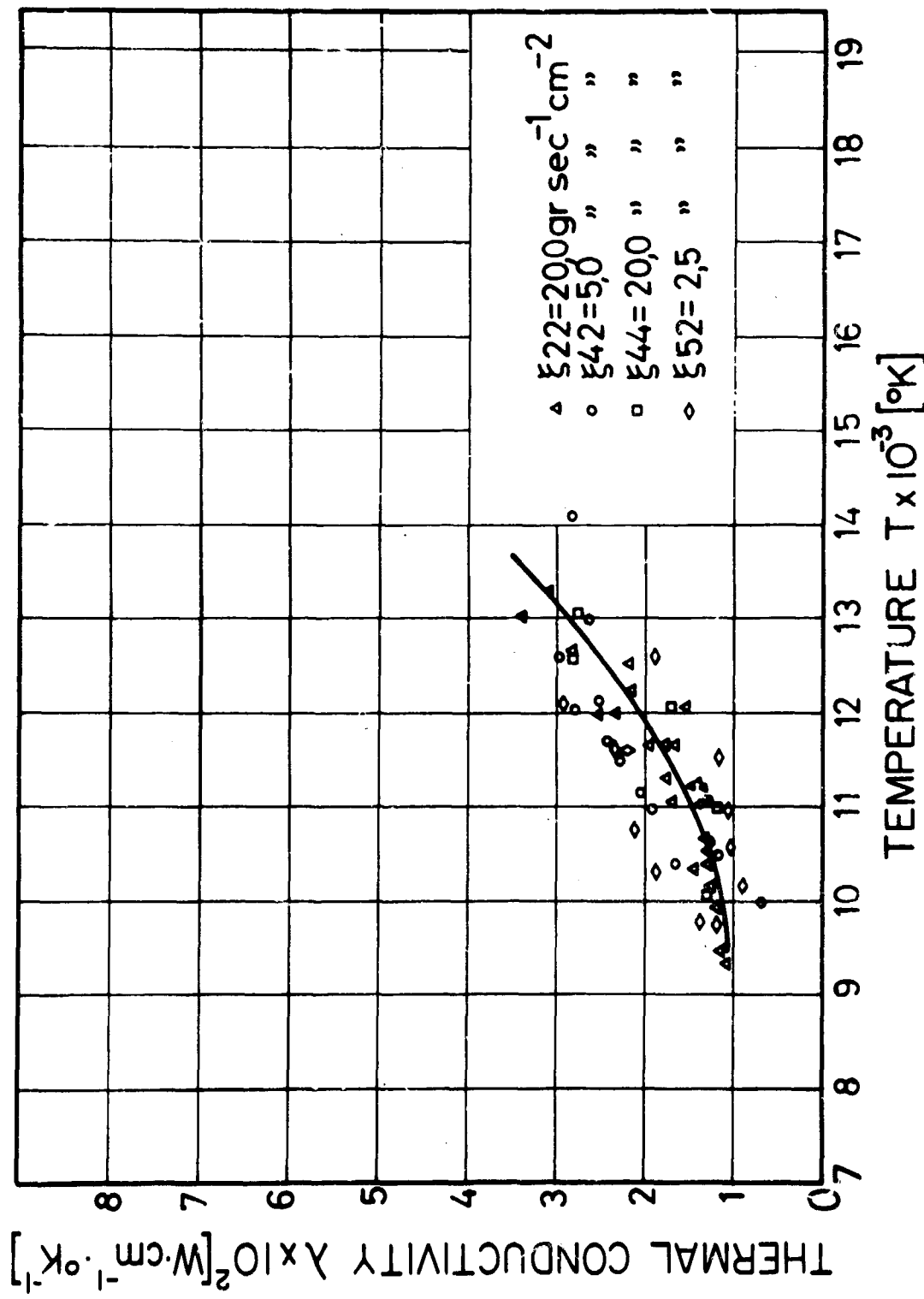


FIG. 12 MEASURED THERMAL CONDUCTIVITY VS. TEMPERATURE FOR ARGON AT ATMOSPHERIC PRESSURE

The velocity profile  $w(r)$  is determined by means of the Pitot tube probe mentioned earlier which is swept through the arc column by a fast acting pneumatic piston. The immersion time is in the order of  $1 \times 10^{-2}$  sec.

The experimentally obtained radial distribution of the dynamic pressure,  $p(r)$  is reduced to the radial distribution of the axial velocity  $w(r)$ , according to Bernoulli's equation for a Pitot tube. Although the cooling of the arc plasma by the probe effectively acts like a sink, the error is not very large. This follows from the analysis of Bernoulli's equation for compressible flow with the assumption that the mass flow density  $\rho_w$  remains constant along a streamline. Additionally, it should be pointed out, that it is necessary to determine only the axial gradient of the velocity and not its absolute value. Thus, measuring the values of the radial pressure distributions relative to each other at two closely spaced column cross sections, with the perturbation effects being essentially the same, it is reasonable to expect that the velocity gradient  $\frac{dw}{dz}$  can be accurately determined. The results of this measurement are shown in Figure 13.

Comparison of the curves shown in Figures 11, 12, and 13 with the results of about a dozen other investigators shows that our experimental averages (solid lines) fall about in the middle of the cluster of curves for these parameters. This indicates good agreement with the major portion of the reported

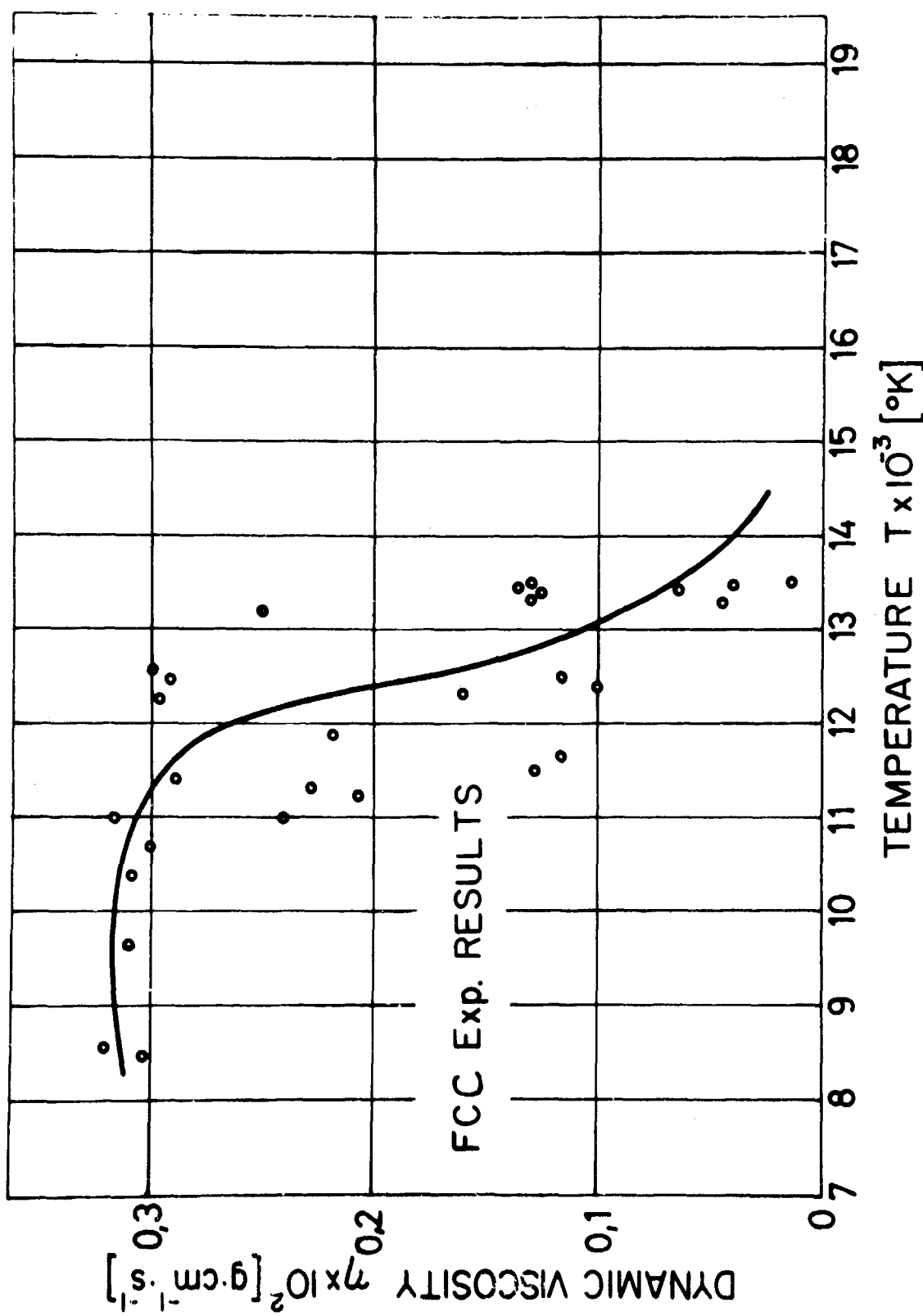


FIG. 13 MEASURED DYNAMIC VISCOSITY VS. TEMPERATURE FOR ARGON AT ATMOSPHERIC PRESSURE

measurements for these parameters. (See Figures 5.4, 5.7, and 5.11 of ref. 3).

### C. Techniques

The development of various techniques represented an important on-going objective which accounted for a significant portion of the effort during the entire contract period. This effort was directed toward improvements in four tributary areas, as follows:

1. Transient probe diagnostics
2. Arc configurations
3. Porous anode development
4. Arc ignition phenomena

Useful achievements have been accomplished in all four areas, particularly in probe diagnostics and the control of electrode damage due to arc ignition, which were directly responsible in a practical sense for the degree of progress achieved in the basic project objectives. A summary of the accomplishments in each category is given in the following.

#### (1) Transient probe diagnostics (Refs. 1,2,3,25)

During the first two years of this project work on transient probe diagnostic techniques was conducted under joint sponsorship of the Thermomechanics Laboratory of the Aerospace Research Labs., under Contract No. AF33(615)-3165. In all, four types of probes were developed:

- (a) A Hall magnetic probe for the measurement of the self magnetic field of the arc, which yields current

density.

(b) A thermocouple probe for the measurement of local absolute heat flux, which yields gas temperature.

(c) A fiber optics probe for the measurement of local radiant intensity, which yields temperature distributions directly.

(d) A Pitot tube probe for the measurement of local dynamic pressure, which yields the flowfield distribution.

The earliest results are presented in ref. 1, pp. 19-39. Further discussions are reported in ref. 2, pp. 108-149 (Hall, potential, and thermocouple probes) and in ref. 3, pp. 25-33, (Hall, fiber optics and Pitot tube probes). The most complete description for all four types of probes is contained in ref. 25. In addition two separate papers have been published on the Hall probe <sup>(26)</sup> and the fiber optics probe <sup>(27)</sup>. In view of these extensive previous reports only very brief summaries are included here.

(a) Hall magnetic probe

The use of a Hall effect sensor to measure the flux density of a magnetic field is well known. The major development in this work was the adaptation of newly available miniature sensing elements to a high speed transient probe system. The element best adapted to this purpose is the Siemens SBV 525 sensor, consisting of an indium arsenide Hall element measuring 1.5 x 2 x 0.3 mm. Estimated spatial resolu-

tion using this sensor is better than 1 mm. The two major problems encountered were thermal protection and perturbation of the column to be probed. To a considerable extent these represent trade-offs, since either thermal insulation or a water-cooled casing enlarges the probe tip and therefore the column distortion. Very fast traverse speed mitigates this problem since the response time of these elements is quite rapid and represents no limitation. Maximum probe speeds used in our work were  $\sim$  100 cm/sec. Higher probe speeds (which would involve a more elaborate drive mechanism) are of course possible, and would further alleviate the problem. At the speeds used no thermal damage after repeated probings was observed. The main concern was thermal variation of the Hall coefficient and development of a spurious thermoelectric potential.

For probing the FTA column in which the maximum temperature is  $< 12,000^{\circ}\text{K}$ , the problem was solved by a thin thermal insulation of fiberfrax. Experiments showed that, as the thermally insulated probe penetrated the first half of the column, both thermal influence on probe output and perturbation of the column were negligible (See ref. 25, Figs. 24 and 25, and ref. 26 for a discussion of probe perturbation). Hence only the first half of the oscillogram was used, which, because of cylindrical symmetry, was sufficient for the measurement.

The probe output was fed to a standard gaussmeter to ob-

tain  $B(r)$  vs.  $r$ . A typical oscillogram of the FTA column, and the resultant radial distributions of  $B(r)$  and  $J(r)$  are presented for illustration in Figures 14, 15, and 16 respectively.

In probing the FCC column, in which the maximum temperature exceeds  $12,000^{\circ}\text{K}$ , thermal insulation was found to be inadequate. Accordingly a water-cooled jacket was designed for the probe. This eliminated the problem of thermal effects but posed the problem of correcting for column perturbation owing to the larger size of the water-cooled probe. In addition to higher speed probing, the miniaturization of the water-cooled jacket, with associated high pressure water-cooling in the manner of the Greyrad enthalpy probe<sup>(28)</sup>, would appear to solve both the thermal and perturbation problems of the Hall probe, thus making this instrument available for use on almost any type of arc column.

(b) Thermocouple probe

The development of the transient thermocouple probe represents one of two attempts to obtain space-resolved radial distributions of temperature in free-burning arc columns and plasma jets. Elimination of the laborious Abel inversions required by spectrographic techniques was one of the chief motives for this work. For argon plasmas at 1 atm. whose temperature distribution lies in the range 3000 to  $12000^{\circ}\text{K}$ , the thermocouple probe ultimately evolved was highly successful, complete temperature profiles being pro-

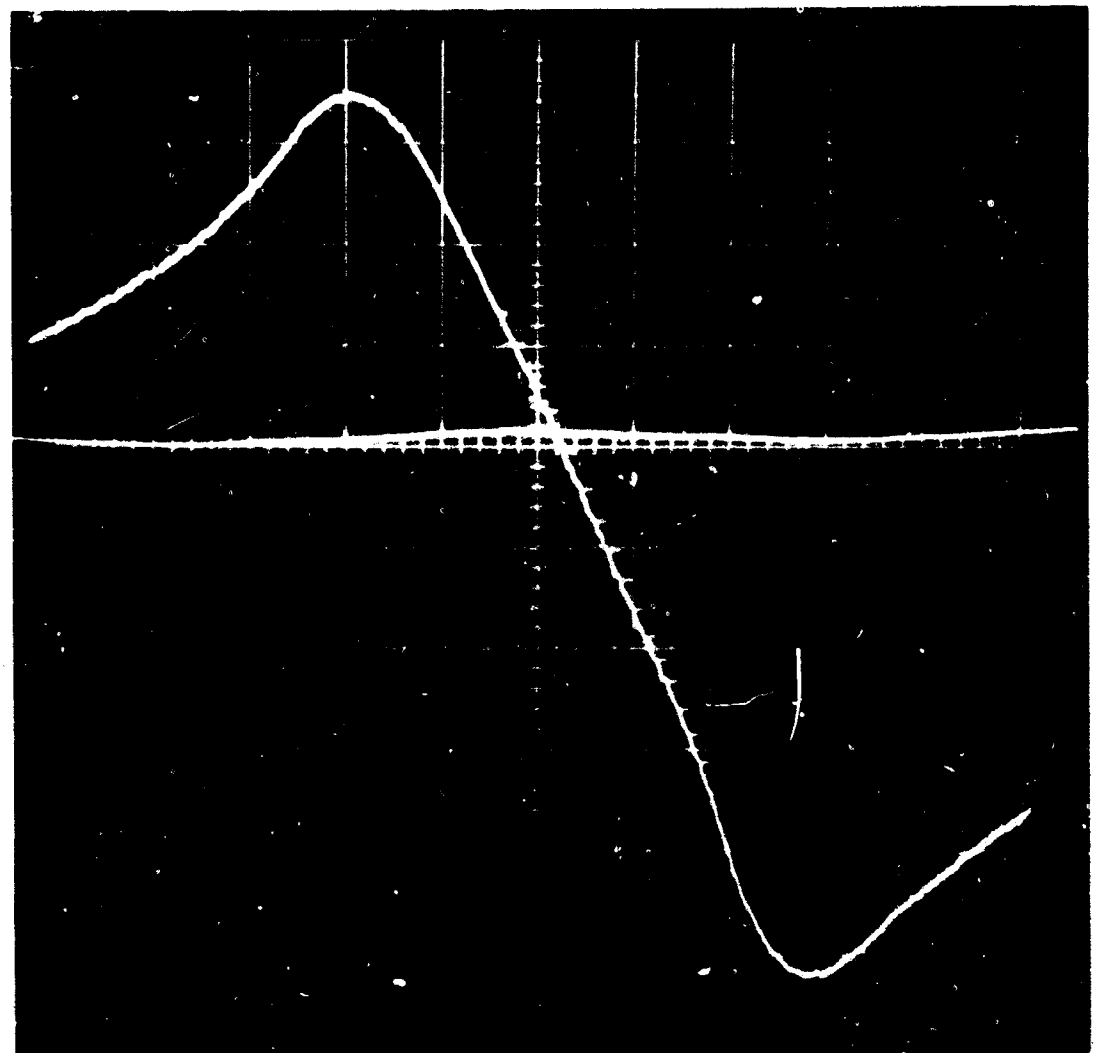
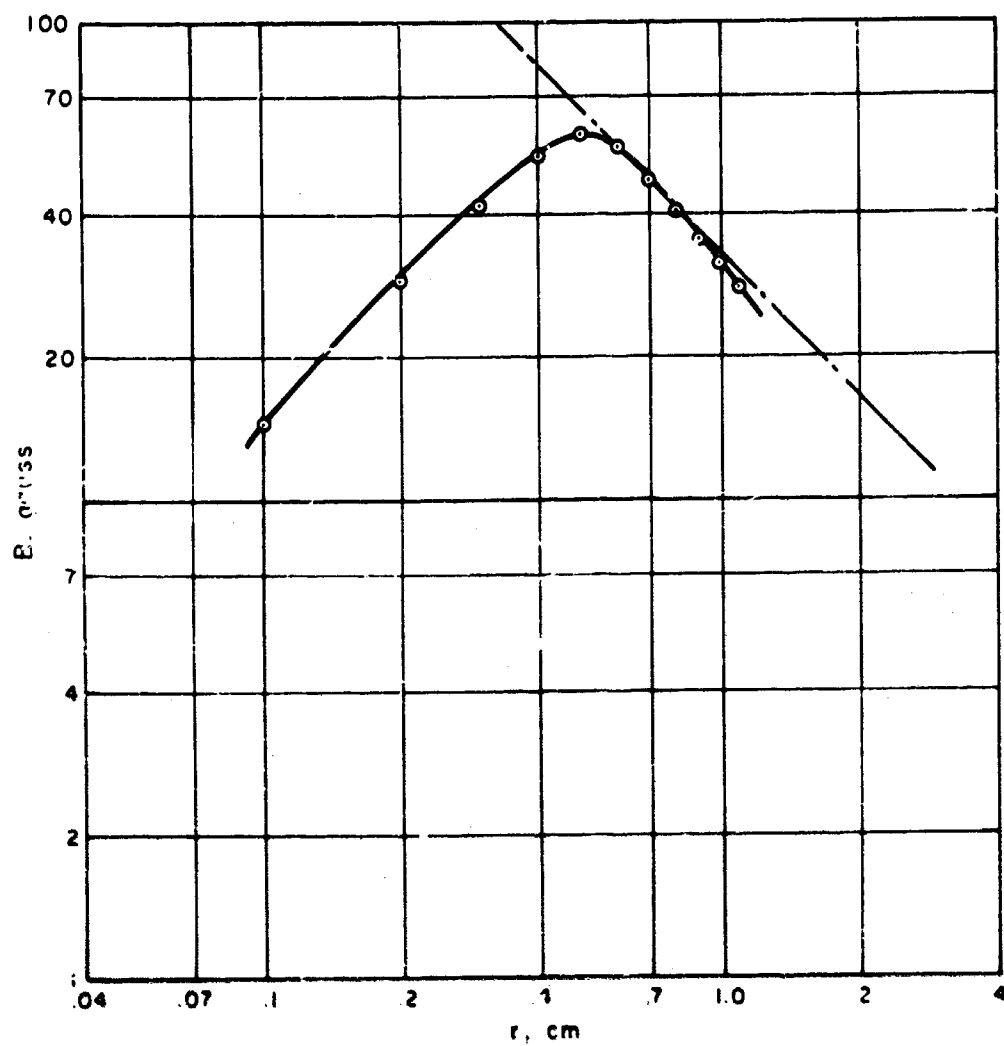


FIG. 14 OSCILLOGRAM OF HALL PROBE TRACE 1.5 MM FROM FTA  
ANODE; 150 AMP. ARGON ARC



A-334-5-0016

FIG. 15 RADIAL MAGNETIC FIELD DISTRIBUTION 1.5 MM FROM PTA ANODE ( FROM TRACE OF FIG. 14 )

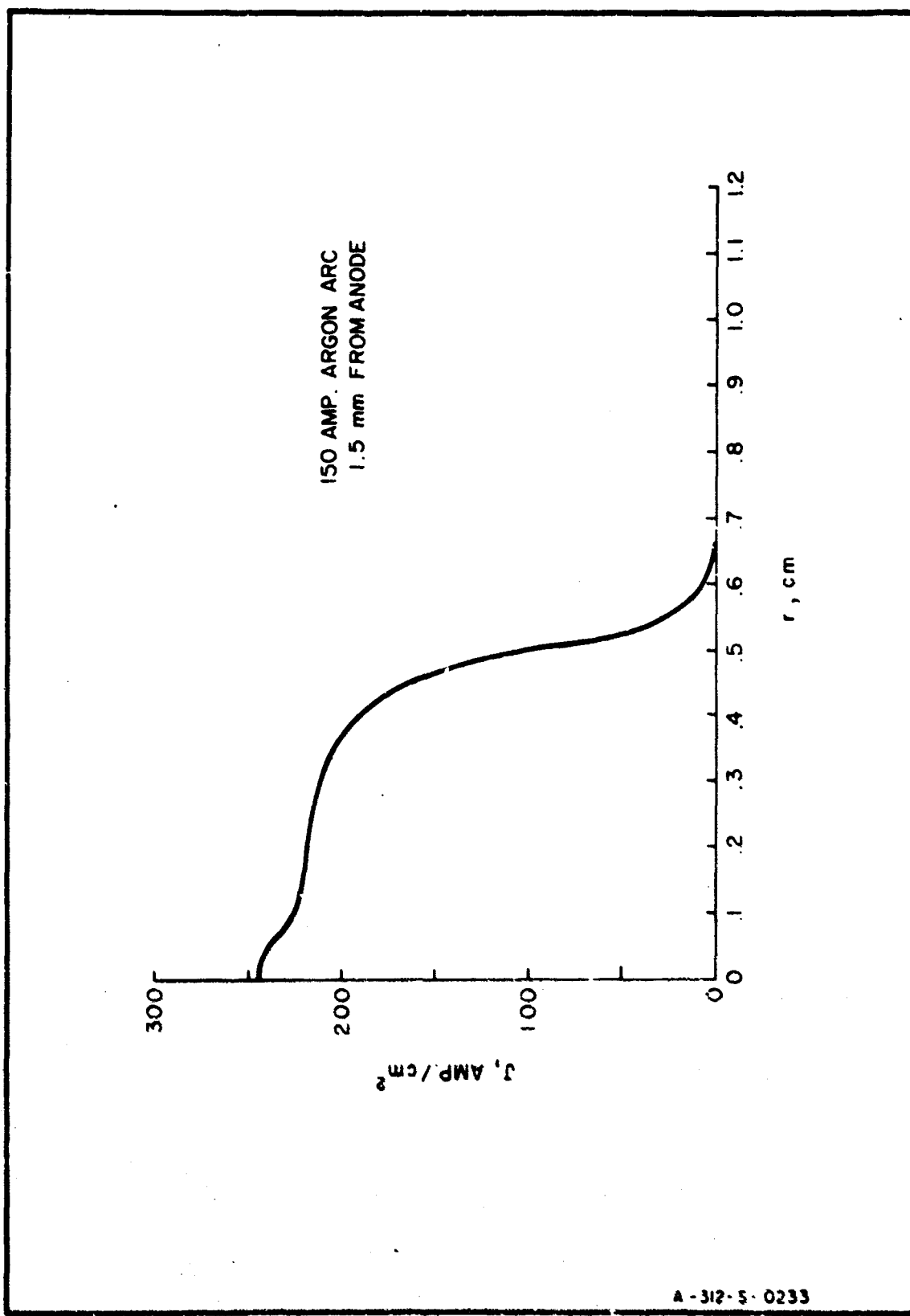


FIG. 16 RADIAL CURRENT DENSITY DISTRIBUTION 1.5 MM FROM FTA  
ANODE (FROM FIG. 15)

duced within minutes after the plasma was probed.

Prior attempts to use miniature thermocouples to probe plasmas were all based on a differential measurement, i.e. a comparison of probe output for two closely-separated points in space or time, the rationale being the cancellation of the film transfer coefficient from the data reduction. Traditionally this has been a very difficult parameter to evaluate under the conditions of measurement. An analysis<sup>(29)</sup> performed early in the program revealed that, as a general feature, all probe systems based on measuring heat flux ratios are limited in their range to approximately twice the maximum probe temperature (melting point of the thermocouple), which effectively precludes measurement above about 4000°K. Accordingly the effort was devoted to producing a probe based on absolute heat flux measurement. Neglecting radiation and other minor heat losses, the governing equation is

$$T_g = \left( \frac{C_{pr} m_p}{h A_p} \right) \frac{dT_p}{dt} + T_p \quad (23)$$

where  $T_{g,p}$  = gas and probe temperatures, respectively

$C_{pr}$  = heat capacity of probe tip

$m_p$  = mass of probe tip

$A_p$  = surface area of probe tip

$h$  = film coefficient

$T_p$  and  $\dot{T}_p$  are measured directly from the probe output.

$A_p$ ,  $C_p$  and  $m_p$  are known from the probe size and composition.

Therefore direct readout in terms of temperature requires a knowledge of  $h$ , as mentioned above, which is itself temperature dependent. The problem was attacked by making use of an empirical correlation relating the Nusselt number to the Reynolds and Prantl numbers for a small sphere <sup>(30)</sup>, viz:

$$Nu = 2 + 0.35(Re)^{0.58} (Pr)^{0.36} + 0.03(Re)^{0.54} (Pr)^{0.33} \quad (24)$$

where  $Nu$ ,  $Re$ ,  $Pr$  = Nusselt, Reynolds, and Prantl numbers, respectively.

Eq. 24 provides a relation between  $h$  and the transport properties of the medium in the boundary layer. For subsonic flow ( $Re \sim 0.1$ ) the arithmetic mean of free stream and probe temperatures is adequate for evaluation of the film temperature,

$$T_f = \frac{T_g + T_p}{2} \quad (25)$$

Eq. 25 permits a calculation of  $h$  for any pair of values of  $T_g$  and  $T_p$ , using published, theoretically derived data for the transport properties as functions of temperature, the latter being contained in definitions of  $Nu$ ,  $Re$  and  $Pr$ , viz:

$$Nu \equiv h\ell/\lambda$$

$$Re \equiv \xi\ell/\mu$$

$$Pr \equiv C_p\mu/\lambda$$

where  $\ell$  = diameter of (spherical) probe tip

$\lambda$  = thermal conductivity of gas

$\mu$  = viscosity of gas

$C_p$  = specific heat of gas at constant pressure

$\xi$  = mass flow density of gas

Converting  $T_p$  and  $\dot{T}_p$  into the probe output and slope,  $V$  and  $\dot{V}$ , via the known thermocouple vs. output curve, a set of calibration curves was constructed for the probe by plotting  $V$  vs.  $\dot{V}$ , parametric in  $T_g$  using a fixed value of  $\xi$  for each set, and evaluating  $h$  for the appropriate  $T_f$  with the aid of the published data on  $\lambda$ ,  $\mu$ , and  $C_p$ . A typical set of curves shown in Figure 17.

In actual measurement, the probe tip is swept through the arc at a rate such that the peak temperature of the probe does not exceed about  $600^{\circ}\text{C}$ . For a  $12000^{\circ}\text{K}$  column this represents a speed of 6 cm/sec. Hence for the material used (Pt-Pt/10% Rh) thermal damage is non-existent. Also at this speed the probe moves only 0.14 mm in a time equal to the thermal response time of the tip (2 m-sec.). Hence, since the tip is only 0.86 mm in diameter, excellent spatial resolution is obtained, and column perturbation is quite negligible. One of the most serious problems, namely the large random signal due to plasma fluctuations which appear in the output whenever the bare probe tip contacts the plasma, was solved by using a three-wire thermocouple system in place of the usual two-wire system. This consisted of two Pt wires and one of Pt/10% Rh. The outputs of the two similar wires and the two dissimilar wires were fed to

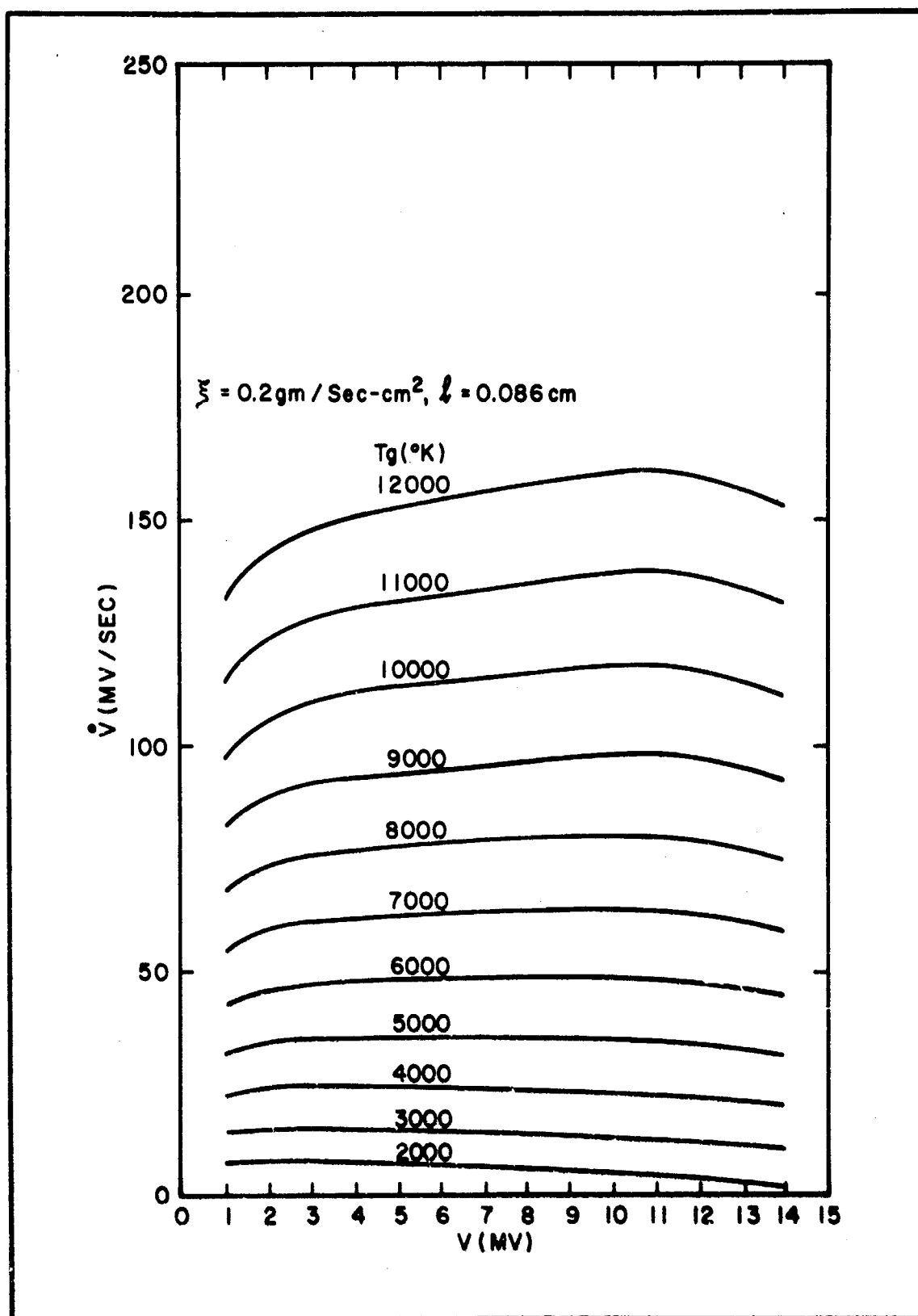


FIG. 17 CALIBRATION CURVE FOR Pt, Pt-10% Rh THERMOCOUPLE PROBE IN ARGON

opposite ends of a differential amplifier with a high common mode rejection ratio. Since the noise signal appears in the same amplitude and phase at both ends it is cancelled completely in the output. However the desired thermoelectric signal appears only at the input for the dissimilar wires and is therefore passed through without attenuation. A common mode rejection ratio of 120 db was successful in eliminating all trace of a 100 volt noise signal from a thermocouple output of only 100 microvolts.

The probe output and its slope are fed to the two inputs of a dual trace oscilloscope whose sweep is synchronized with the probe traverse. The oscillogram is indexed by superimposing markers (dots) on the trace to provide a measure of the radial coordinate. This provides a pair of values for  $V$  and  $\dot{V}$  for each value of radial coordinate, which is obtainable from the oscillogram within a few minutes. A group of such oscillograms is illustrated in Figure 18. These represent probings of the plasma jet of a conventional plasma torch. The temperature distributions were obtained directly from the calibration curves (Figure 17) for the appropriate value of  $\xi$ . The resulting temperature profile is shown in Figure 19. The curve of  $T_g$  shown in Figure 2 was also obtained by this method.

Because of the inclusion of  $\xi$  in the Reynolds number in eq. 24, the question arises as to the implied necessity for an auxiliary measurement of  $\xi$  for the selection of the appropriate

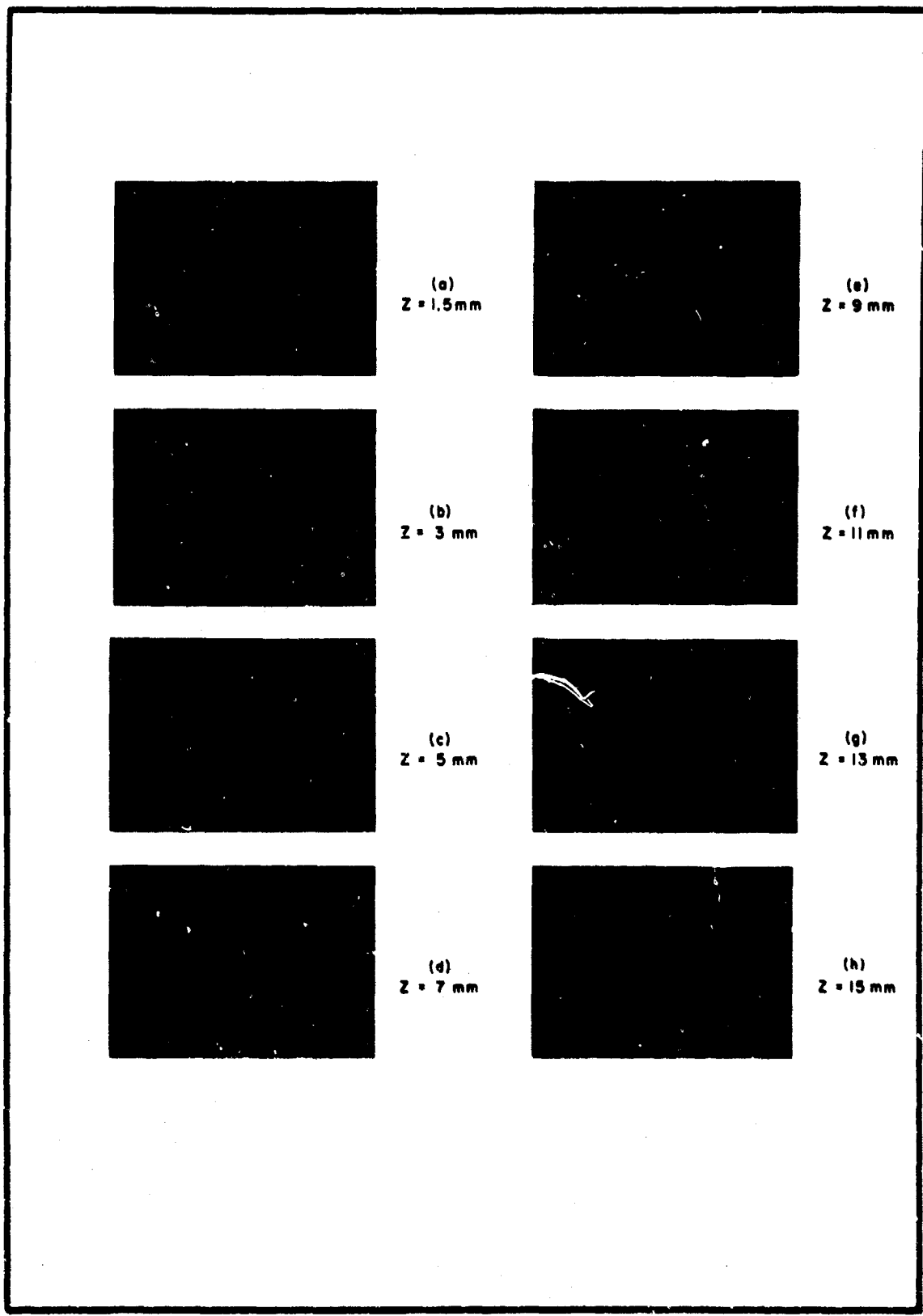


FIG. 18 OSCILLOGRAMS OF THERMOCOUPLE PROBE OUTPUTS FOR AN ARGON PLASMAJET

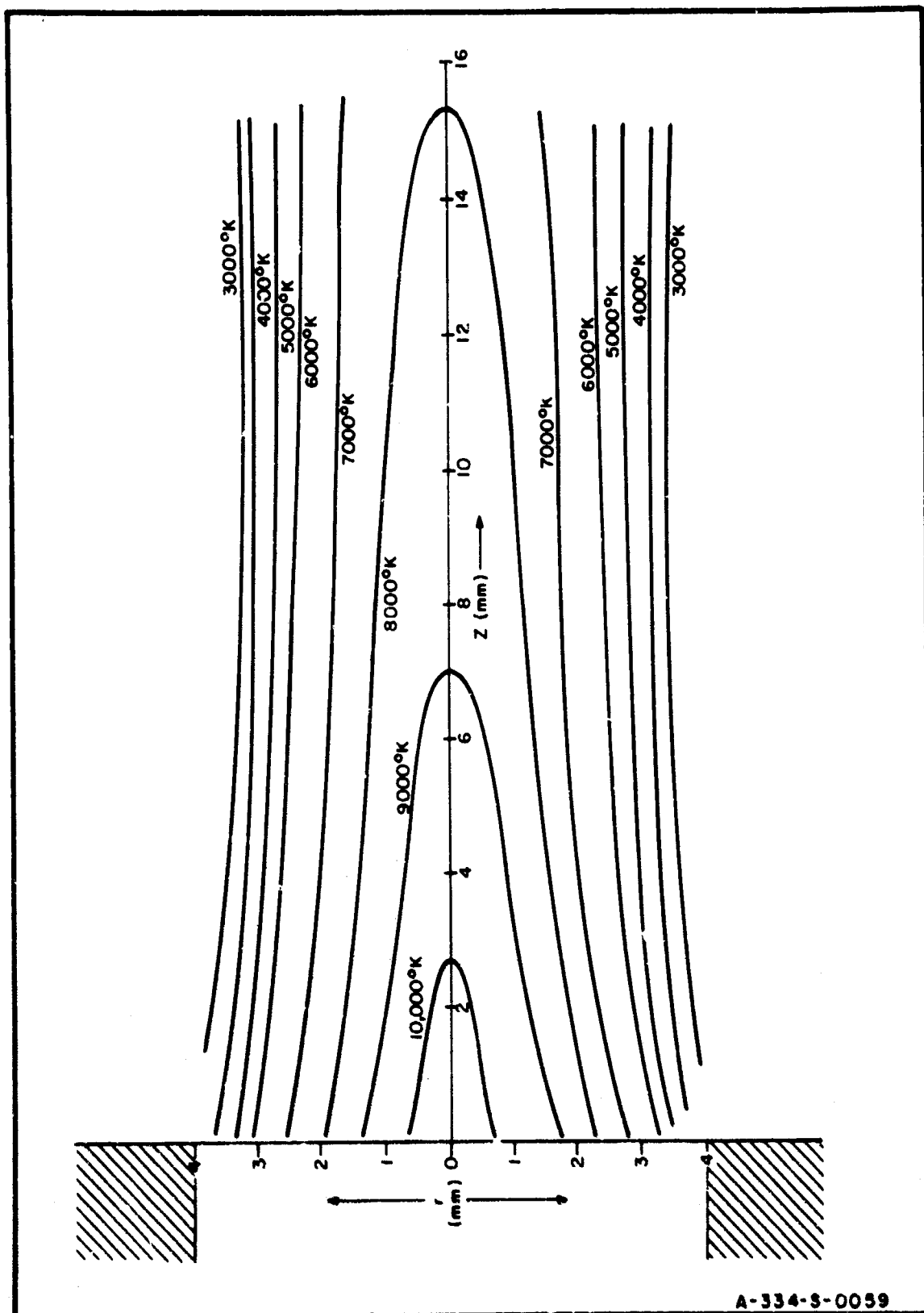


FIG. 19 TEMPERATURE PROFILE OF ARGON PLASMAJET MEASURED BY THERMOCOUPLE PROBE (SEE FIG. 18)

set of calibration curves. The discussion in ref. 25 shows that the error in  $T_g$  due to uncertainty in  $\xi$  is only 10% of the error in  $\xi$ . Hence a crude estimate of  $\xi$  for a given system is adequate, such as derived from the total mass flow and the column cross-section.

Validation of the thermocouple probe by comparative measurements with the Greyrad enthalpy probe and spectrographic measurements, performed simultaneously with the thermocouple probe, showed agreement to within less than 5%. For gas temperatures under 9000°K the data may be used directly. For temperatures between 9000 and 12000°K, a correction must be applied (amounting to about 10% at 12000°K) owing to the sharp rise in the thermal conductivity of argon above 9000°K, which makes the simple arithmetic mean(eq. 25) inadequate to represent the film temperature. A procedure for applying this correction is described in Appendix III of ref. 25.

(c) Fiber Optics probe

The fiber optics probe work represents an attempt to sample plasma radiation from a small (e.g. 1 mm<sup>3</sup>) plasma volume in order to achieve directly space-resolved distributions of the emitted radiation. Such a probe would be useful in deriving temperature distributions from the observed radial intensity distributions and, by analyzing the radiation spectrometrically, provide information on the distribution of species. The highly localized sampled volume of this probe eliminates the need for Abel inversion of the data as well as

the requirement for cylindrical symmetry. Preliminary discussion is presented in ref. 1, pp. 34-39, ref. 25, pp. 51-66, and in ref. 27.

The first probe tested consists essentially of a slender, stainless steel tube with a blackened interior which traverses the plasma at right angles to the plasma flow. The front end of the tube is fitted with an end cap such that a small (1 mm diam.) hole pierces the tube near the end to admit a small stream of plasma as the probe traverses the column. At the far end of the tube a flexible fiber optics bundle is inserted so as to receive the light flux only from the small plasma volume flowing through the hole. This geometry is illustrated in Figure 20.

The radiation is conducted along the fiber optics bundle, which was about 20 inches long, to emerge on the photocathode of a photomultiplier tube, the output being then recorded oscillographically in the usual manner.

In this model the probe is inserted along its axis so that the tube remains immersed in the hot plasma during the entire traverse period. As a result difficulty was experienced with overheating. Although the traverse speed was high enough to avoid thermal damage, the blackened interior to the tube became hot enough to emit radiation some of which entered the fiber optics bundle and led to spurious results. This difficulty was eliminated in a later design illustrated in Figure 21. In this model the tube is open-ended and the cap is replaced by a

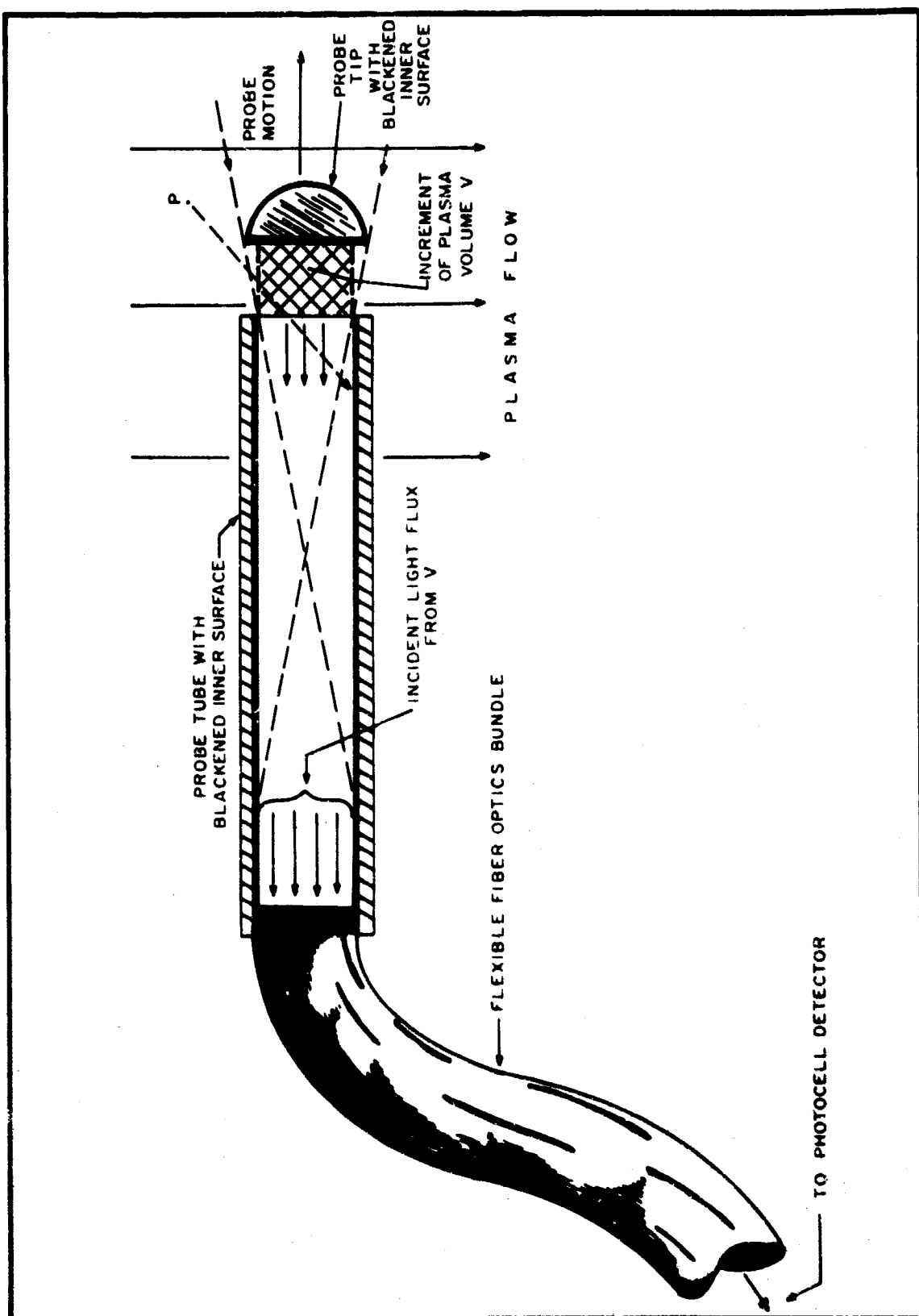
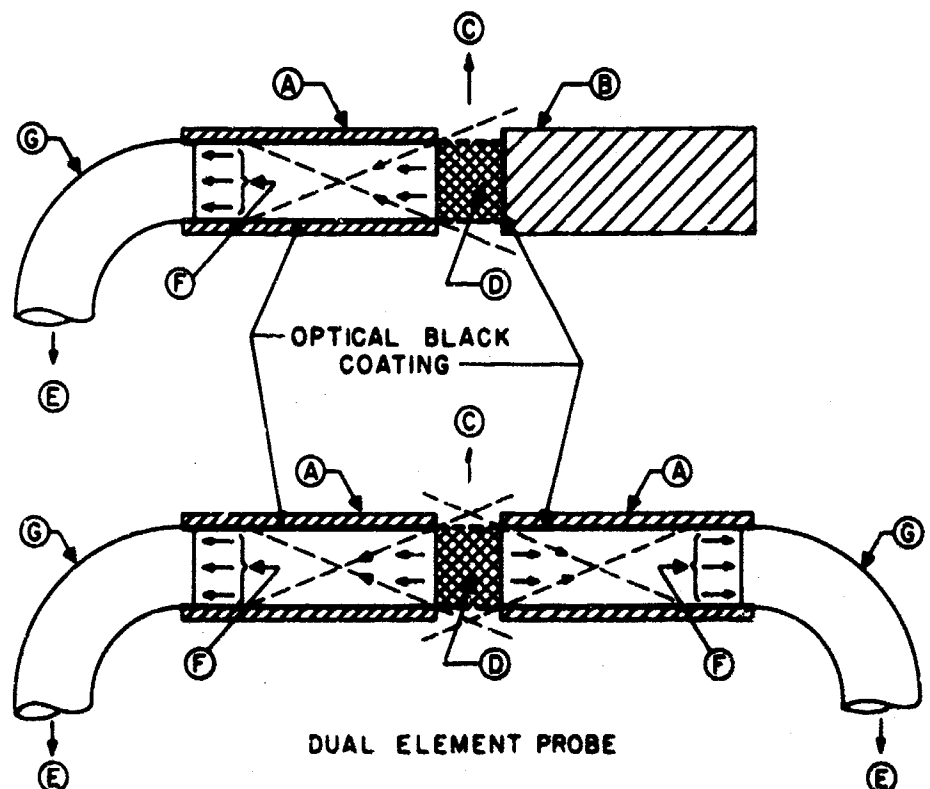


FIG. 20 FIRST MODEL OF TRANSIENT FIBER OPTICS PROBE

SINGLE ELEMENT PROBE



LEGEND:

- A. PROBE TUBE WITH BLACKENED INNER SURFACE
- B. PROBE CAP WITH BLACKENED FRONT SURFACE
- C. PROBE MOTION
- D. INCREMENT OF PLASMA VOLUME V
- E. TO PHOTOMULTIPLIER AND RECORDER
- F. INCIDENT LIGHT FLUX FROM V
- G. FLEXIBLE FIBER OPTICS BUNDLE

FIG. 21 TWO LATER MODELS OF TRANSIENT FIBER OPTICS PROBE

solid rod with a blackened end (top diagram of Figure 21) having the same diameter as the tube. This effectively blocks off all radiation from the plasma except that from the small volume between the ends of the tube and rod. The latter are mounted on a rigid yoke and driven through the plasma in a direction at right angles to both the arc column and the axis of the tube. Hence the probe is immersed in plasma only for a very short fraction of the traverse time. By replacing the solid rod with a second tube, also fitted with a fiber optics bundle, (bottom diagram of Figure 21) the probe output is doubled. This dual element probe was used repeatedly with no visible thermal damage (at probe speeds of  $\sim$  100 cms/sec.) and with negligible spurious radiation. A typical trace of the distribution of radiant intensity across the FTA positive column is shown in Figure 22.

Tests performed with the dual element probe in comparison with simultaneous spectrographic measurements showed general good agreement between the two methods. Discrepancies were between 5% and 10% with the fiber optics probe being somewhat higher off-axis and somewhat lower near the axis. Some of the uncertainties considered involved the influence of noise level in the low luminosity regions off-axis, the influence of natural plasma fluctuations, and the uncertainty in the magnitude of the sampled volume. In the latter case, the sampled volume probably depends on the nature of the wake created in the plasma by the motion of the probe. This in

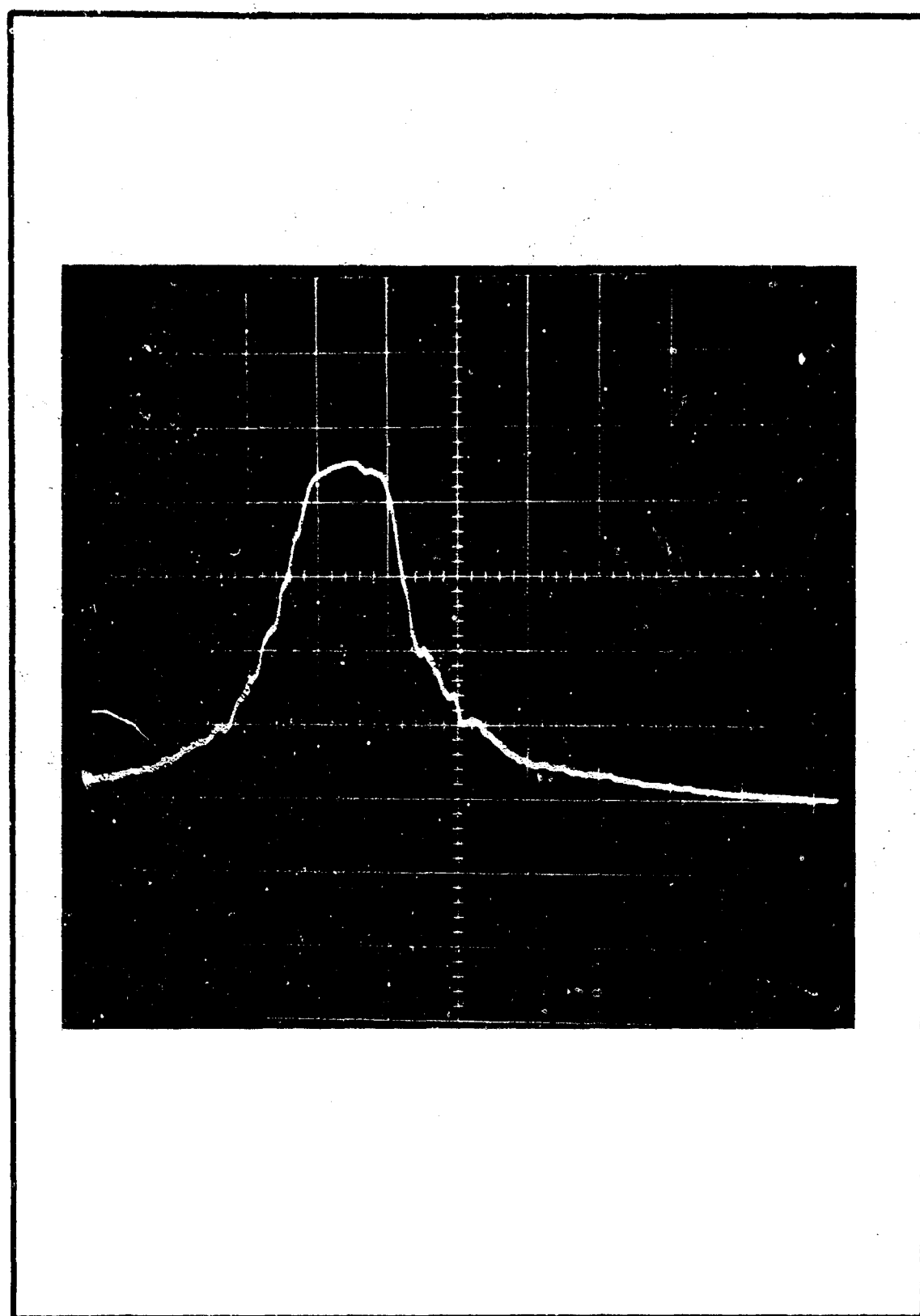


FIG. 22 OSCILLOGRAM OF RADIAL RADIANT INTENSITY DISTRIBUTION  
FOR FTA POSITIVE COLUMN (ARGON)

turn depends on the local relative velocity and some of the plasma transport properties. Complete analysis of these uncertainties was not carried out on this project. The results obtained, however, indicate that they are capable of resolution and that the fiber optics probe can be used effectively in measurement of radiant intensity distributions of free-burning arc columns.

(d) Dynamic pressure probe

The dynamic pressure probe was developed to obtain direct flow field distributions in free-burning arc columns and plasma jets. The probe involved in this work follows the design of Barkan and Whitman <sup>(31)</sup>. It consists of a small Pitot tube whose orifice is swept through the column. The Pitot tube is connected to a pressure transducer which produces a signal proportional to the local dynamic pressure. The mass flow density is then derived from the dynamic pressure with the aid of the Bernoulli equation in the usual manner. The chief motivation for this work was to investigate the influence of the mass flow density on the reduction of thermocouple probe data and to provide data required in the measurement of transport properties with the FCC.

The unit described by Barkan and Whitman involved a piezoelectric type of pressure transducer with a sensitivity  $\sim 0.5$  psi. This was tested in our systems and found to be wholly inadequate, the tests indicating that the sensitivity

requirement was two orders of magnitude higher. The major portion of the effort was expended in testing various available transducers. A satisfactory unit with the required high sensitivity was finally obtained, namely the Pace-Wianco model P105D variable reluctance transducer. This unit showed a sensitivity of  $< 0.001$  psi and was much more insensitive to mechanical shock and vibration than any of the piezoelectric types investigated. Its application is limited to low velocity flows such as the FTA, FCC, and similar devices, since the maximum pressure readable with this transducer is only 0.05 psi.

One of the important parameters for the Pitot tube probe is response time. This was investigated experimentally by probing a jet of nitrogen issuing from a 3/8" ID pipe. Steady state (stationary) measurements of the flow field were made as well as continuous traverses at different speeds. The results are shown in Figure 23, from which it is seen that at traverse speeds  $\leq \sim 25$  cms/sec, the transient response of the system is satisfactory. Either stainless steel or fused quartz Pitot tubes, when driven at 25 cm/sec speed, can be used without noticeable thermal damage. A group of oscillograms taken with the dynamic pressure probe and used to evaluate the flow field distribution of the FCC is presented for illustration in Figure 24.

#### (2) Arc Configurations

A number of arc configurations were investigated

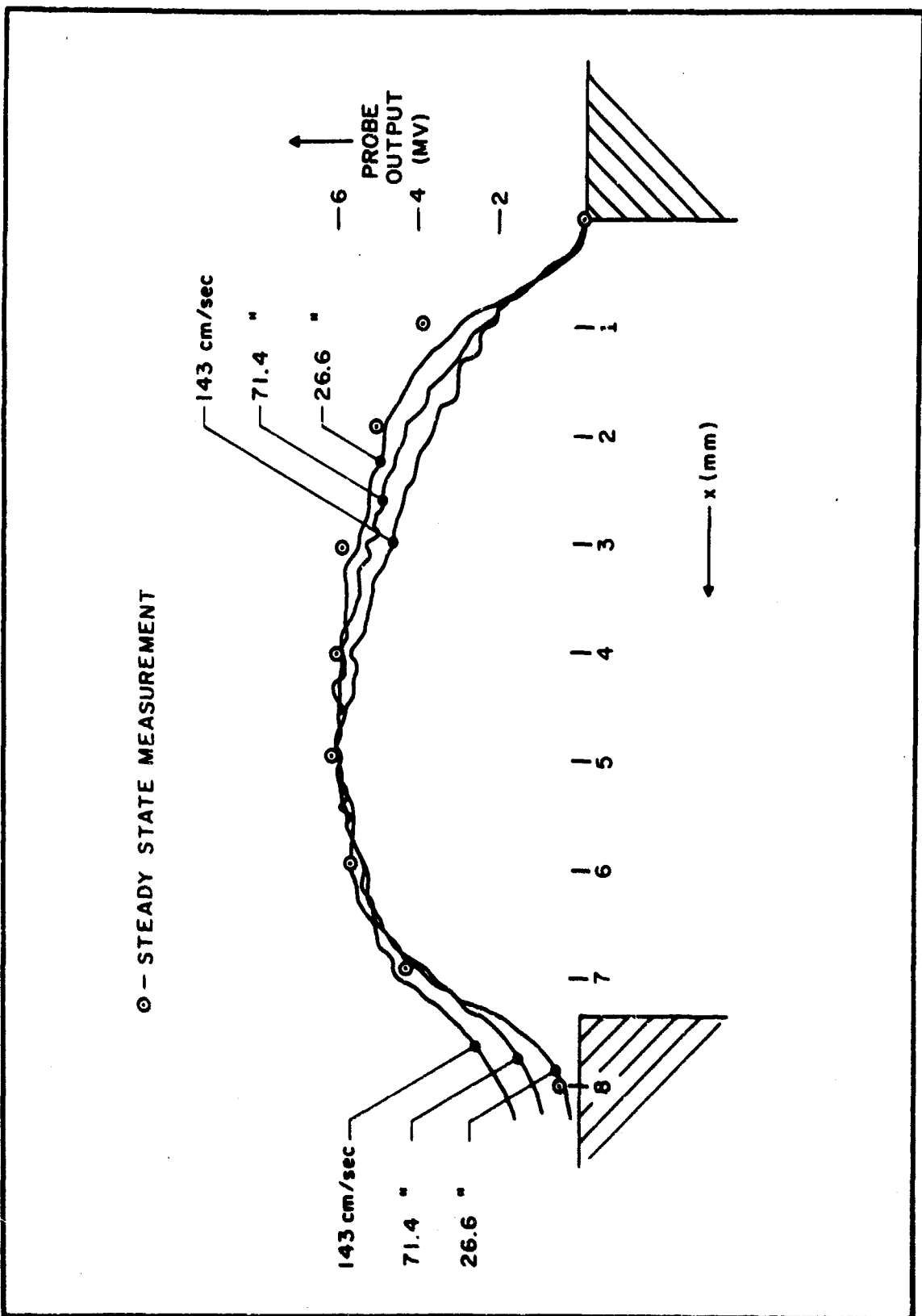
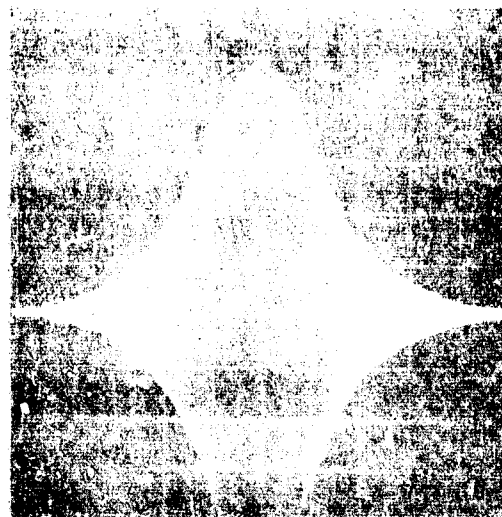
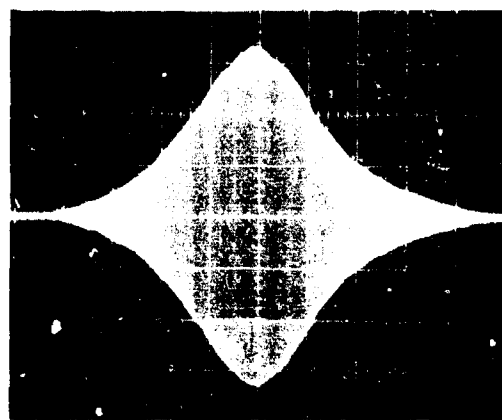


FIG. 23 COMPARISON OF TRANSIENT AND STEADY STATE  
PRESSURE PROBE MEASUREMENTS

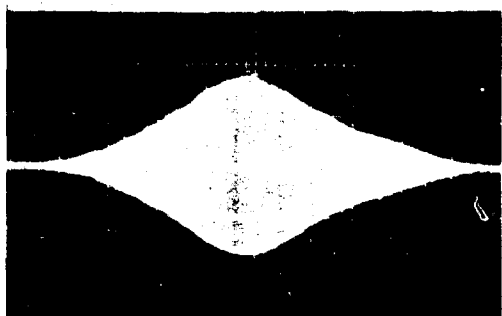
DIAMETRAL



1 mm OFF AXIS



2 mm OFF AXIS



3 mm OFF AXIS



FIG. 24 OSCILLOGRAMS OF PRESSURE PROBE TRACES  
IN CATHODE COLUMN AT  $z = 2$  CM AND  
VARIOUS LATERAL POSITIONS (ARGON, 1 ATM)

60H-334-0047

during the course of this project for the purpose of providing stable, quietly operating devices of high reliability and reproducibility while retaining the maximum of accessibility for probing the column and for several special purposes. The configurations which were successfully operated consist of the following:

- (a) Triple cathode cylindrical FTA
- (b) FTA/FCC combination with inclined geometry
- (c) Conical FTA
- (d) FTA/FCC combination with opposed geometry.

The range of usefulness for each of these configurations is discussed in the following.

(a) Triple Cathode Cylindrical FTA (ref. 1)

In the work on the FTA prior to the inception of this project a disc-shaped porous anode was used together with a bare tungsten rod cathode inclined at about 45° to the anode axis. This produced a cylindrical positive column suitable for diagnostics close to the anode. However a rather large turbulent mixing zone occurred due to the collision of the natural cathode jet with the anode gas which distorted the column beyond a cm or so from the anode when operating in the customary 5 to 15 KW power input range. Accordingly a triple cathode configuration was devised and tested, which was capable of swinging the three cathodes backwards so that the three cathode jets would merge smoothly with the positive column. The three cathodes were disposed

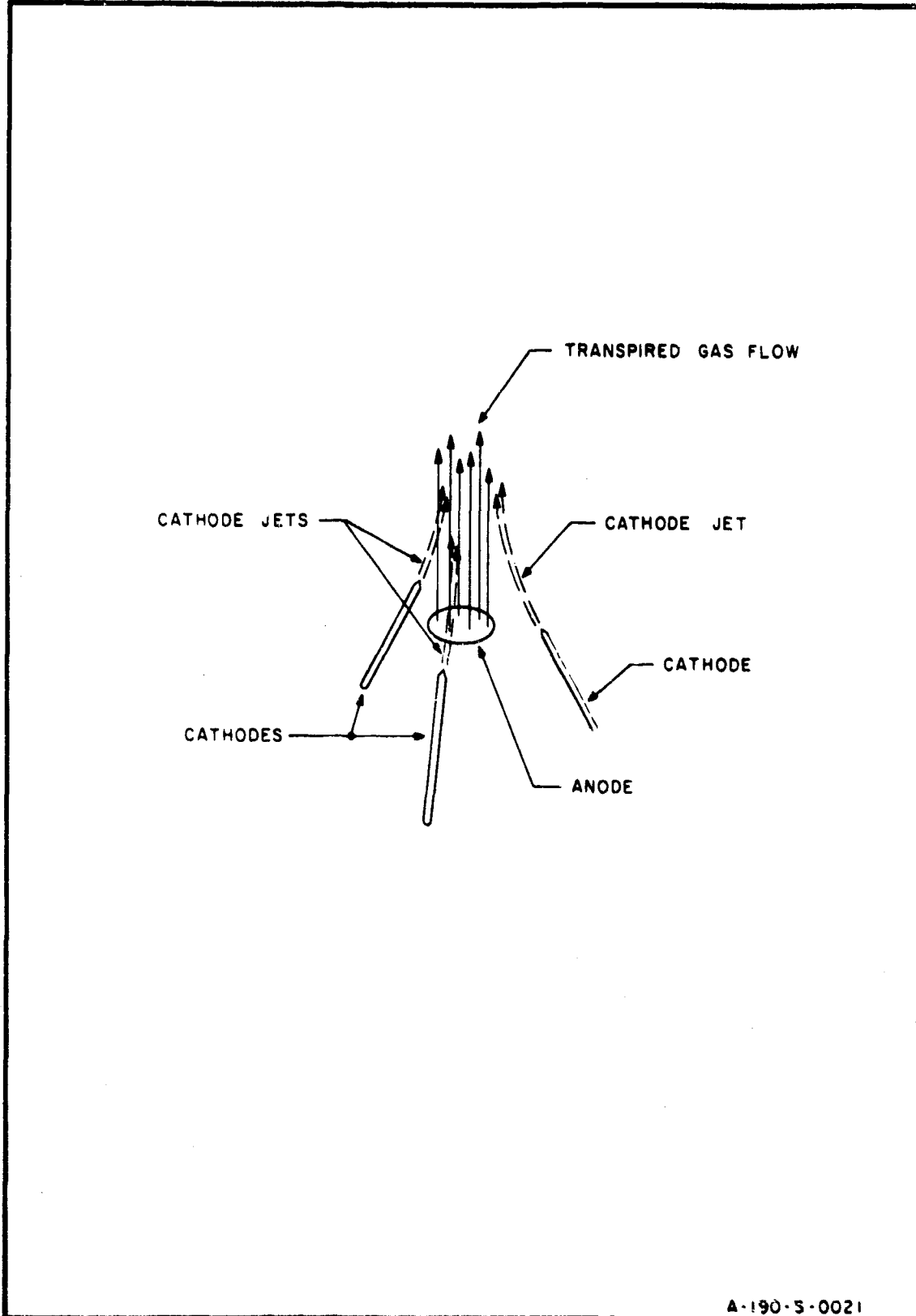
symmetrically about the anode axis. Figure 25 illustrates this geometry in the operating configuration.

The triple cathode was successful in generating an extended (6 to 8 cm long) symmetrical cylindrical column. This is seen in Figure 26. After a limited use in the diagnostics program, however, this configuration was abandoned when the FCC was introduced, because it was found that the same results could be achieved with a single cathode when the latter was used as a FCC.

(b) FTA/FCC combination with inclined geometry

(refs. 1 & 3)

This combination was used for the major portion of the diagnostic program. The two electrodes are positioned with axes inclined at about 45°, as shown in Figure 27. By properly regulating gas flows at both anode and cathode the large turbulent mixing zone previously encountered can be made quite small and distinct positive and negative columns generated. Further the lengths of each column segment can be adjusted almost at will over a wide range with surprisingly low arc voltage. Figure 28 shows this unit in operation and indicates the "clean-cut" column segments and smooth merging of anode and cathode flows. In this illustration the negative column was 7 cms long, and the anode column about 4 cms long with a total arc voltage of only 76 volts. The anode dark space (non-equilibrium zone) mentioned in section IIA above is clearly visible on the right of the figure.



A-190-5-0021

FIG. 25 TRIPLE CATHODE ARC IN SWEPT-BACK GEOMETRY



FIG. 26 ARC JET GENERATED BY TRIPLE CATHODE ARC ASSEMBLY



FIG. 27 SINGLE CATHODE FCC-FTA COMBINATION



FIG. 28 SINGLE CATHODE FCC-FTA COMBINATION IN OPERATION  
(200 AMP., ARGON, 1 AM.)

This configuration represents an ideal device for laboratory studies of plasma phenomena. In addition to the virtually complete accessibility, it is exceptionally reliable, a unit of this type having been operated almost daily for over a year without maintenance of any kind.

(c) Conical FTA (refs. 1 & 4)

The conical configuration was developed to provide a free-burning single-ended plasma jet having the same features as the cylindrical FTA but with the added feature of unidirectional flow. Originally the motivation was to develop an arc heater which would retain the high efficiency characteristic of the FTA, and could mate with an expansion nozzle without the need for an intermediate settling chamber. Later the conical configuration was also considered as a radiation source.

The construction of the unit is shown schematically in Figure 29. The cathode has the usual conical tip but the porous anode consists of a truncated conical shell positioned upstream of the cathode tip. The anode current-receiving surface is therefore annular and the column is in the form of a conical lamina. The transpiration gas flows convergently toward the cathode tip where it merges into a single unidirectional effluent jet. In the operation of this device a minimum arc current is required in order to establish the current termination completely around the anode annulus. This depends on the size of the annulus. For a unit having an anode 1/2" TD x 3/4" OD, a current of 200 amps was found to be required. Figure 30 is a

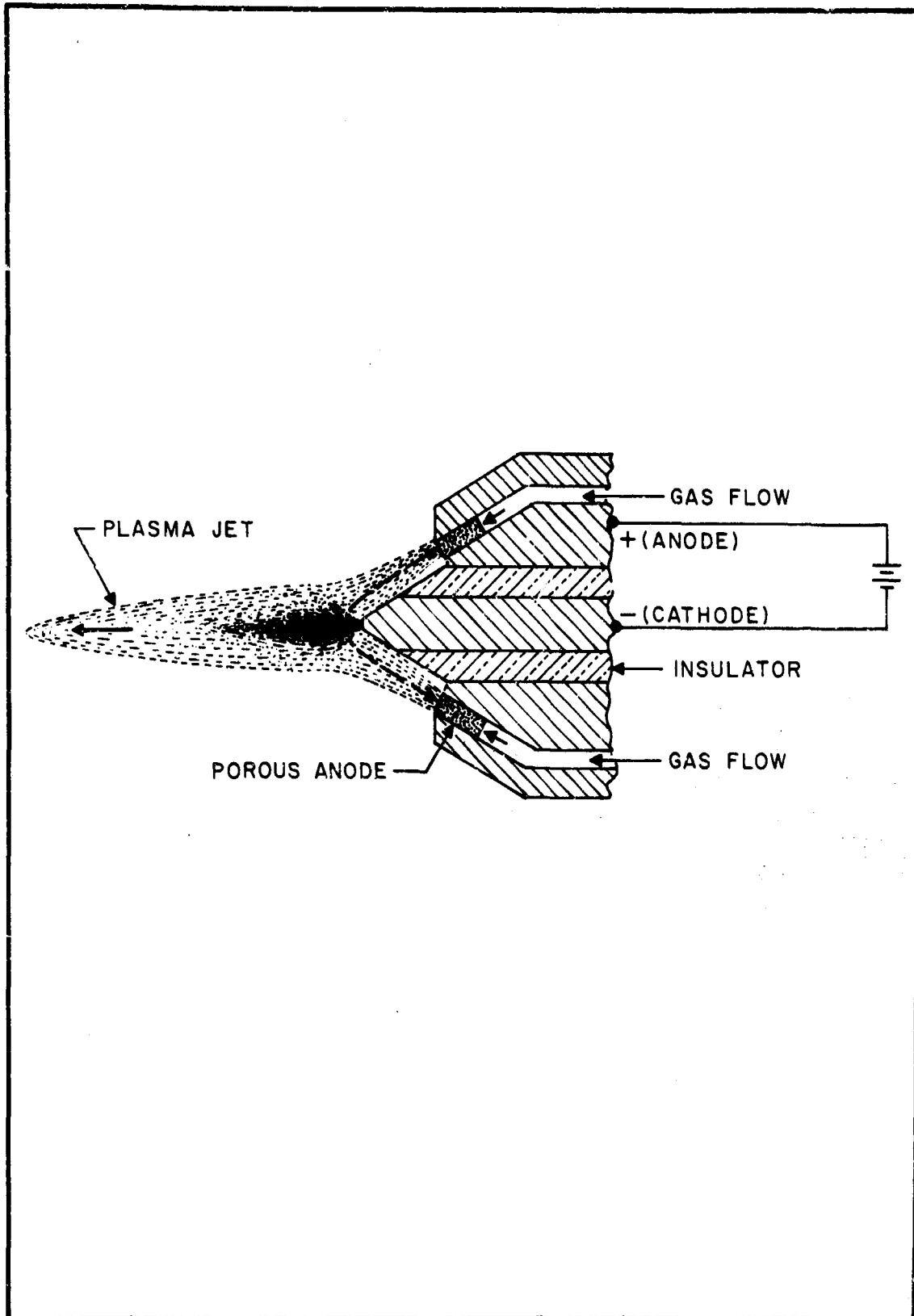


FIG. 29 CONICAL VERSION OF FTA



FIG. 30 CONICAL FTA IN OPERATION (300 AMP, ARGON, 1 ATM.)

photograph of this unit in operation. Note that all of the plasma generated including the arc column is external to the apparatus. Efficiencies in the range of 80 to 90% are easily achieved. Although this configuration has not yet been tested as a wind tunnel arc heater, recently a number of conical FTA units have been applied to other heating purposes (arc melting and welding) and found to perform better than the more conventional wall-stabilized plasma torch.

(d) FTA-FCC combined in opposed geometry

Since this configuration was designed exclusively for the work on the radiation source, it will be described in subsection D, below.

(3) Porous anode development (ref. 1)

Most of the work on porous anode development was carried out early in the program and was concerned chiefly with testing the porous anodes for uniformity of the transpiration flow field. This was deemed essential when certain anodes showed a considerable streakiness in the effluent column which was attributed to a non-uniform permeability in the anode itself. The tests involved measuring the flow field a few mm from the exit face of the anode by scanning the surface diametrically with the Pitot tube probe. In testing a given specimen two mutually perpendicular scans were made. Illustrations of typical test results on NC-60 graphite anodes are shown in Figures 31 and 32. These represent the cold flow fields for a poor specimen and a good specimen, respectively. Specimens exhibiting flow non-uniformity such as shown in Figure 31 were

DRAWN	CHECKED
	APPROVED

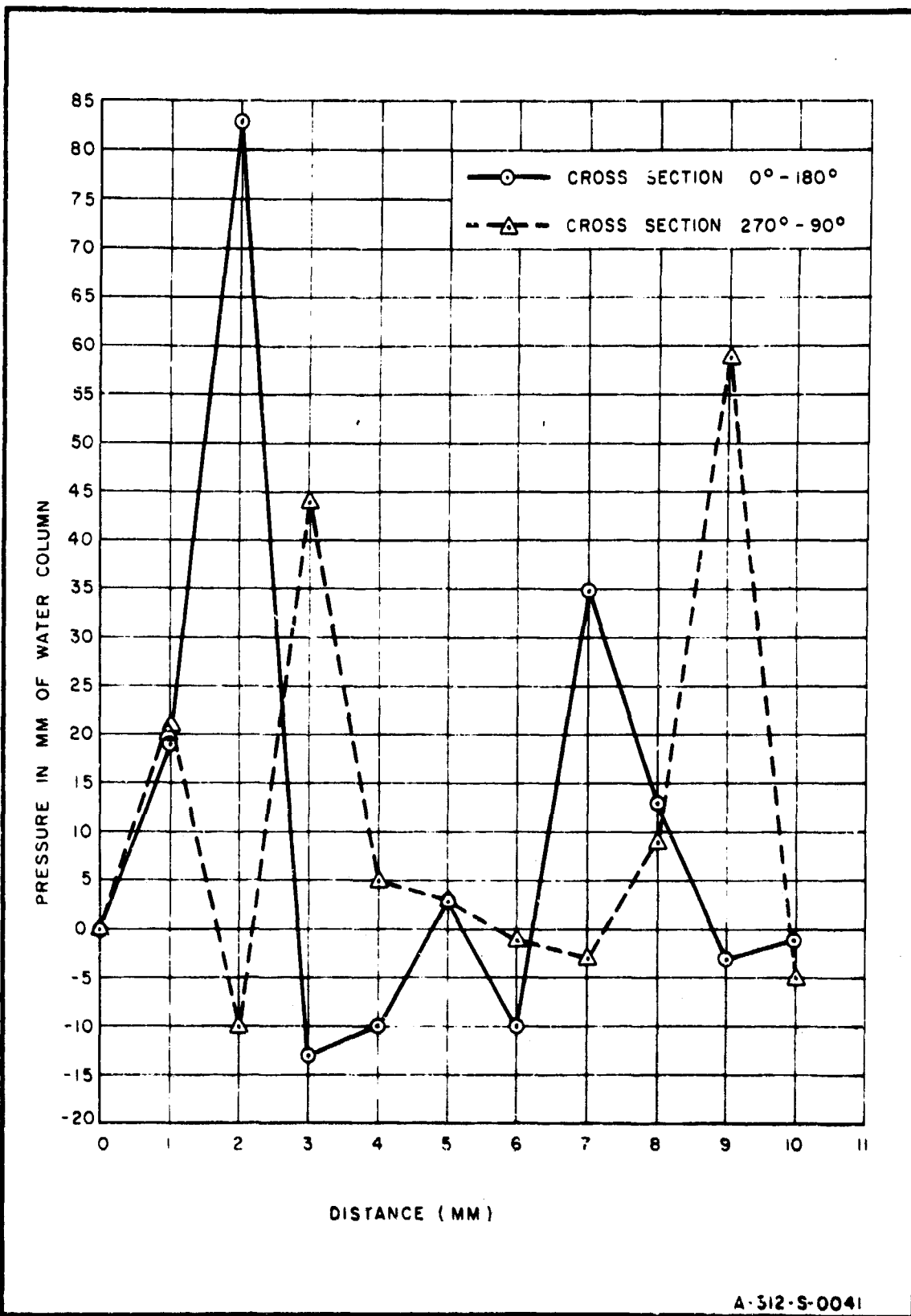


FIG. 31 CROSS SECTIONAL DISTRIBUTION OF COLD FLOW NEAR ANODE FACE (NC-60 GRAPHITE - POOR SPECIMEN)

DRAWS	CHECKED	APPROVED
-------	---------	----------

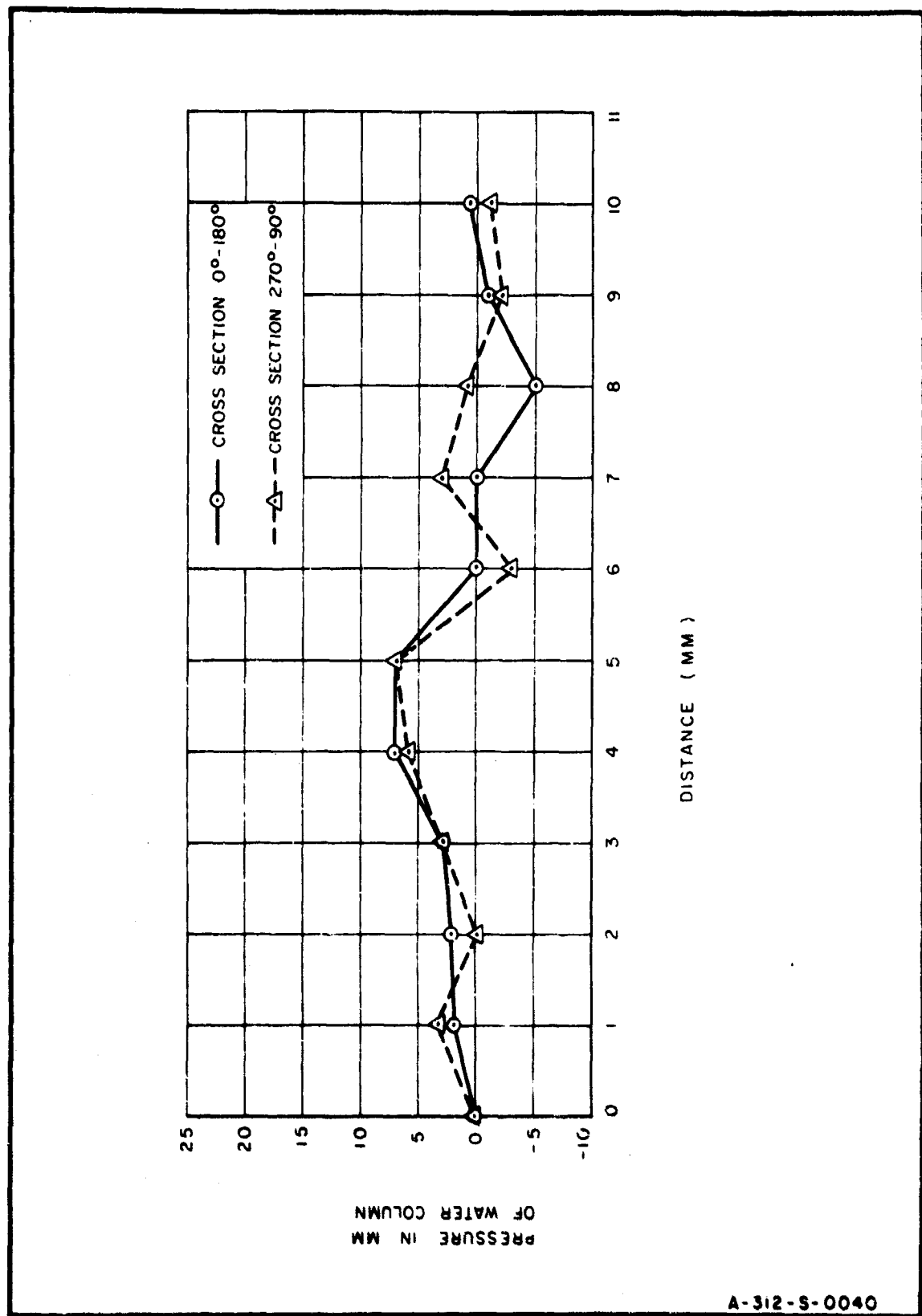


FIG. 32 CROSS SECTIONAL DISTRIBUTION OF COLD FLOW NEAR ANODE FACE (NC-60 GRAPHITE - GOOD SPECIMEN)

of course rejected.

This method of quality control was also extended to the sintered tungsten anodes used in the later phases of the project, particularly in the radiation source work. It was found useful in revealing anodes which for one reason or another had not been properly sintered.

In addition to quality control testing further refinement in the fabrication procedure relating to sintering time and compacting pressure was achieved. As a result the tungsten anodes used in the radiation source work suffered only minor damage during extensive running. Further this damage appeared to be independent of running time and was finally related to the number of arc ignitions to which the particular anode had been subjected.

(4) Arc ignition phenomena (refs. 5 & 6)

The problem of ignition damage to the porous anodes used in the FTA became apparent during the work on the radiation source. A program was therefore initiated to investigate the nature of this effect, which was carried forward until the end of the contract period. Although a discussion of some of the findings and the application of remedial measures are presented in refs. 5 and 6, the details of the experimental phases of this investigation leading to a successful resolution of the problem have not heretofore been reported. A complete report of this subject is therefore contained in Section III below.

D. Radiation Source (refs. 1,4,5, &6)

Earliest consideration of the radiation properties of the FTA involved the use of the conical configuration (Figures 29 and 30). Visual observation indicated a rather concentrated zone of high brightness just beyond the cathode tip. A rather crude measurement of the spectral distribution (ref. 1) of the radiation emitted by the conical FTA was carried out early in the project period. The results seemed to indicate a relatively high emission of continuum radiation. Owing to lack of suitable radiometric equipment the early results are not considered conclusive. In fact it now appears that the infra-red portion of the spectral distributions (Figure 40, ref. 1) contained radiation which came from the glowing tip of the cathode. Further work on the radiation characteristics was deferred until the 1967-68 period when appropriate radiometric equipment became available.

(1) Opposed geometry configuration

Toward the beginning of the radiation study the decision was made to replace the conical FTA configuration with a combination of the FTA and FCC in an opposed geometry. There were several reasons for this decision. For example, although the single-ended nature of the conical FTA would allow a large solid angle for light collection (e.g.  $\sim 8$  steradians), difficulty was anticipated in designing a transparent envelope which would contain the high speed effluent jet. Secondly, preliminary tests on the independent control of forced convection at the cathode of the conical configuration were largely negative. It was nevertheless

considered to be a considerable advantage for a radiation source to be able to increase the temperature near the cathode tip by controlling the gas flow (see Figure 9). The configuration adopted for the radiation source study consisted of the FTA/FCC combination similar to the arrangement of Figure 27, except that the cathode and anode axes are maintained in a collinear position. This is illustrated diagrammatically in Figure 33. In this configuration the two jets collide in the interelectrode space. If the anode and cathode flows are properly balanced, the combined gas flares radially outward and is eventually caught up in a flow of sweep gas for heat exchange and recirculation to the electrodes.

This geometry is adaptable to a relatively simple cylindrical envelope. Further, the gas flow at the cathode can easily be controlled first to provide the optimum temperature in the column and then the anode flow adjusted to obtain proper balance of the two jets. A simplified model of this geometry was constructed and tested (ref. 4) with encouraging results.

#### (2) Radiation source equipment

The major part of the effort during 1967 was devoted to the design, construction and assembly of equipment. This included the new lamp together with its housing and control console as well as auxiliary instrumentation such as a radiation calorimeter and radiometric apparatus for the measurement of spectral irradiance.

A photograph of the source is shown in Figure 34 and the control console in Figure 35. Diagrams of gas and water circulation systems are shown in Figures 36 and 37.

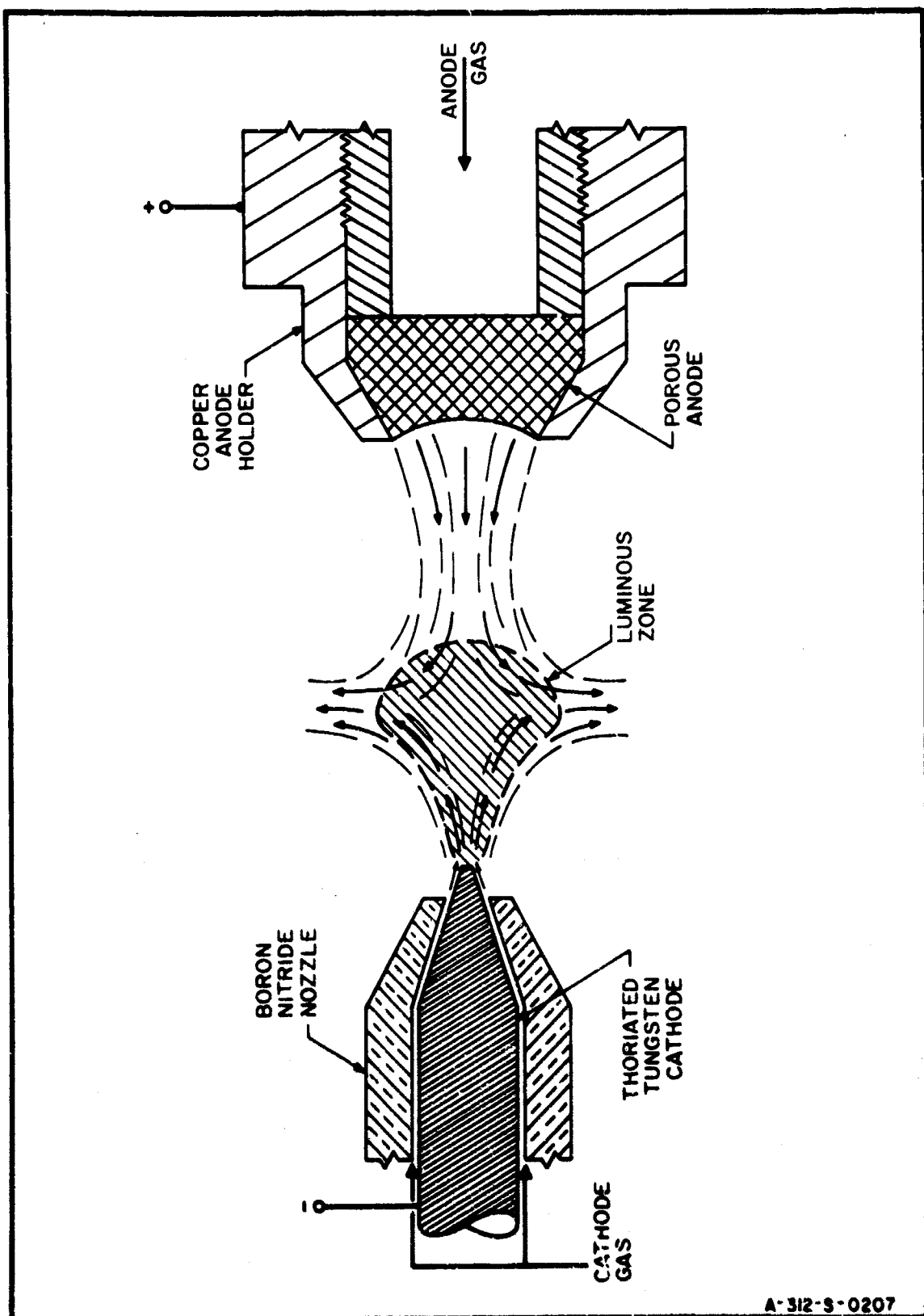
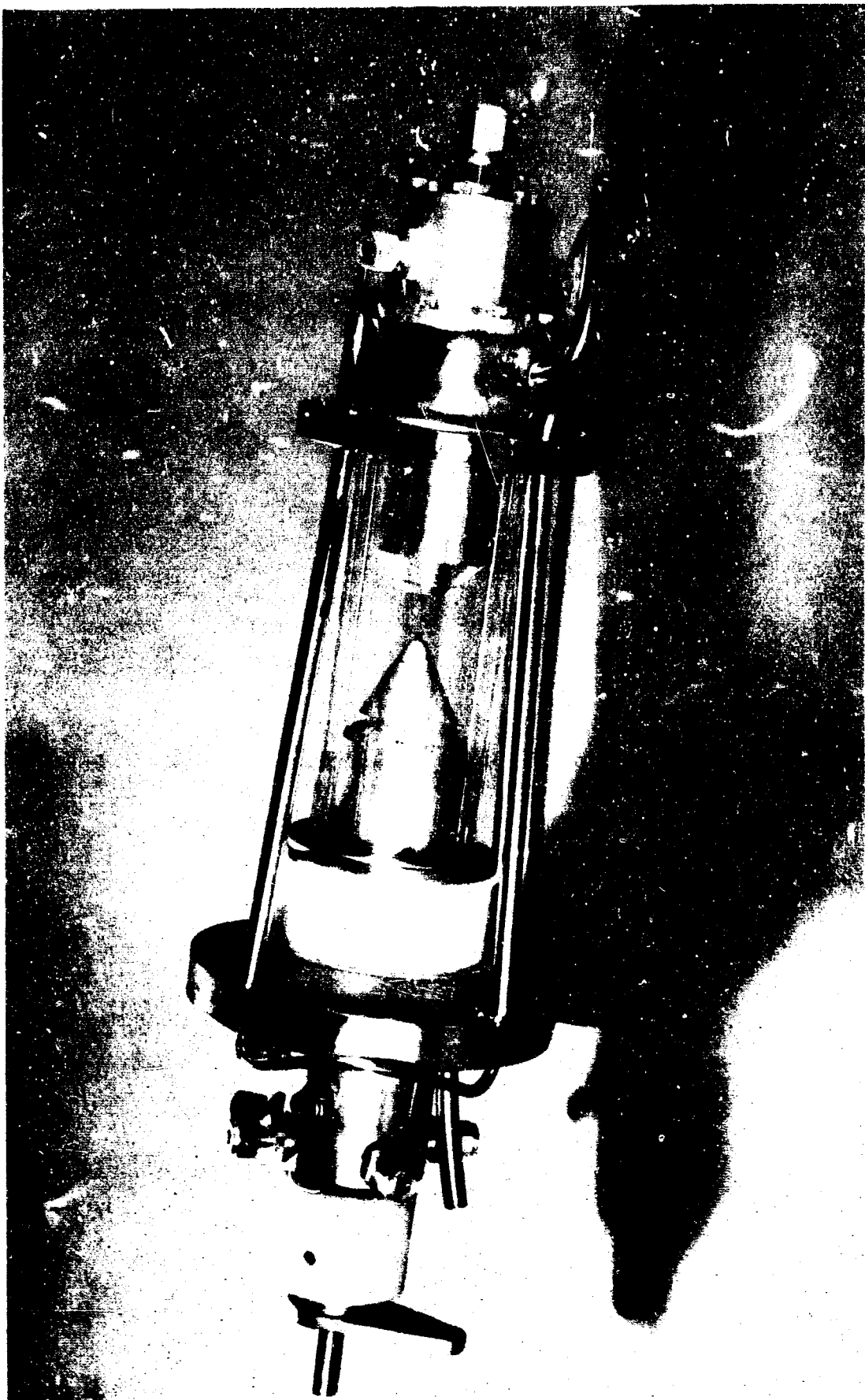


FIG. 33 SKETCH OF COLLINEAR OPPOSING FLOW FCC - FTA COMBINATION

FIG. 34 PHOTO OF COLLINEAR FCC-FTA ARC LAMP



F-1/312

92

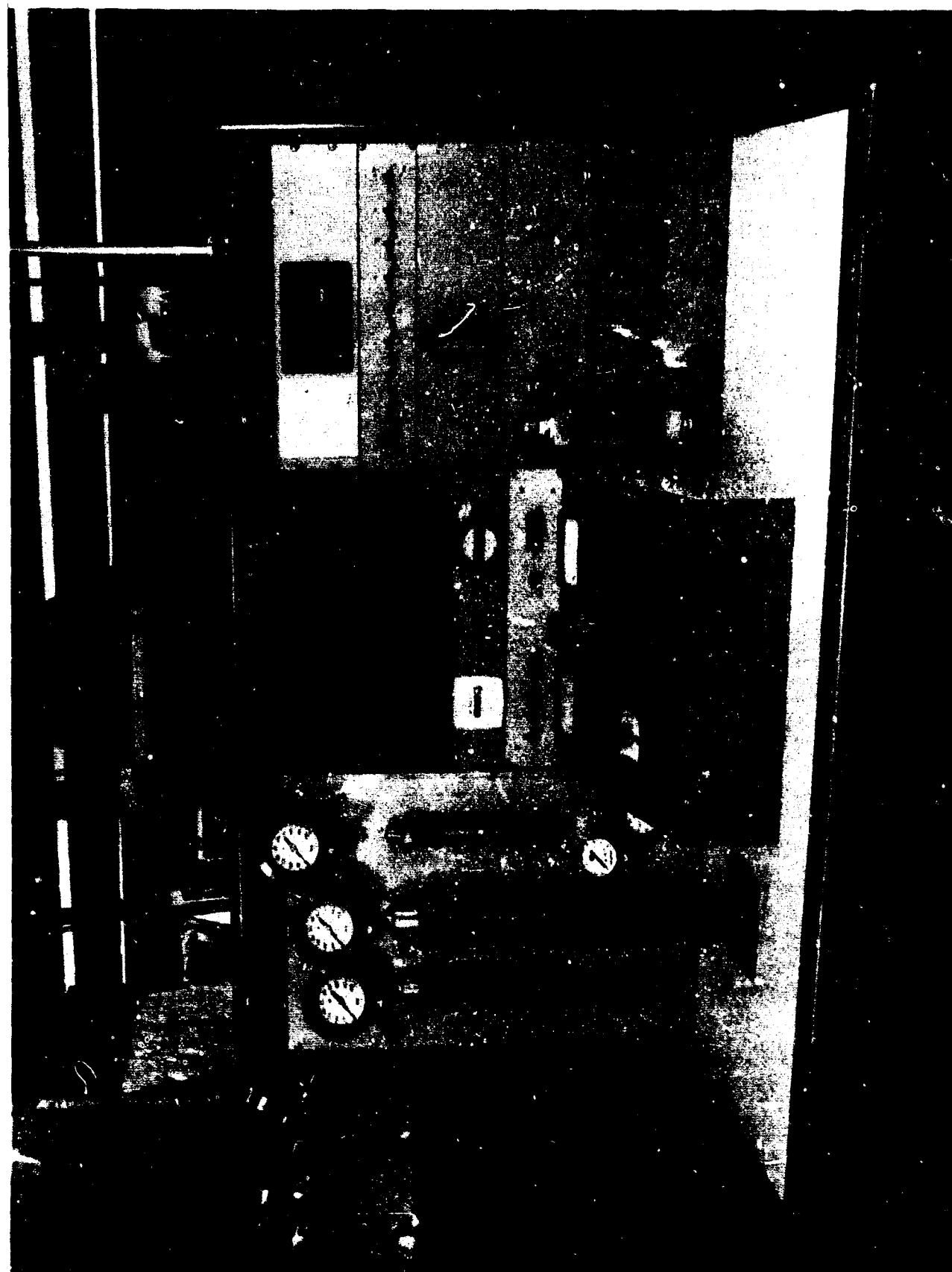


FIG. 35 PHOTO OF LAMP CONTROL CONSOLE

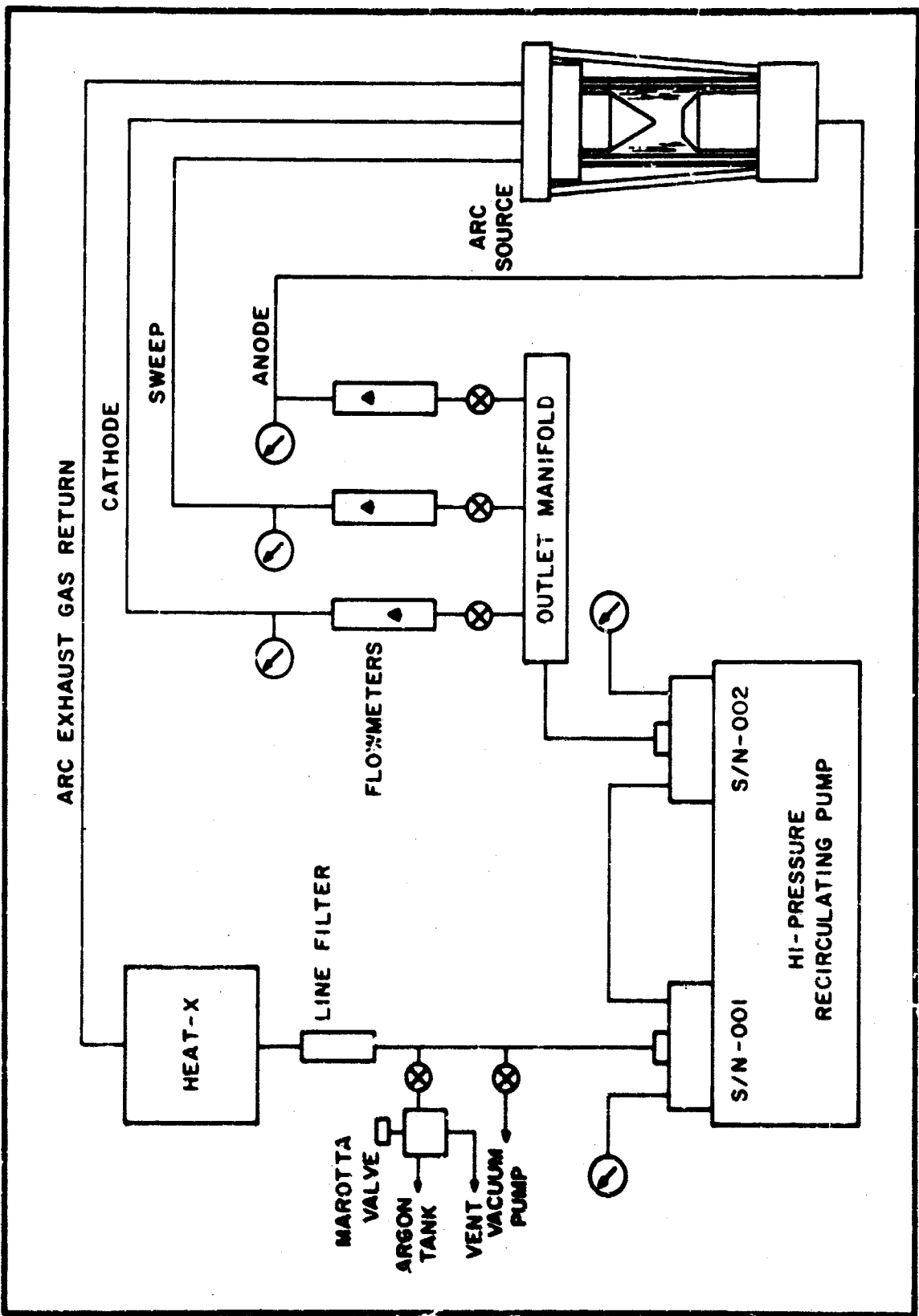


FIG. 36 SCHEMATIC DIAGRAM OF RADIATION SOURCE GAS FLOW SYSTEM

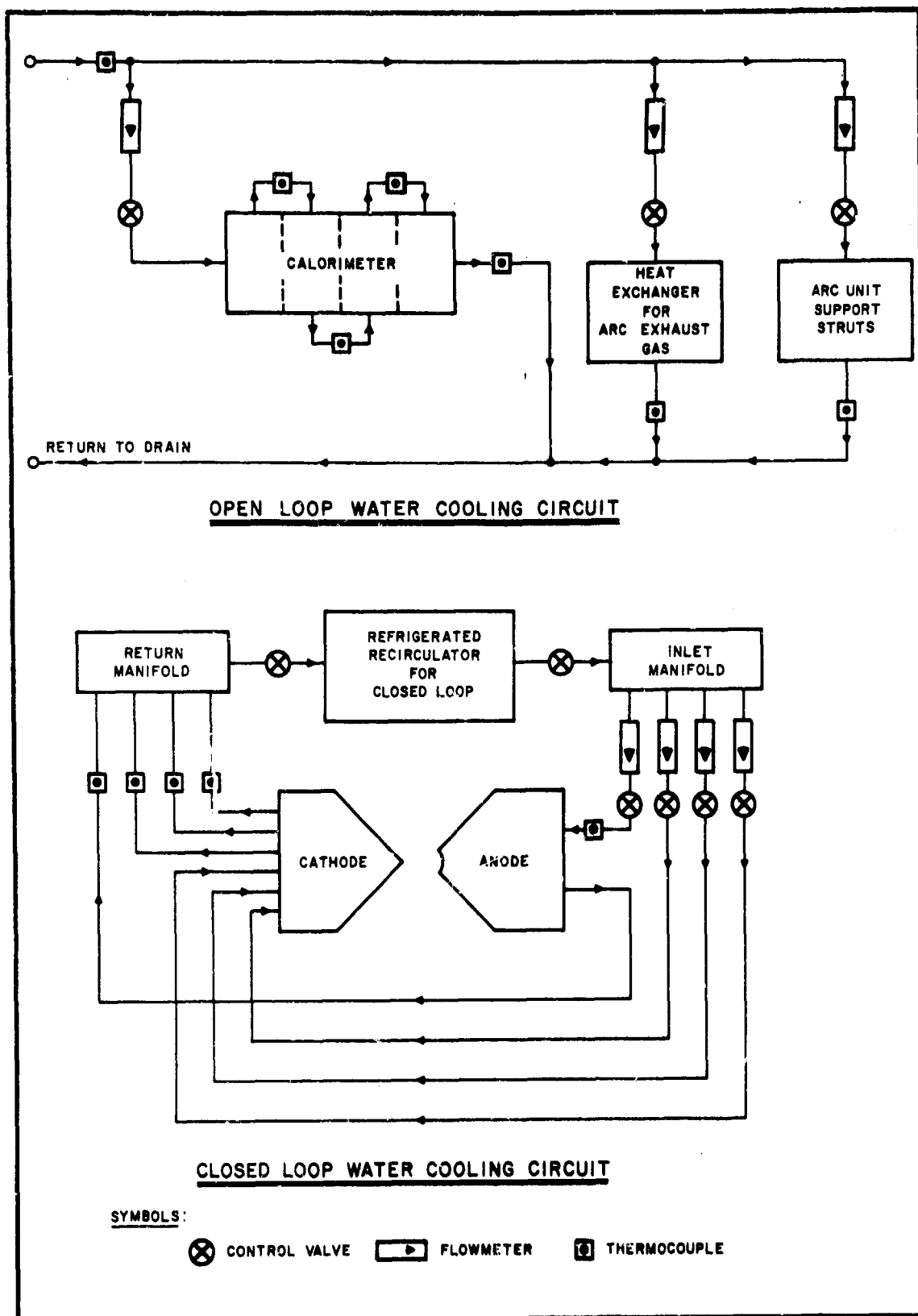


FIG. 37 SCHEMATIC DIAGRAM OF RADIATION SOURCE WATER COOLING CIRCUITS

The calorimetry equipment, which was used to evaluate the total radiant conversion efficiency of the source, consisted of a double-walled tank in which the lamp was inserted; the interior surface of the tank was blackened to facilitate absorption and the flowrate and temperature rise of the water circulated between the double walls were monitored in the usual manner to determine the radiated power. The set-up used for spectral irradiance was essentially that described by Stair et al<sup>(32)</sup>. Light from the arc source was introduced into an integrating sphere and thence passed through a light chopper into a Leiss double quartz prism monochromator. The beam emerging from the monochromator was detected alternately by a thermoelectrically controlled lead sulphide detector (in the range of  $2.5\mu$  to  $0.7\mu$ ), and an Ascop photomultiplier tube (in the range  $0.7\mu$  to  $0.25\mu$ ). The detector outputs were fed into a Brower lock-in amplifier and thence to an Omniphotic recorder synchronized with the wavelength dial of the monochromator. A diagram of the radiometry system is shown in Figure 38.

(3) Test results

The testing phase of the radiation source work began early in 1968 and was continued to the close of the contract period. In this section a summary of the results reported in ref. 6 (Jan. 1 to Sept. 30, 1968) is given. The results obtained after Sept. 30, 1968 are described in Section III below.

The arc was operated in the power range of 5 to 10 KW at envelope pressures of 50 to 180 psi of argon. Initially

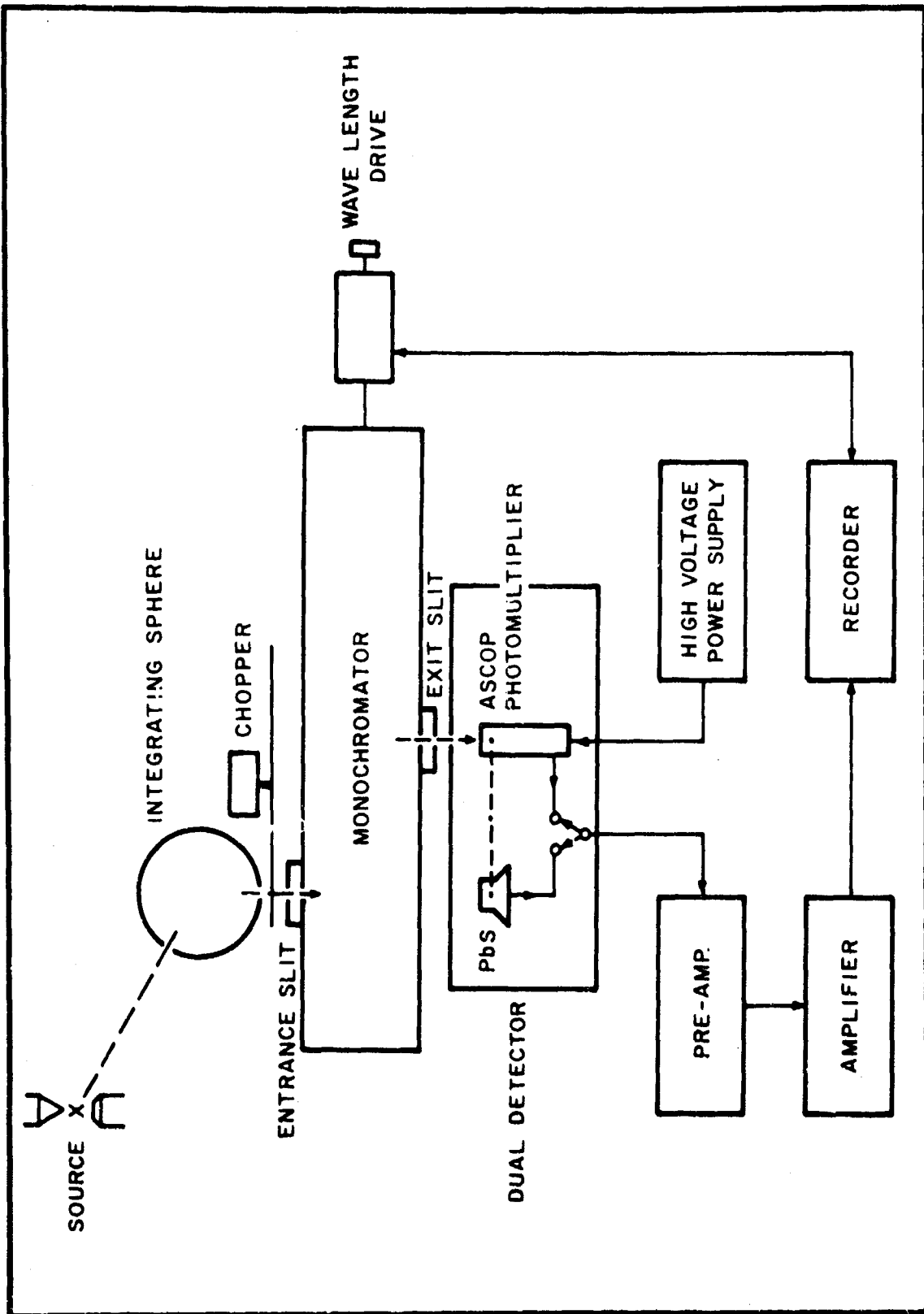


FIG. 38 SCHEMATIC DIAGRAM OF RADIOMETRY ARRANGEMENT

considerable difficulty was experienced in achieving stable operation, especially at the higher power and pressure levels. A series of operational tests led to two changes which made a sufficient improvement in operating stability to permit performance tests to be made. One such change was the addition of apparatus to vary the arc gap during operation. This was accomplished by a motor-driven hydraulic ram which changed the anode axial position via a sealed bearing in the housing. The capability of gap adjustment largely eliminated the tendency of the arc column to jump from the porous surface to other parts of the anode holder.

The second problem involved a strong tendency for the column to assume a curved off-axis path with randomly varying angular position about the axis. This difficulty was finally diagnosed as resulting from an unfavorable pressure distribution inside the envelope. This in turn was caused by the combination of the tangentially fed sweep gas, which produces an axial pressure minimum, and the stagnation zone due to the collision of anode and cathode jets, which produces an axial pressure maximum. The combination of the two produces an off-axis region of minimum pressure concentric to the axis. Since the arc column forms in accordance with the minimum energy principle the minimum length higher pressure path on the axis becomes competitive with the longer length minimum pressure path off axis. The arc column jumped to an off-axis position whenever the reduced off-axis pressure was more than enough to compensate for the longer path.

This problem was partially solved by changing the sweep gas from a vortex flow to a flow parallel to the axis. This reduced the off-axis minimum pressure zone sufficiently to permit stable axial operation at power inputs up to 10 KW and envelope pressures up to 150 psi. At still higher power and pressure levels the tendency of the column to form in the off-axis position reappeared. It was concluded that scale-up to higher power operation would require a redesign to the lamp housing. Because of the lack of adequate time in the remaining contract period this was not attempted.

The first performance parameter measured was the radiant conversion efficiency, defined as the total radiated power divided by the electrical power input. Some 28 measurements of conversion efficiency were carried out with variation in arc current, voltage, gap and envelope pressure. A summary of some of the later measurements is shown in Figure 39. Here the conversion efficiency is plotted against power input since the efficiency traditionally tends to increase with power level. Also plotted for comparison are the performance data for the 20 KW Hanovia short arc xenon lamp and the Tamarack jet-pinched arc operating in argon at 27 KW. It is seen that the FTA/FCC source compares favorably with these units despite the fact that our measurements were made at less than half the power input. A conversion efficiency of >40% in argon at a power input as low as 5 KW represents a distinct advance in lamp performance and implies that in xenon at power levels > 20 KW efficiencies ~ 60% should

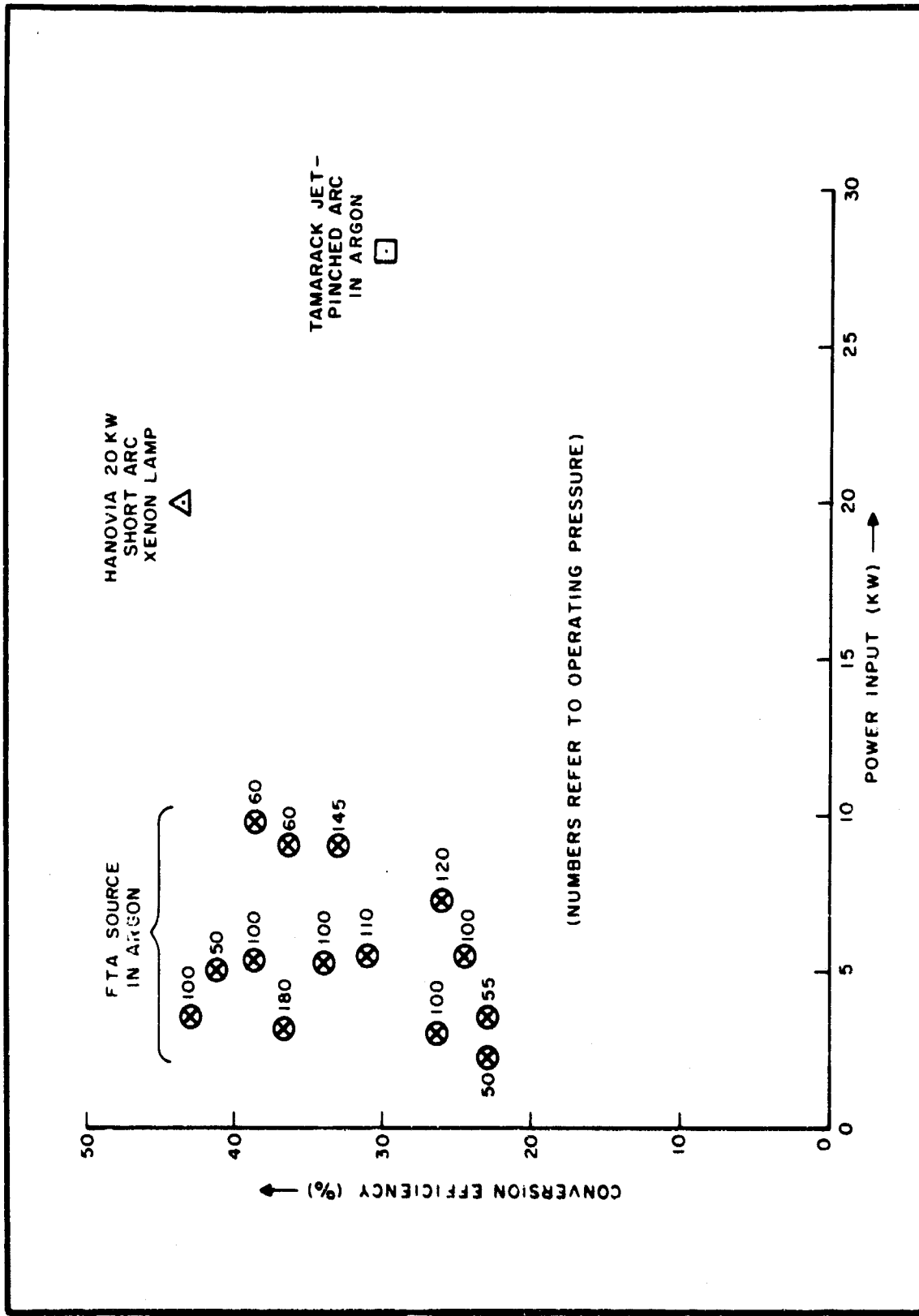


FIG. 39 CONVERSION EFFICIENCY TEST RESULTS

be obtainable from this unit.

The tests on spectral irradiance and the measurement of the micro-brightness profile of the FTA/FCC source, most of which was performed subsequent to Sept. 30, 1968, is presented in Section III-B, below.

### III. Recent Progress

This section deals with results achieved subsequent to the date of the last interim progress report (ref.6) and which have therefore not been previously reported. Two areas of progress are involved, namely, the details on the investigation of arc ignition phenomena, and the results of spectral irradiance and micro-brightness profile measurements for the FTA/FCC radiation source.

#### A. Arc Ignition Phenomena

The first indication that the process of arc ignition was responsible for electrode damage arose during an early investigation of the FTA<sup>(33)</sup> in which the erosion rate of porous (NC-50) graphite anodes was measured for several total running times. The results obtained in these early tests are summarized in Table 5. The fact that the erosion rate (gms/sec of anode weight loss) decreased markedly with increased running time strongly suggests that a fixed amount of anode ablation occurs at an early period and that little if any ablation occurs thereafter. The figures in the total weight loss column of Table 5

TABLE 5

EFFECT OF TOTAL OPERATING TIME ON FRICTION RATE  
 (NC-50 Graphite Anodes, Argon, 1 Atm.)

Specimen No.	Voltage (volts)	Current (amps)	Flow Rate (gms/min)	Total Weight Loss (gms)	Total Operating Time (sec)	Erosion Rate (gms/sec)
NC-50-38	25	108	100	0.0357	70	51 x 10 <sup>-5</sup>
NC-50-33	25	90	100	0.02327	705	3.3 x 10 <sup>-5</sup>
NC-50-40	23	90	100	0.02418	1860	1.3 x 10 <sup>-5</sup>

tend to confirm this conclusion. Visual observation of porous tungsten anodes, with the aid of a small telescope focussed on the anode, showed the sudden appearance of small molten patches on the surface as soon as the arc was ignited. Moreover, the size of the molten areas did not increase regardless of how long the arc was kept operating thereafter. This observation lends support to the occurrence of transient thermal damage to the surface of the anode associated with the ignition process.

As an initial working hypothesis, it was assumed that the phenomenon of ignition created a small conduction area on the anode surface, on which a very high current density was momentarily created, and which lasted long enough to cause local overheating. To test this hypothesis, some experiments were run, using sintered tungsten anodes, comparing the appearance of the anode surface when the arc was ignited by a single spark with one which had been ignited by multiple parallel sparks. This was accomplished by using an igniter electrode having multiple prongs held equidistant from the anode surface. It was anticipated that multiple parallel sparks would produce several ignition zones which would share the starting current thereby reducing somewhat the local thermal loading. The results are shown in the photographs of Figure 40. The top photograph, which shows the anode surface after ignition by a single spark, displays a relatively large molten area which covers nearly half of the column contact area. In the bottom photograph, which shows the anode after ignition

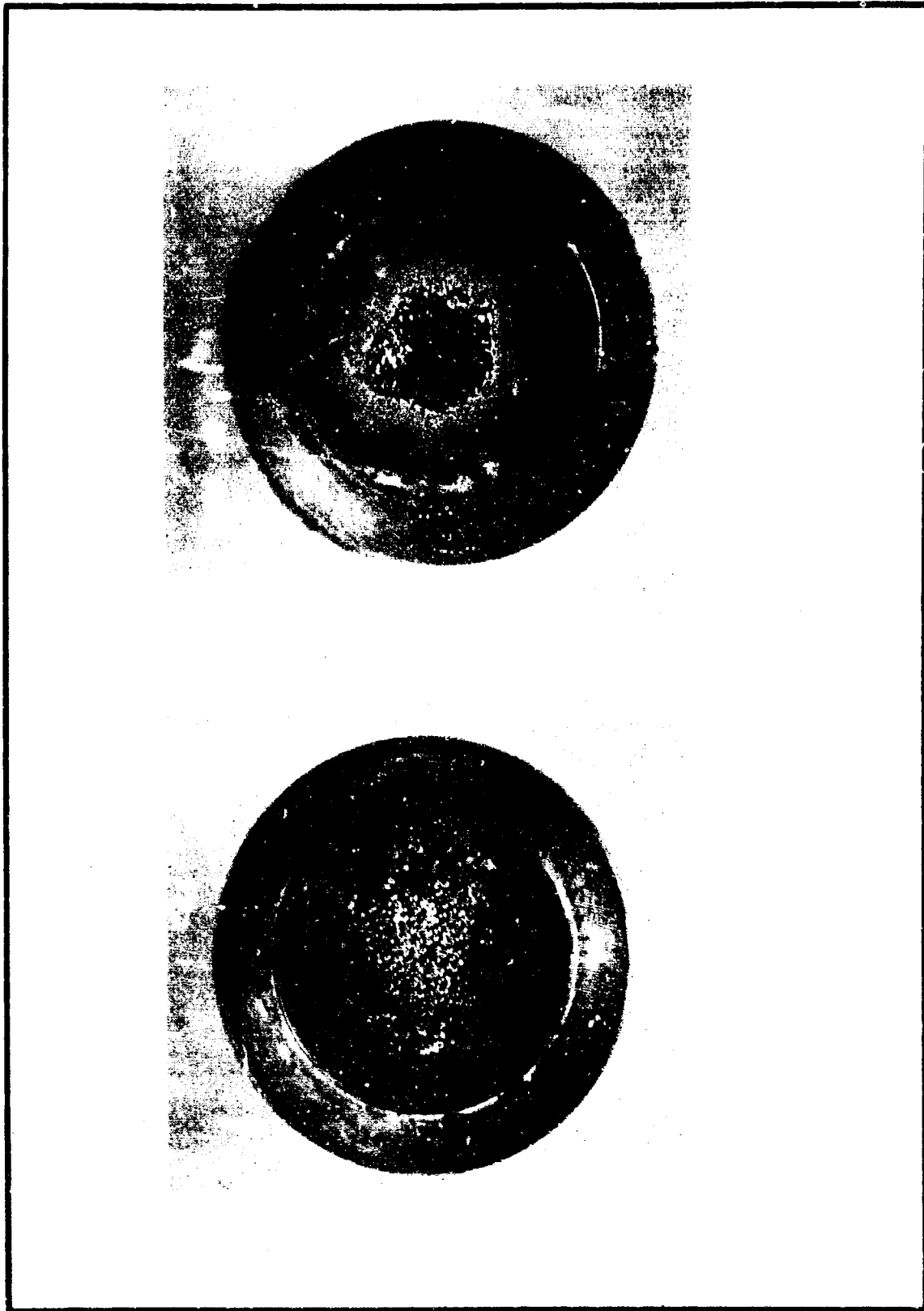


**FIG. 40** EFFECT OF MULTIPLE SPARK IGNITION  
TOP: Single Spark  
BOTTOM: Multiple Spark

by 5 or 6 parallel sparks, the degree of visible melting on the surface is considerably reduced.

Following this experiment it was decided to investigate in detail the transient variation in those arc parameters which contribute to thermal damage. The power absorbed per unit area of anode surface is given by

$$P_a = J_a (V_a + \phi_a) = \frac{I}{A} (V_a + \phi_a) \quad (26)$$

where  $J_a$  = current density at anode surface

$V_a$  = anode sheath voltage

$\phi_a$  = anode work function

$I$  = total arc current

$A$  = contact area of column on anode surface

$\phi_a$  depends only on the anode material and remains constant in time. For arcs in steady state, the anode sheath voltage,  $V_a$ , depends mainly on the nature of the gas and the operating pressure, with slight dependence on the arc current. However, since information on the growth of  $V_a$  during the transient period was lacking, it was assumed that there might be some correlation between  $V_a$  and the total arc voltage. Hence the arc parameters considered to be involved in initial thermal loading are  $I(t)$ ,  $V(t)$ , and  $A(t)$ . In addition to these the mass flow rate,  $\dot{m}$ , must also be involved for the FTA, since this parameter is effective in removing some of the absorbed heat. While the inlet pressure might be maintained constant, there is no assurance that the flow remains constant during the ignition sequence.

### (1) Test procedures

It was decided to use porous graphite anodes only for the analysis of the ignition transient. The reason for this is that erosion of graphite anodes (by sublimation or spalling) does not influence the transpiration of gas through the anode. If sintered tungsten anodes were used the surface melting during ignition might close off enough of the pores in the critical areas to make interpretation of results uncertain. Both National Carbon NC-60 and Stackpole 37G types of porous graphite were used.

The voltage transient was measured by connecting the arc terminals to the vertical input of an oscilloscope of suitable speed (Tektronix 502A), the oscilloscope being adjusted for a triggered sweep. The pulse used to trigger the sweep was also fed through a variable time delay to the arc igniter, so that all phases of the ignition process could be made to appear on the trace. The traces were recorded on a standard oscilloscope camera.

For the current transient the same technique was used except that the signal was obtained from the current metering shunt and passed through an Enesco ADS-95 amplifier before being fed to the oscilloscope terminals.

The arc current coverage area,  $A(t)$ , was determined photographically with the aid of a Fastax motion picture camera. The latter was run at a speed of 1000 frames per sec., providing 1m-sec

resolution for the area measurement. The resulting films, exposed to show magnified pictures of the anode surface, were projected on a screen and the coverage area determined graphically. The time parameter for a given frame was determined by counting the number of frames, starting from the first exposed (spark) frame.

In the case of the mass flow parameter, the measurement was performed by means of a Venturi tube using a Wianko P2-4109-3 variable reluctance differential pressure gauge to obtain the mass flow signal. At the same time the inlet pressure was also monitored via a CEC 84145-0-600 strain gauge pressure transducer, in order to obtain information on flow resistance during the transient period.

Two types of power supply were used during the tests. The first of these was a standard commercial arc welding supply, the Miller SR-1000-C7 unit, which has a drooping current characteristic and is commonly used to supply power to plasma generators. The second was a special power supply designed and built to have a nearly perfect constant current characteristic. By using only solid state rectifiers and controls the response time of this supply was reduced to <20 m-sec. This source was introduced chiefly as a result of the first observations on the current transient using the Miller supply.

(2) Test Results

(a) Current and voltage transients

Oscillograms of the current and voltage transients for the NC-60 and 37G anodes, using the Miller power supply, are shown in Figures 41 and 42, respectively. The similarity of the corresponding traces for the two types of anode is quite noticeable. This is taken to signify that the observed responses are not greatly dependent on porous anode physical properties, since NC-60 graphite has a much higher permeability, lower density, and broader pore size distribution than the 37G graphite.

The observed current transient response is especially interesting. Referring to the upper traces of Figures 41 and 42, it is seen that (reading from left to right) at the moment of ignition the current jumps suddenly from zero (lowest horizontal graticle line) to about 160 amps, which is more than twice the steady state current of 70 amps at which level the current control on the Miller supply had been set prior to ignition. Actually there is a short high frequency oscillation (more evident in Figure 42 than in Figure 41) just after ignition, probably due to the ringing of the resonant circuit comprising the transformer inductance and its distributed capacitance. This damps out quickly, however, ( $\sim 0.1$  sec.) and is not considered important as regards thermal effects. The most surprising aspect of the current transient is that the current continues to rise, following the initial ringing, for a

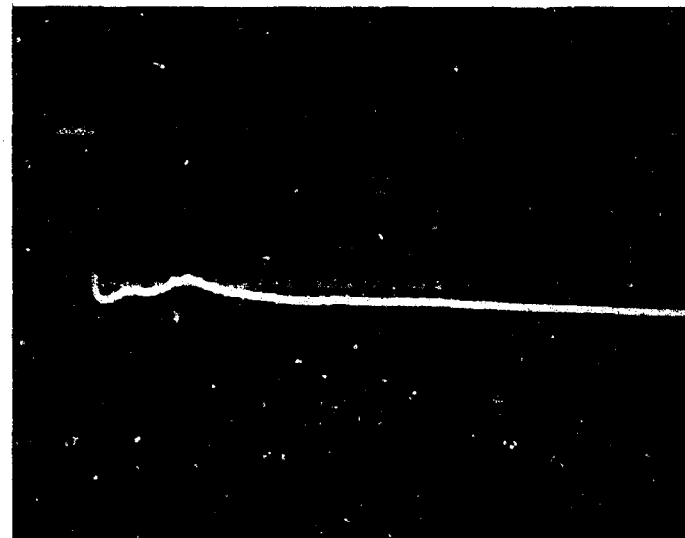
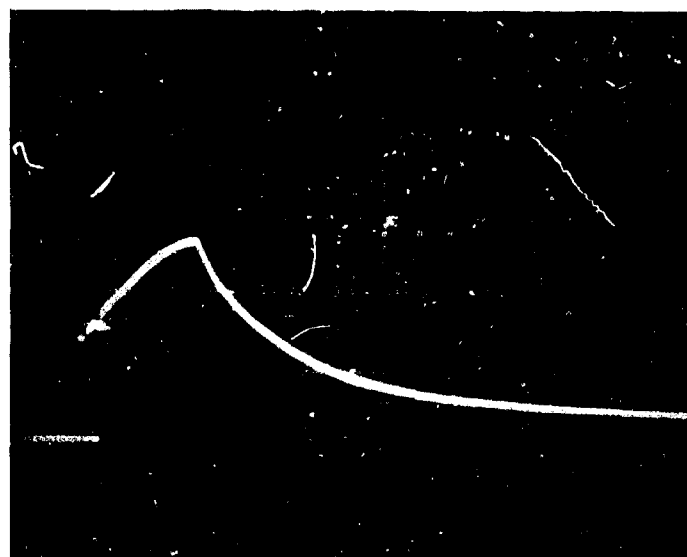


FIG. 41 CURRENT TRANSIENT (TOP) AND VOLTAGE TRANSIENT (BOTTOM)  
FOR NC-60 ANODE AND MILLER POWER SUPPLY.  
(HOR.: 0.5 sec/div.; VERT.: UPPER - 125 amp/div.,  
LOWER - 50 volt/div.)

F-1/312

109

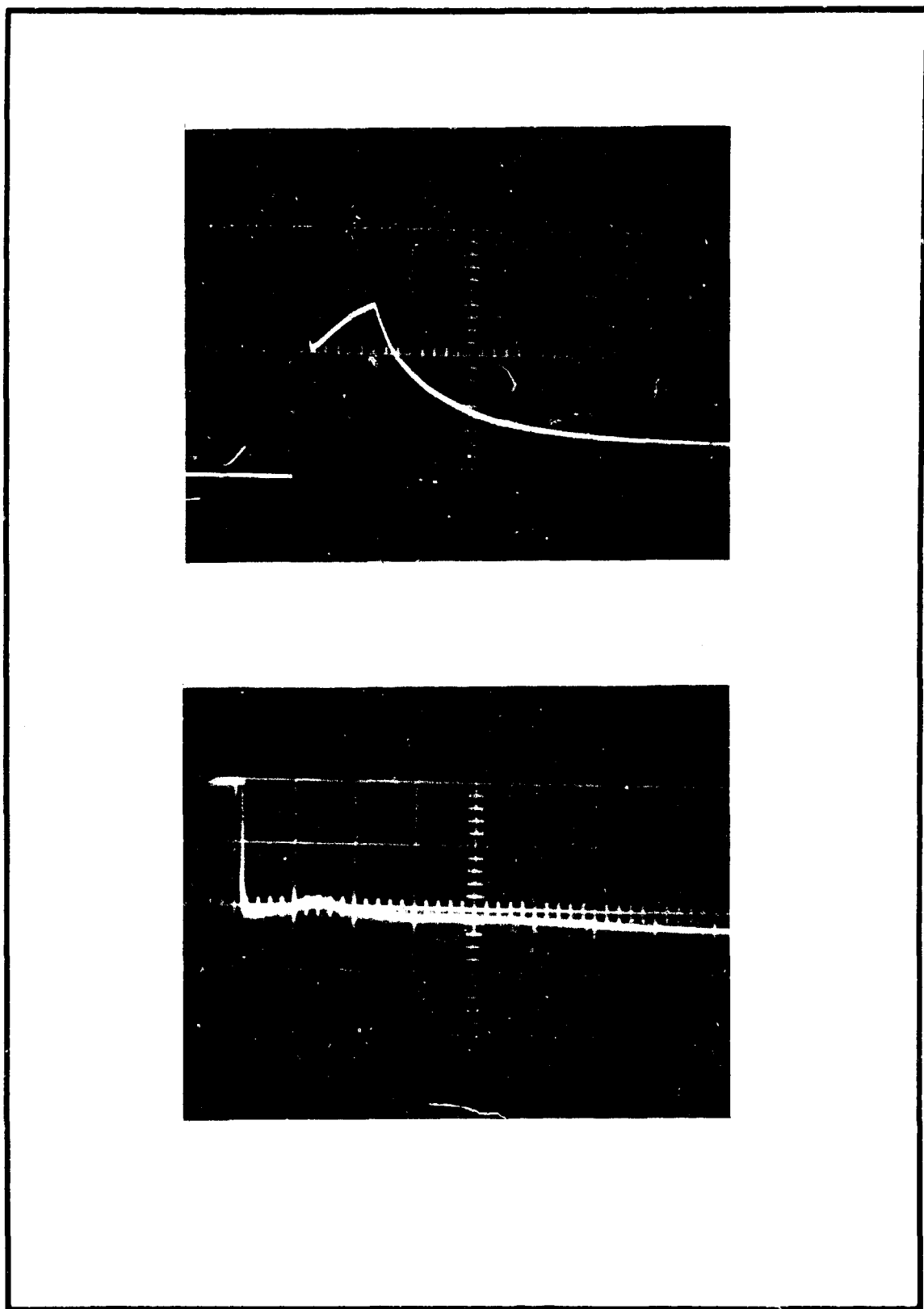


FIG. 42 CURRENT TRANSIENT (TOP) AND VOLTAGE TRANSIENT (BOTTOM)  
FOR 37G ANODE AND MILLER POWER SUPPLY  
(CALIBRATIONS SAME AS FIG. 41.)

period of about 0.75 sec., reaching a value of 350 amps., i.e. about 5 times the steady state current. After reaching a peak, it abruptly begins to decrease, in an exponential manner, reaching the steady state value approximately 3 seconds later. This phenomenon obviously represents a complex interaction between the power supply and arc circuits while both power supply and arc characteristics undergo radical changes between initial and steady state conditions. One can infer that the power supply has a considerable lag in the control of current ( $\sim$  1 sec) since this is accomplished by the desaturation of a large saturable core transformer. It can also be assumed that during the early phases of the spark to arc transition the discharge may exhibit the negative resistance characteristic commonly observed in non-convective arcs. This would account for the large initial current and its further rise. The abrupt change in slope to a decreasing current after 0.75 sec. can then be interpreted as due to the power supply control circuit "taking hold", i.e., achieving sufficient core desaturation to begin limiting the arc current, which thereafter settles slowly into the fully regulated condition at steady state.

A theoretical analysis of this current behavior was not attempted, primarily because of lack of knowledge of the discharge characteristics during the growth period of the arc from the initial spark channel. From the standpoint of ignition phenomena, however, the important conclusion from the observed current

transient response is that the Miller supply and similar arc welder power sources have too slow a response time and permit current surges during the arc ignition process which are large enough and of sufficient duration to cause thermal damage to the electrodes. While this is of no importance in arc welding where electrode ablation is a desideratum, it could well account for the pitting of anode nozzles and similar damage which has been observed after repeated ignitions of arc lamps and plasma torches.

The voltage transient oscillograms (lower traces of Figure 41 and 42) show no unusual behavior. For both types of anode the arc voltage drops suddenly from the open circuit voltage (150 volts) to a value slightly above the steady state arc voltage (35 volts)\*, following which it executes several low amplitude fluctuations and then subsides during the next 2 or 3 second interval to the steady state value. Insofar as thermal effects are concerned, it is evident that the voltage transient is relatively unimportant compared to the current surge. The dissimilarity between the voltage and current transient wave-forms is indicative of the highly complex nature of the arc power supply circuit.

In view of the above results with the Miller power supply the experiments were repeated with a specially constructed power supply designed to eliminate the current surge. In this unit the saturable core transformer was eliminated and a fast current control circuit employing only solid state regulation was installed. Regulation was achieved by sensing the current from a series shunt and referring this to an adjustable reference voltage, the

\*The zero voltage reference level in the lower traces of Figures 41 and 42 is the second horizontal graticule line from the bottom.

comparison signal then being fed to a bank of water-cooled power transistors in series with the load so as to maintain a constant load current. This unit provided a much more constant current supply than the conventional arc welder source. For example the voltage-current characteristic of the Miller supply had a slope of a few volts per ampere in the operating range, while the slope for the constant current supply was 100 volts per ampere. In addition the response time for current regulation was < 20 m-sec.

With a power source of these characteristics it was expected that the large current surge following ignition could be eliminated. This expectation was verified as may be seen in the oscillograms of Figures 43 and 44. These represent the current and voltage transients for NC-60 and 37G anodes respectively, using the constant current power supply. In particular the current responses show that the arc current rises from zero to its steady state value within about 50 m-sec. of ignition. (The nature of the current transient between 0 and 50 m-sec. was not investigated since it was deemed to be thermally unimportant.)

A considerable improvement was noted when sintered tungsten anodes were ignited with the constant current supply. Although melting on the surface was not eliminated, it was considerably reduced in magnitude, generally appearing as a few scattered melted areas about 1 mm. or so across. Such anodes could be used for 4 or 5 ignitions before thermal damage made replacement necessary.

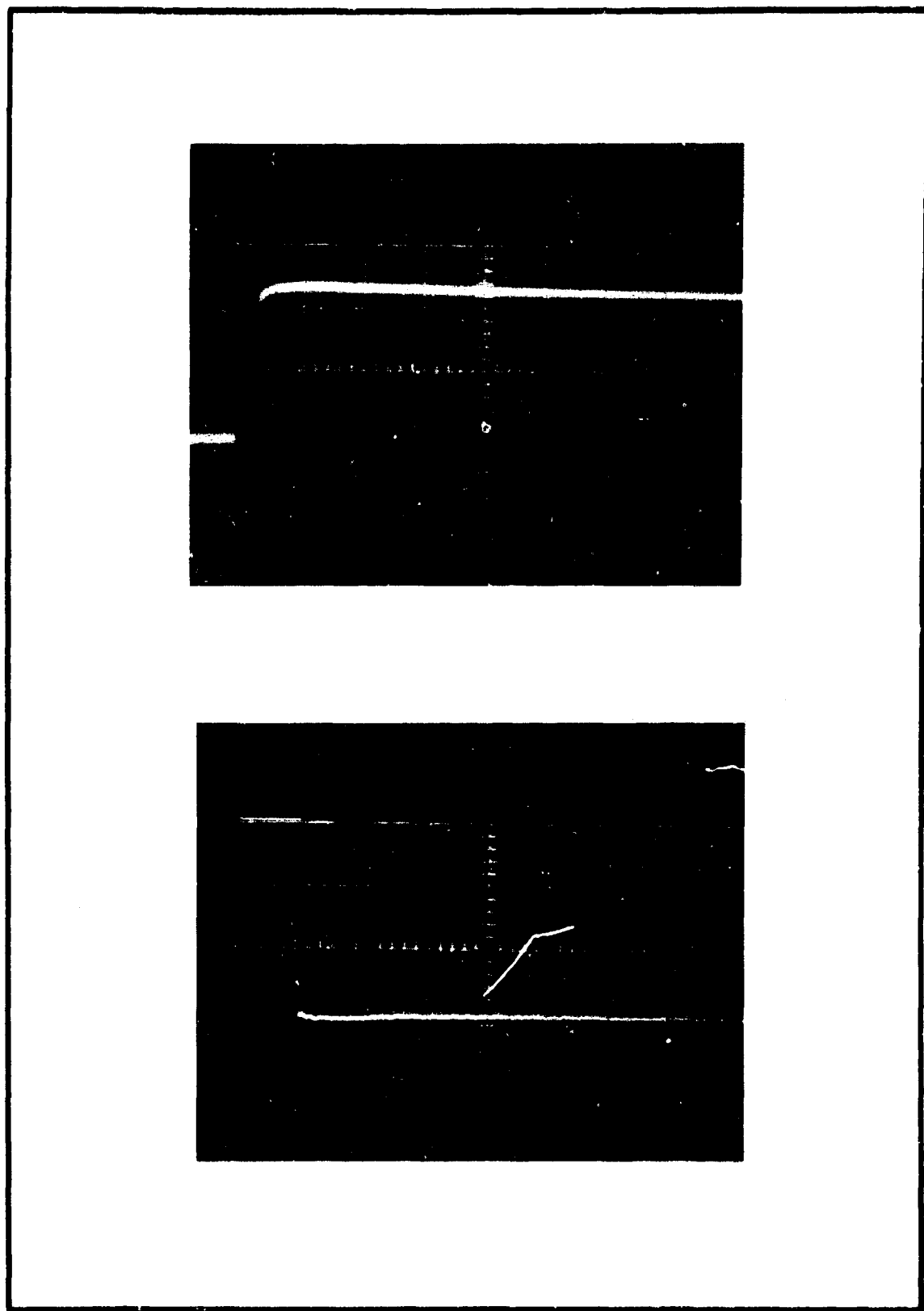


FIG. 43 CURRENT TRANSIENT (TOP) AND VOLTAGE TRANSIENT (BOTTOM)  
FOR NC-60 ANODE AND CONSTANT CURRENT POWER SUPPLY.  
(HOR.: Upper - 0.2 sec./div., Lower - 0.5 sec./div;  
VERT.: Upper- 60 AMP./DIV., Lower - 30 VOLT/DIV.)

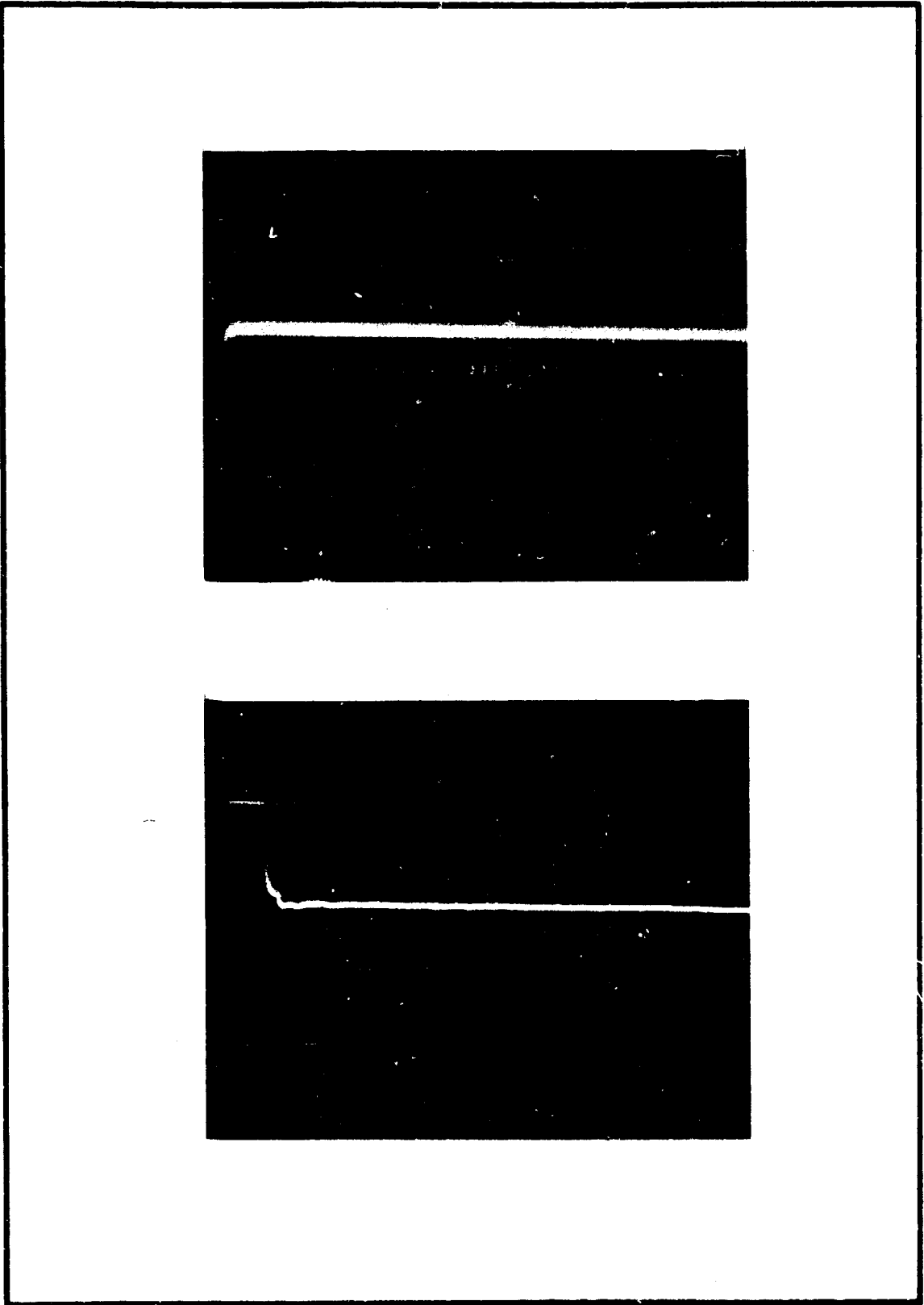
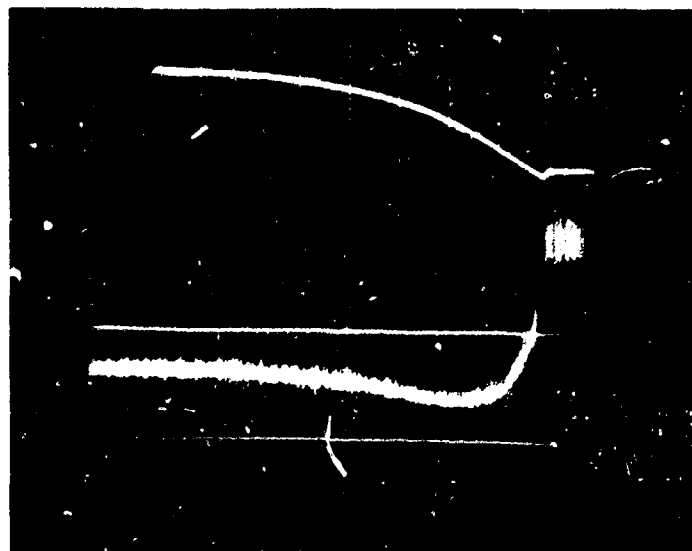


FIG. 44 CURRENT TRANSIENT (TOP) AND VOLTAGE TRANSIENT (BOTTOM)  
FOR 37G ANODE AND CONSTANT CURRENT POWER SUPPLY.  
(HOR.: 0.5 SEC/DIV.; VERT.: Upper - 25 AMP./DIV.,  
Lower - 50 VOLT/DIV.)

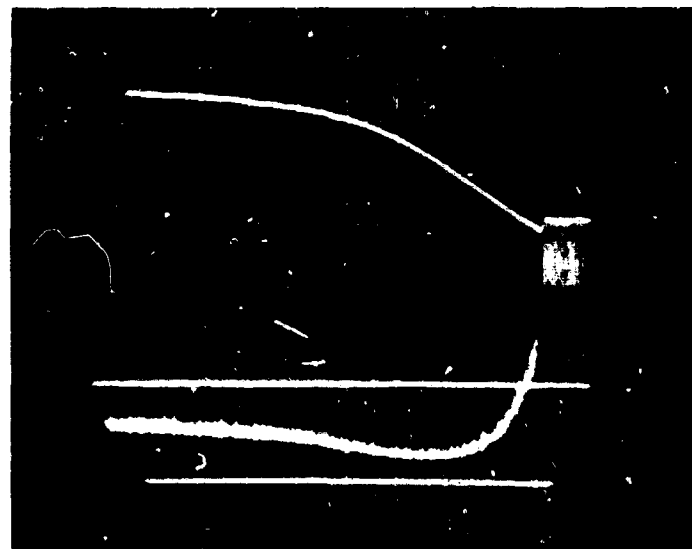
(b) Flow transient

The results of tests to determine the behavior of the gas transpiration through the anode during the ignition process are shown in Figure 45. These were taken using the Miller supply for NC-60 anodes only since the results were similar to 37G but the signal to noise ratio for the latter was lower because of the much lower permeability. The oscillograms consist of dual traces (in this case reading from right to left), one each for the pressure drop across the anode and for the mass flow of gas through it. The deflection between the uppermost trace and the upper of the two horizontal traces indicates the pressure drop. The flow transient is indicated by the deflection between the trace which before ignition (at the extreme right) is second from the top (and which can be recognized by the noticeable noise level, probably due to some turbulence in the Venturi flow gauge) and the bottom horizontal line.

At the moment of ignition (near extreme right) the pressure drops momentarily (for about 0.2 sec) and then rises slowly, reaching steady-state in about 6 seconds. The mass flow, following ignition, appears to drop suddenly to zero for 0.2 sec. Then it jumps to a value slightly less than the cold flow (pre-ignition) rate and despite the rising pressure, drops off to a minimum in 2 or 3 seconds; following this it rises slowly to a steady state flow in about 8 seconds, the value of which is approximately twice the minimum. The time parameters for this peculiar flow transient



100 AMP.



150 AMP.

HOR.: 1 SEC./DIV.

VERT.: Upper Traces - 22 G/MIN/DIV.  
Lower Traces - 17 psi/DIV.

FIG. 45 FLOW TRANSIENTS FOR NC-60 ANODE  
AT 100 AND 150 AMP.

are dependent on the steady state arc current as may be seen by comparing the upper and lower oscillograms of Figure 45, which were taken for 100 and 150 amps, respectively. Note that for the 150 amp case the flow at the minimum is closer to zero than for the 100 amp case despite a higher pressure across the anode.

The features occurring in the first 0.2 sec. of the flow transient are thought to be due to a shock wave associated with the rapid development of the ignition spark and possibly some early events in the spark to arc transition. This could cause a back pressure wave through the anode and could account for the momentary cessation of flow. Although considered to be too short in duration to have much average influence on thermal effects, it was recognized that even a short flow cessation during an initial period of high current density might not be entirely negligible.

The rising pressure and falling flow rate observed during the first second or two after the short transient period is considered to reflect the increased heating of the transpiration gas in the body of the porous anode. This would cause an increase in the viscosity and account for the rise in flow resistance of the anode.

The minimum in flow and subsequent rise to a higher steady state is attributed to the current surge which, as will be shown below, causes an "overshoot" in the current-carrying area on the anode surface. This would account for a similar variation in the transpirant viscosity and therefore in the flow resistance. The longer time constants for the flow transients, as compared to the current transients, is

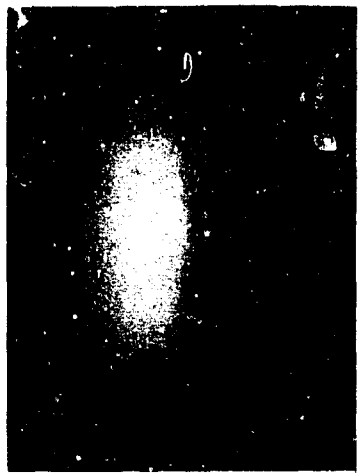
attributed to thermal lag. This explanation was further substantiated by noting that the area overshoot as well as the flow minimum were eliminated with the constant current supply. The main conclusion from the flow transient tests is that, when using a standard arc welding power supply arc ignition of the FTA causes a reduction in flow rate and therefore the degree of transpiration cooling of the anode concurrently with the current surge, thereby aggravating the thermal loading of the anode during the ignition process.

(c) Current density transient

The current density is of course the parameter most directly related to thermal loading of the anode during the ignition process. As mentioned earlier the coverage area of the discharge,  $A(t)$ , was obtained from Fastax motion pictures of the anode surface during ignition taken at 1000 frames per sec. The frames corresponding to specified time intervals were projected on a screen and traced on graph paper to evaluate the area. A selected series of frames is shown in Figure 46. The frame on the upper left is the first in the sequence and shows the ignition spark. (The channel is curved due to inclination of electrodes and gas blowing from the anode; the dark line in this and the next frame is the striker electrode which is inserted for ignition and pulled out of the discharge in about 20 m-sec.) Note that the anode termination in this frame is a



0



16



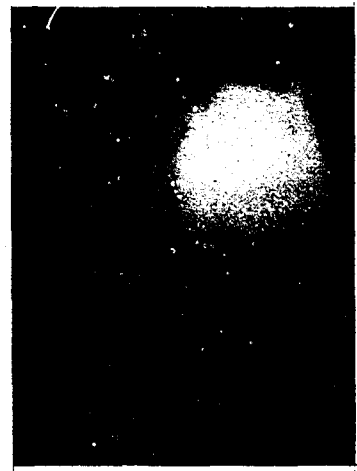
80



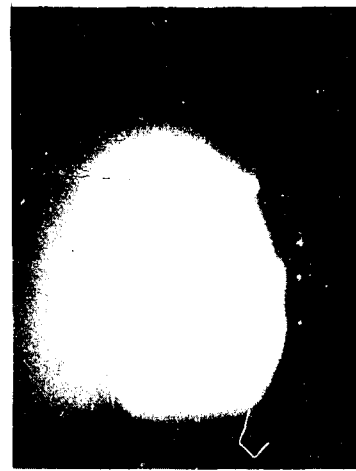
160



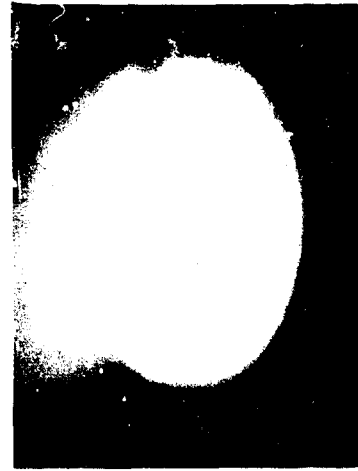
320



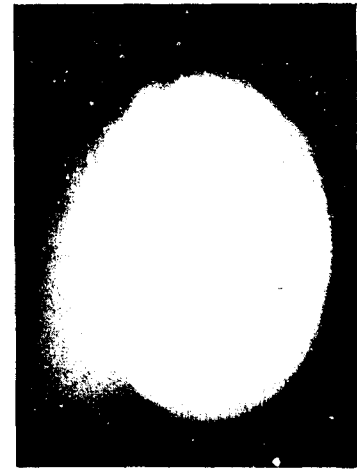
480



640



960



1,120

FIG. 46 FRAME SEQUENCE SHOWING BUILD-UP OF ANODE COVERAGE AREA DURING IGNITION

(Numbers refer to milliseconds of elapsed time from ignition spark)

single very small spot. Succeeding frames in Figure 46 (reading from left to right top and bottom) are marked by numbers indicating the elapsed time in milliseconds following the spark. As seen in the next 4 or 5 frames the ignition process for anode coverage consists of first a single very small spot, which quickly branches into a multiplicity of small spots during the early phases of the transition, after which the many small spots begin to coalesce, forming larger but fewer spots, this process continuing until after about 0.5 sec. a single large spot is formed. Thereafter this large roughly circular spot grows and either reaches a constant area or subsides to a smaller area, depending on the power supply used.

Curves of  $A(t)$  vs.  $t$  for both NC-60 and 37G anodes are shown for each power supply in Figures 47 and 48. In Figure 47, for the Miller supply, the coverage area for both types of electrodes rises nearly linearly for between 1 and 2 seconds and then subsides, reaching a steady value in about 4 seconds. For the constant current supply (Figure 48) the area rises steeply at first and then tapers off to a constant value in about 2 seconds. The differences between the curves for the two anode materials in both figures may be attributed to the differences in physical properties between the NC-60 and 37G graphites. The anode coverage area of an arc is determined mainly by the thermal balance between the heat input and the several energy sinks such as thermal conduction, convection to

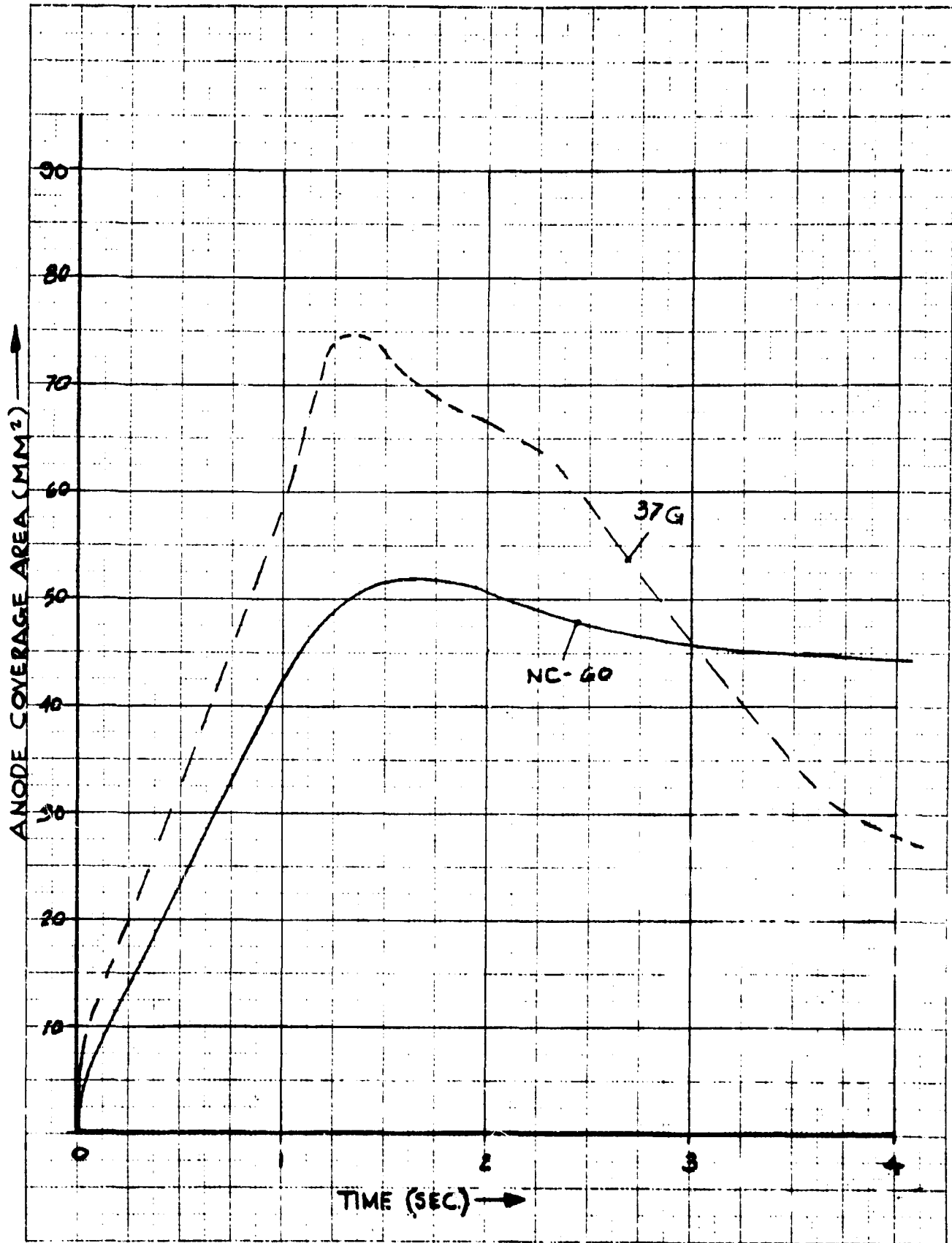


FIG. 47 AREA COVERAGE TRANSIENT FOR MILLER POWER SUPPLY

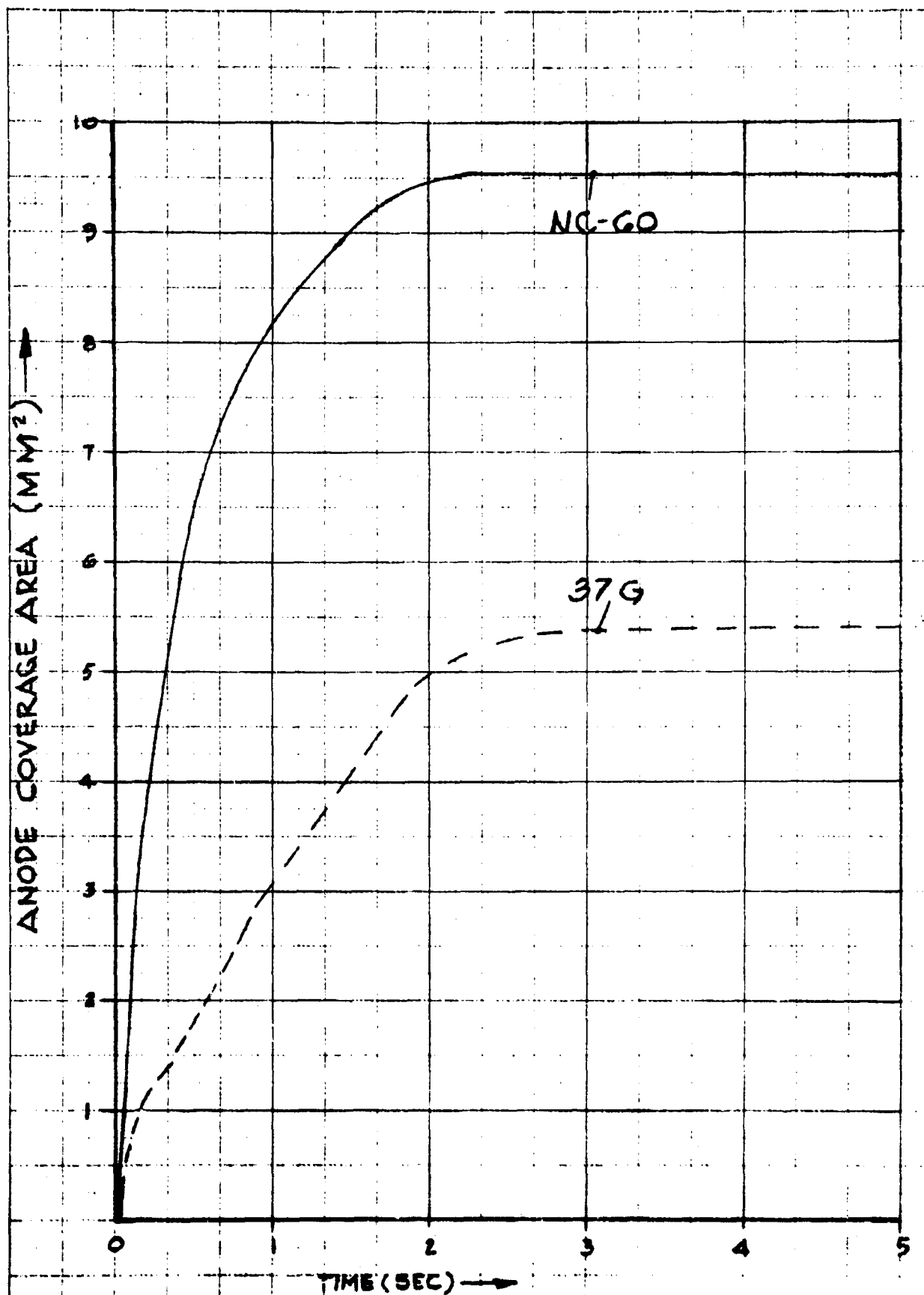


FIG. 48 AREA COVERAGE TRANSIENT FOR CONSTANT CURRENT POWER SUPPLY

the transpirant, radiation, etc. Hence differences in heat capacity and conductivity (bulk density), and in permeability and pore size are expected to result in the type of individual area transients observed.

The significant observation to be made from the area transients is that while they are qualitatively consistent with the respective current transients for each type of power supply, the time constants for the growth in area are in all cases longer than those for the rise in current. For example, in the case of the Miller supply the current peaks at 0.75 sec. after ignition while the area peaks at about 1.4 sec. Similar, for the constant current supply, the current rises abruptly to its steady state value for both NC-60 and 37G, while the area doesn't reach steady state until 2 sec. after ignition. This is probably the result of thermal inertia of the anode responding to the particular balance of heat source and sinks prevalent in each case. At any rate the conclusion is inescapable that for the first second or so following ignition very high current densities prevail on the anode surface. Moreover, as indicated by Figure 46, the interval of reduced anode area occurs over the same general time span within which the flow transient reaches its minimum thus aggravating the situation caused by the high initial current density. The effect is somewhat less for the constant

current supply. However, it is apparent that the current density transient for both supplies reaches values which can be locally destructive during the arc ignition process.

In order to illustrate the magnitude of this effect the data for the current and area transients (from Figures 41 and 46) were used to compute the current density transient for the NC-60 anode and the Miller supply. The result is shown in Figure 49. From this curve it may be seen that the initial current density is  $\sim 24000$  amps/cm<sup>2</sup> and that although it drops rapidly at first it remains above the steady state value (100 amps/cm<sup>2</sup>) for more than 3 sec. Of especial significance is the fact that the average current density for the first second after ignition is  $\sim 1000$  amps/cm<sup>2</sup>. Referring to equation 26 and assuming the typical values for  $V_a$  and  $\phi_a$  of 10 and 5 volts respectively, we see that for  $J=1000$  amps/cm<sup>2</sup>, the power loading of the contact area on the anode during the first second after ignition is  $\sim 15$  KW/cm<sup>2</sup>. This result explains the local melting observed on the surface of porous tungsten anodes following the ignition process.

### (3) Control of ignition damage

From the results of the tests on arc ignition transients it is obvious that elimination of ignition damage requires control of the transient current density starting from

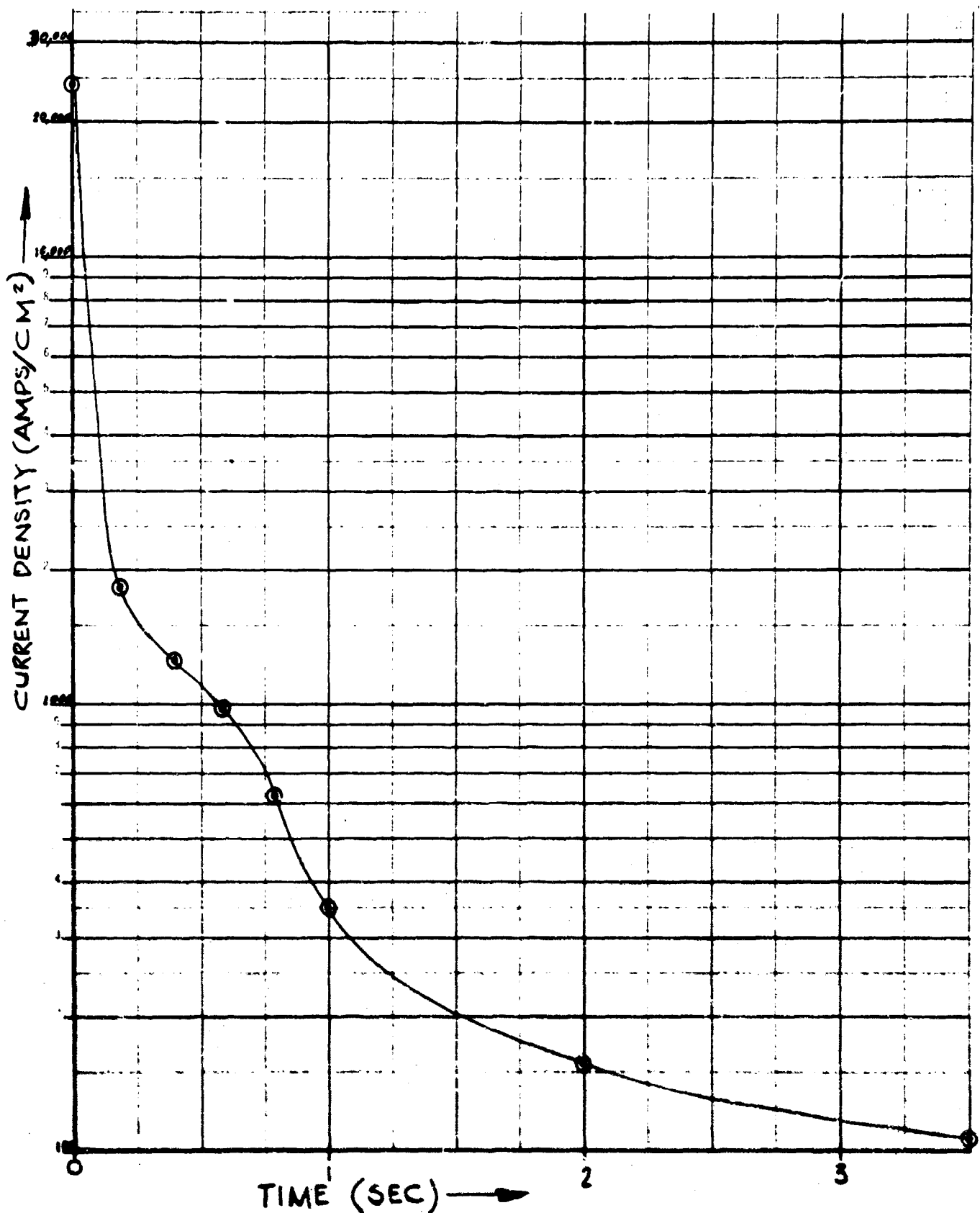


FIG. 49 CURRENT DENSITY TRANSIENT FOR NC-60 ANODE  
AND MILLER POWER SUPPLY

the moment of ignition. Ideally the initial current density should be restricted to a value well below the steady state current density, low enough for example to avoid all possibility of local melting in the case of metal electrodes. Then the current density should be increased at a rate which is preferably slower than the observed current density growth rate, e.g. at a rate which would increase the current density gradually to steady state in about 5 or 6 seconds. Since the growth rate of anode area coverage is not readily under the control of the operator it follows that control of current density is best accomplished by control of the arc current. From empirical observation it was determined that the maximum initial power density on the surface of the sintered tungsten anodes (at the flow rates required for proper FTA operation) should be not greater than about  $0.4 \text{ KW/cm}^2$ . This translates to a starting current below 30 amps.

The constant current supply was not capable of regulating the current below about 40 amps and therefore could not be used to prevent ignition damage without major revision. Also because of its limited current and voltage range and the much greater versatility of the Miller supply, the remedial measures to control ignition damage on tungsten electrodes were applied to this unit.

In view of the slow response of the Miller current regulation circuit it was decided to control the initial arc current by external resistance. First a shunt resistance was placed

across the arc terminals to by-pass most of the initial current around the discharge, which could be removed by a switch after an appropriate time interval. However, when a sufficiently low shunt resistance was used, the voltage across the arc before ignition became erratic. A ballast resistance in series with the arc was then tried. This also was unsatisfactory in that a large and cumbersome (water-cooled) ballast resistor was required to reduce the starting current below 30 amps. A combination of the two proved effective in requiring a reasonably sized ballast resistance and a shunt resistance large enough to provide a residual voltage drop across the electrodes to allow for positive ignition.

The actual system used involved a 0.588 ohm series ballast resistance and a 0.1 ohm shunt resistance. The current level rheostat on the Miller was coupled to a motorized drive unit with a cam-actuated switch which stopped rotation at any pre-adjustable arc current level. A timing circuit was used to provide the following program sequence.

With both resistances connected the start button served to start the timing sequence and ignite the arc, the initial current being controlled by the two resistances. After about 2.5 sec. the shunt resistance was removed from the circuit by means of circuit breaker actuated by the timer. Simultaneously the current level control motor was started which rotated the rheostat so as to increase the arc current at a rate of 20 amps per sec. At about 8 secs following ignition the ballast resistance was

shorted out by means of a relay also actuated by the timer. A short time later depending on the preadjusted arc current level the current control motor was stopped by the cam switch, thus completing the ignition cycle.

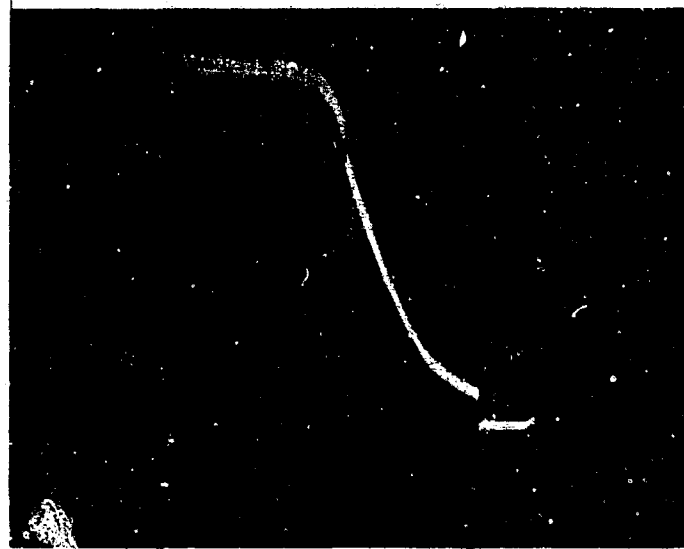
Figure 50 is an oscillogram of the programmed current variation carried out in accordance with the above sequence. The trace (which reads from right to left) shows an initial current of about 24 amps which is maintained for 2.5 sec., a period which allows for the growth of the anode coverage area to near its steady state value. The rate of rise of current thereafter (20 amps/sec) is also slow enough to avoid the creation of thermally destructive values of current density during the entire ignition cycle. A total ignition time of about 10 sec. is required.

Use of this technique for porous tungsten anodes was successful in completely eliminating surface melting with the Miller supply. Figure 51 is a photograph of such an anode after 10 successive ignitions. Although the current coverage is clearly visible due to the brighter appearance of the active area, no sign of melting or thermal damage is visible.

The above technique of arc ignition control was utilized for all subsequent experiments performed with tungsten anodes in an FTA set-up.

#### B. Radiation Source

Results obtained on the FTA/FCC radiation source subsequent to Sept. 30, 1968 involve measurements of spectral irradiance and a microbrightness profile of the emitting zone.



HOR: 2 SEC./DIV.

VERT: 20 AMP./DIV.

(CURRENT REFERENCE LEVEL -  
SECOND GRATICLE LINE FROM BOTTOM)

FIG. 50 ARC CURRENT VARIATION DURING PROGRAMMED  
IGNITION SEQUENCE

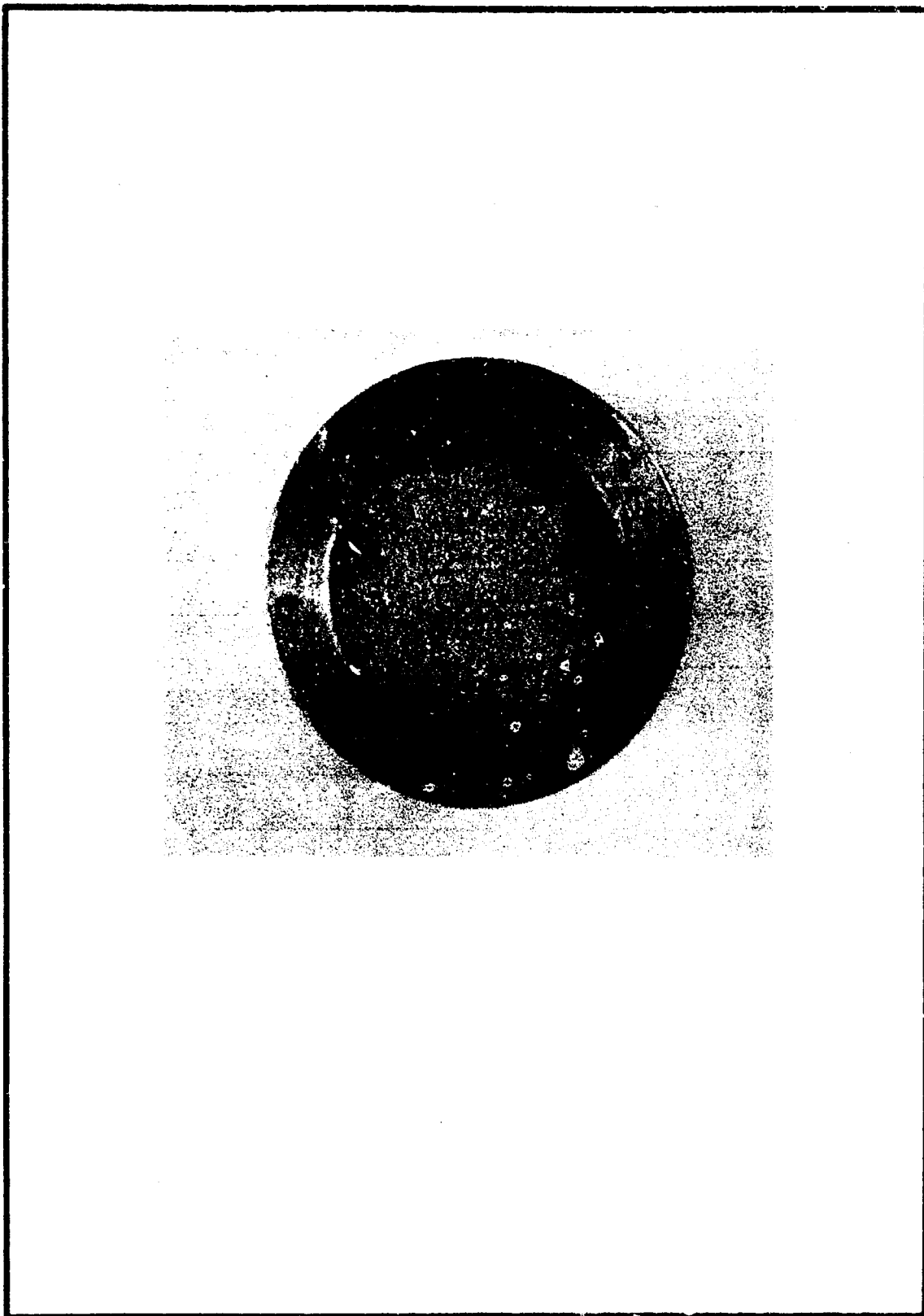


FIG. 51 TUNGSTEN ANODE SURFACE AFTER TEN IGNITIONS  
WITH PROGRAMMED CONTROL SEQUENCE

(1) Spectral irradiance

The radiometry equipment used in the measurement of spectral irradiance has been described in section II D above (see Figure 38). In order to evaluate spectral irradiance a spectral intensity scan is made first with the arc source and immediately thereafter with a standard lamp in the identical geometry. The standard lamp consisted of a G.E. 1000 watt quartz-iodine lamp calibrated for spectral irradiance by the Eppley Laboratories. In a number of runs checks for consistency were made by taking a standard curve just before and just after the arc source. In all cases the records checked to better than 2% indicating that drift in the radiometric components was quite small. The irradiance curve was of course obtained by taking the ratio of the arc source to standard lamp recording deflections for corresponding wave length intervals.

A typical result is shown in Figure 52. Here following customary procedure, the curve (solid line) is plotted as percent of total radiated energy per unit wave length interval, in order to facilitate comparison to other types of sources. Also plotted for comparison is the spectral distribution for a vortex-stabilized arc radiation source<sup>(34)</sup> operated under nearly identical conditions of lamp pressure and power input. It is seen that the FTA/FCC source exhibits higher irradiance over almost all parts of the spectrum, the difference being most pronounced in the visible region. This obviously reflects enhanced continuum radiation for the FTA/FCC source. It is thought to result from the higher temperatures generated by the FCC due to the constriction on the emitting zone

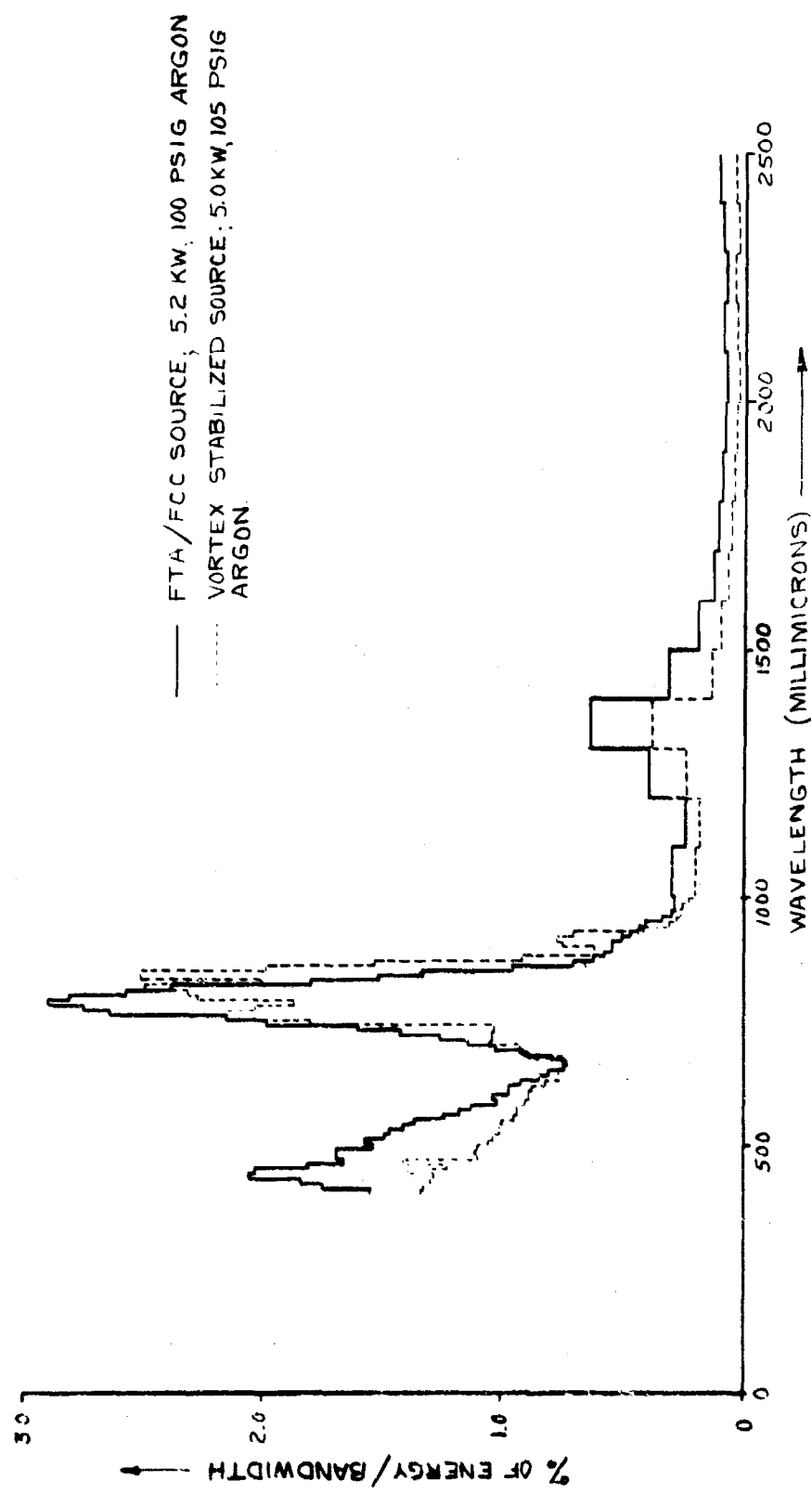


FIG. 52 SPECTRAL IRRADIANCE OF FTA/FCC AND VORTEX-STABILIZED ARC RADIATION SOURCES

off the cathode tip caused by the convergent gas flow at this point (cf. Figure 9). The unusually high degree of ionization indicated by measurements on the FTA column (section II A) may also be involved, since a high free electron density in FTA column would be expected to diffuse rapidly throughout the entire discharge. A high electron density in addition to elevated electron temperature would enhance both the Kramers and Bremsstrahlung components of the continuum radiation.

A measure of the improvement in performance for the visible region of the spectrum is given by the luminous efficacy of the source, which is defined by

$$\eta_e = 680 \frac{\int_{\text{c}}^{\infty} H_{\lambda} V_{\lambda} d\lambda}{\int_{\text{c}}^{\infty} H_{\lambda} d\lambda} \quad \text{lumens per watt}$$

where  $\eta_e$  = luminous efficacy

$H_{\lambda}$  = spectral irradiance

$V_{\lambda}$  = standard visibility function

$\lambda$  = wavelength

The data indicated by the solid curve of Figure 52 was used to compute  $\eta_e$ . The integrations were performed numerically after converting the ordinates to the proper units. The result was

$\eta_e = 74.3$  lumens per watt. The values reported for the 5 KW xenon short arc lamp are  $\sim 50$  lumens per watt. This indicates

a distinct improvement for illumination applications, especially when the fact is considered that argon was used in the present case and that a further improvement can be expected when xenon is substituted for argon as the working gas.

The enhancement of the continuum radiation should also improve the performance of the FTA/FCC source as a solar simulator. Except for the large near infra-red peak, common to all arc sources employing argon or xenon, the problem of matching the Johnson curve requires increasing the ratio of the continuum to infra-red radiation. For the FTA/FCC source an improvement in spectral matching would therefore appear to be more easily achievable. This would involve a scale-up in power level and the use of a composite mixture of working gases, including xenon.

#### (2) Microbrightness profile

One of the desirable performance characteristics of a radiation source is the concentration of the emitting zone into as small an area as possible. This simplifies the design of the optical collection system and improves the degree of collimation obtainable for the on-target beam. In order to evaluate this feature for the FTA/FCC source the microbrightness profile of the arc column was measured. The technique involves projecting an enlarged image of the arc and scanning the resultant image to obtain a detailed brightness profile. An image, optically enlarged about 30 times, was focussed on a movable mask containing a horizontal slit. The position of the slit was movable in the

vertical direction. Behind the mask a radiation detector, consisting of an Eppley thermopile behind a narrow (1 mm) vertical slit, was mounted so that it could traverse the horizontal slit in the mask. Repeated traverses of the detector were made for a series of vertical positions of the horizontal slit from top to bottom of the arc image. From the series of recordings so obtained the isobrightness contour lines were located and the results are plotted in Figure 53. Unfortunately lack of time at the end of the project precluded the calibration of the isobrightness contours to absolute intensity. However, the profile indicated in Figure 53 gives a good indication of the spatial distribution of source intensity.

The influence of the colliding jets is clearly evident. It is also apparent that the source intensity is highly concentrated in the region just off the cathode tip. For practical purposes the emitting zone may be considered to be largely confined to an oval-shaped region contiguous with the cathode, about 3 mm. long and 2 mm. wide. This compares favorably with other convected arc radiation sources and in fact approximates the profile of the short arc lamp. The emitting zone is sufficiently concentrated to permit collection of the radiation into a well-collimated beam. Further, the emitting zone area should be to some degree controllable by adjusting the relative amounts, directions and velocities of the anode and cathode jets.

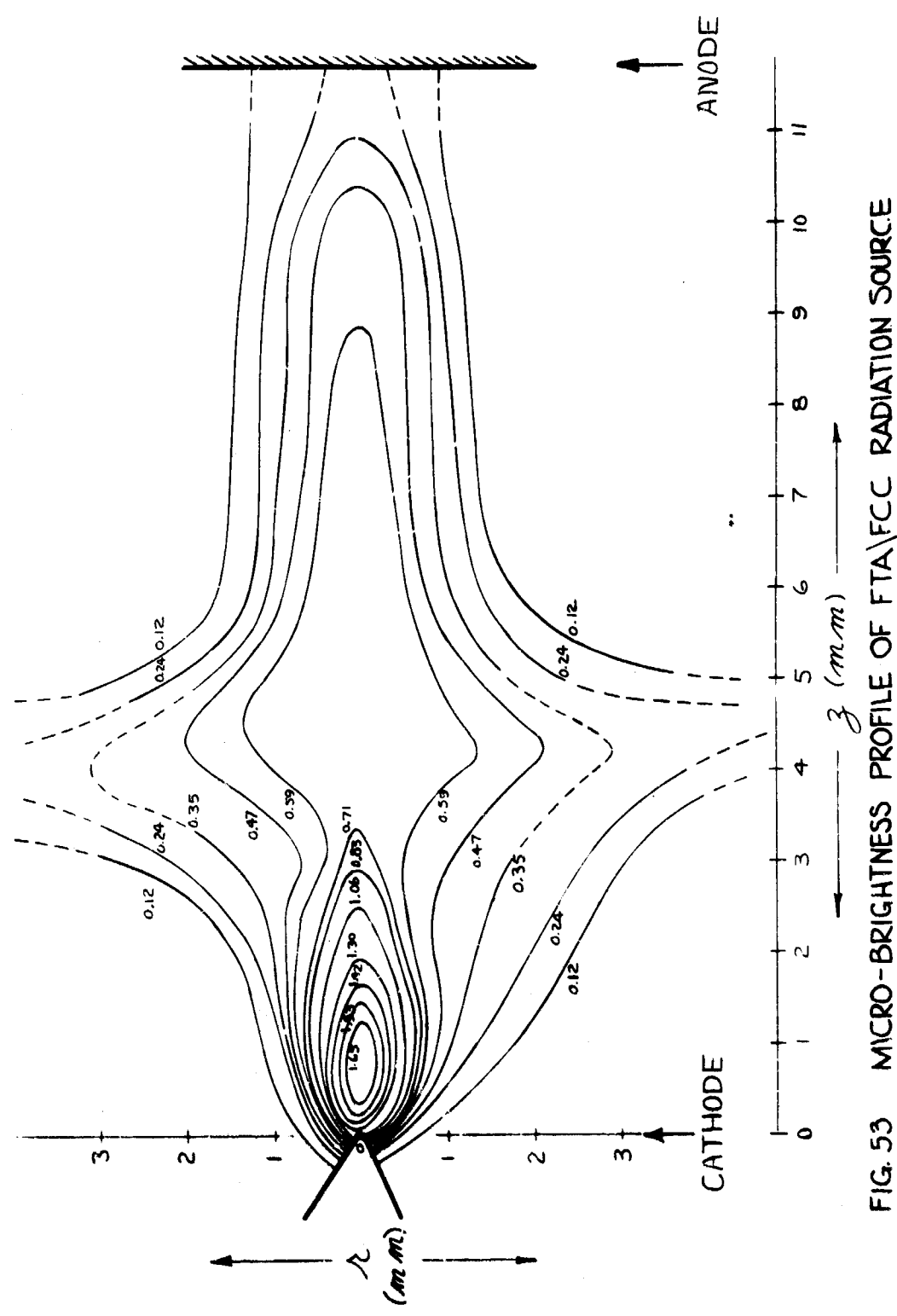


FIG. 53 MICRO-BRIGHTNESS PROFILE OF FTA\FCC RADIATION SOURCE

#### IV. Bibliography

- (1) Sheer, C., Stojanoff, C.G., and Tschang, P.S., "Diagnostic Study of the Fluid Transpiration Arc", Semi-Annual Progress Report P-1/312, Dec. 15, 1964.
- (2) Tschang, P.S., "Energy Transfer and Electron Conduction in the Fluid Transpiration Arc", AFOSR 67-0769, Feb. 17, 1967.
- (3) Stojanoff, C.G., "Characteristics of an Axially Flow-Stabilized Arc and Its Application to the Determination of Transport Properties", Doctoral dissertation, Stuttgart University, July 15, 1968.
- (4) Sheer, C., and Korman, S., "The Fluid Transpiration Arc as a Radiation Source for Solar Simulation", AFOSR 67-2363 Jan. 1 to June 30, 1967.
- (5) AFOSR 68-0762, July 1 to Dec. 31, 1967.
- (6) AFOSR 69-0188TR, Jan. 1 to Sept. 30, 1967.
- (7) Sheer, C., Cooney, J.A., Rothacker, D.L., and Sileo, F.R., "Effect of Fluid Transpiration through the Anodic Arc Boundary", AFOSR-TN-860, June 16, 1961.
- (8) Sheer, C., Cooney, J.A., and Rothacker, D.L., Jour. AIAA, 2, No. 3, pp 483-489, Mar. 1964.
- (9) Stine, H.A., and Watson, V.R., NASA Report No. NASA TN D-1331, Aug., 1962.
- (10) Morse, T.F., Phys. Fluids, 6, No. 10, 1963, pp. 1420-1427.
- (11) Emmons, H.W., Tech. Report No. 23, Engineering Sciences Lab., Harvard University, Dec. 1965.
- (12) Gisinow, M.A., Gerardo, J.B. and Verdeyen, J.T., Phys. Rev., 149, No. 1, Sept. 9, 1966, pp. 91-96.
- (13) Bond, J.W. Jr., Los Alamos Sci. Lab. Report LA-1693, July 1, 1954.
- (14) Spitzer, L. Jr., and Harm, R., Phys. Rev., 89, pp. 977-981, 1953.

(15) Engelhardt, A.G., and Phelps, A.V., Tech. Report No. 20, Physics Dept., Westinghouse Research Labs, Pittsburgh, Pa.

(16) Ahtye, W.F., NASA TN D-2611 (Jan., 1965).

(17) DeVoto, R.S., Report No. SUAA217, Inst. for Plasma Research, Stanford Univ. (Feb., 1965).

(18) Schweitzer, S., and Mitchner, M., AIAA Jour., 4, pp. 1012-1019 (June, 1966).

(19) Vlasov, A.A., Many Particle Theory and Its Application to Plasma", Gordon and Breach, New York, 1961, p. 374.

(20) Kerrebrock, J.L., "Engineering Aspects of Magnetohydrodynamics", Ed. by Mannal and Mather, Columbia Univ. Press, 1962.

(21) Spitzer, L. Jr., "Physics of Fully Ionized Gases", Interscience, 1956, pg. 78.

(22) Busz-Peukert, G. and Finkelnburg, W., Z. Physik, 144, 244 (1956).

(23) Finkelnburg, W., and Maecker, H., "Handbuch der Physik", vol. XXII, Springer, 1956.

(24) Druxes, H., Schmitz, G., and Patt, H.J., Z. Physik, 203, 192-213 (1967)

(25) Sheer, C., et al., "Transient Probe Diagnostics of Dense Plasmas" ARL Report No. ARL 69-0105, Wright Patterson Air Force Base, Ohio, May 1965.

(26) Tschang, P.S., Jour. AIAA, 3, No. 5, 849-852, (May, 1965).

(27) Stojanoff, C.G., Jour. AIAA, 4, 1722-1766 (1966).

(28) Grey, J. et al, Rev. Sci. Instr., 33, No. 7, 738-741 (July, 1962).

(29) Tschang, P.S., ARL Report No. 65-95, Thermomechanics Laboratory, Aerospace Research Labs. Wright Patterson Air Force Base, Ohio, May 1965.

(30) Katsnel'son, B.D., and Timofeyeva, F.A., Kotloturbostroyeniye, 5, 1949.

(31) Barkan, P., and Whitman, A.M., AIAA Jour., 4, No. 9, 1691-93, (1966).

(32) Stair, R., et al, J. Res. NBS, 64A, 291 (1960).

(33) Sheer, C., et al, Air Force Technical Note No. AFOSR-TN-86,  
Mechanics Division, AFOSR, Arlington, Va., (June 16, 1961).

(34) Duncan, C., et al, "Radiometry Research", NASA Report  
No. X-713-67-73, Goddard Space Flight Center, Greenbelt, Md.,  
March, 1967 (See Figure 4, pg. II-112).

## UNCLASSIFIED

Security Classification

## DOCUMENT CONTROL DATA - R &amp; D

(Security classification of title, body of abstract and indexing annotation must be entered when the overall report is classified)

1. ORIGINATING ACTIVITY (Corporate author) <b>Columbia University Electronics Research Laboratories New York, New York 10027</b>		2a. REPORT SECURITY CLASSIFICATION <b>Unclassified</b>
3. REPORT TITLE  <b>DIAGNOSTIC STUDY OF THE FLUID TRANSPERSION ARC</b>		2b. GROUP
4. DESCRIPTIVE NOTES (Type of report and inclusive dates)  <b>Scientific Final</b>		
5. AUTHOR(S) (First name, middle initial, last name)  <b>Charles Sheer Christo G. Stojanoff Samuel Korman Pin S. Tschang</b>		
6. REPORT DATE  <b>31 March, 1969</b>	7a. TOTAL NO. OF PAGES  <b>132</b>	7b. NO. OF REFS  <b>33</b>
8a. CONTRACT OR GRANT NO.  <b>AF 49(638)-1395</b>	9a. ORIGINATOR'S REPORT NUMBER(S)  <b>F/312</b>	
b. PROJECT NO.  <b>9783-02</b>	9b. OTHER REPORT NO(S) (Any other numbers that may be assigned this report)  <b>AFOSR 70-0195TR</b>	
10. DISTRIBUTION STATEMENT  <b>1. This document has been approved for public release and sale; its distribution is unlimited</b>		
11. SUPPLEMENTARY NOTES  <b>Tech, other</b>	12. SPONSORING MILITARY ACTIVITY  <b>AF Office of Scientific Research 1400 Wilson Boulevard (SREM) Arlington, Va. 22209</b>	
13. ABSTRACT  <b>This report covers the investigation of the fluid transpiration arc in combination with the fluid convection cathode. Various arc configurations and operating techniques are described. Preliminary theoretical treatments of the interaction phenomena due to gas injection through a porous anode and through a tightly shrouded cathode nozzle with the arc discharge are carried out. Good agreement has been shown in some respects although several anomalies have been found attributed to deficiencies in the modelling. Several diagnostic techniques were developed during this investigation featuring transient plasma probes. These include a Hall magnetic probe, a thermocouple probe, a fiber optics probe and a Pitot tube probe. The cause of arc ignition damage to electrodes was investigated and corrected. The radiation characteristics of a combination arc source featuring a collinear geometry for the fluid transpiration anode and fluid convection cathode, were also investigated. Improved performance in conversion efficiency and luminous efficacy was demonstrated along with a favorable brightness profile.</b>		

DD FORM 1 NOV 65 1473

UNCLASSIFIED

Security Classification

**UNCLASSIFIED**

**Security Classification**

14. KEY WORDS	LINK A		LINK B		LINK C	
	ROLE	WT	ROLE	WT	ROLE	WT
Fluid transpiration arc						
Fluid convection cathode						
Porous anode development						
Ignition transient						
Plasma jet radiation source						
Solar simulation source						

**Security Classification**